Lawrence Berkeley National Laboratory
Recent Work

Title
DOUBLE BEAM INTERFEROMETRY FOR ELECTROCHEMICAL STUDIES

Permalink
https://escholarship.org/uc/item/2qn0r3rt

Author
Muller, Rolf H.

Publication Date
1972-03-01

eScholarship.org Powered by the California Digital Library
University of California

To be published as a chapter in a book "Advances in Electrochemistry and Electrochemical Engineering" Vol. 9 R. Muller, ed. (Interscience)

LBL-115 Rev.
Preprint c.1

RECEIVED
LAWRENCE
RADIATION LABORATORY

LIBRARY AND
DOCUMENTS SECTION

# DOUBLE BEAM INTERFEROMETRY FOR ELECTROCHEMICAL STUDIES

Rolf H. Muller

March 1972

AEC Contract No. W-7405-eng-48

For Reference

Not to be taken from this room

LBL-115 Rev. c.1

**DISCLAIMER**

This document was prepared as an account of work sponsored by the United States Government. While this document is believed to contain correct information, neither the United States Government nor any agency thereof, nor the Regents of the University of California, nor any of their employees, makes any warranty, express or implied, or assumes any legal responsibility for the accuracy, completeness, or usefulness of any information, apparatus, product, or process disclosed, or represents that its use would not infringe privately owned rights. Reference herein to any specific commercial product, process, or service by its trade name, trademark, manufacturer, or otherwise, does not necessarily constitute or imply its endorsement, recommendation, or favoring by the United States Government or any agency thereof, or the Regents of the University of California. The views and opinions of authors expressed herein do not necessarily state or reflect those of the United States Government or any agency thereof or the Regents of the University of California.

0 0 0 0 3 6 0 0 9 7 7



DOUBLE BEAM INTERFEROMETRY FOR ELECTROCHEMICAL STUDIES

Contents

Abstract . . . . . . . . . . . . . . . . . . . . . . . . . . . iii

I. Introduction . . . . . . . . . . . . . . . . . . . . . . . 1

1. Principles of Interferometry . . . . . . . . . . . . . . 1

2. Electrochemical Refractive Index Fields . . . . . . . . . 5

II. Refractive Index and Composition . . . . . . . . . . . . . 6

1. Empirical Correlations . . . . . . . . . . . . . . . . . 6

2. Molar Refractivity . . . . . . . . . . . . . . . . . . . 7

3. Spectral Dependence of Refractive Index . . . . . . . . . 18

4. Temperature Dependence of Refractive Index . . . . . . . 19

III. Interferometry of Electrochemical Refractive Index Fields . 21

1. Instrumentation . . . . . . . . . . . . . . . . . . . . . 21

A. Introduction . . . . . . . . . . . . . . . . . . . . 21

B. Rayleigh Interferometers . . . . . . . . . . . . . . 25

C. Jamin Interferometers . . . . . . . . . . . . . . . . 27

D. Mach-Zehnder Interferometers . . . . . . . . . . . . 32

E. Michelson Interferometers . . . . . . . . . . . . . . 36

F. Polarizing Interferometers . . . . . . . . . . . . . 38

G. Gouy Interferometers . . . . . . . . . . . . . . . . 40

H. Diffraction Interferometers . . . . . . . . . . . . . 41

2. Interpretation of Interferogram . . . . . . . . . . . . . 44

A. Conventional Interpretation . . . . . . . . . . . . . 44

B. Consideration of Light Deflection . . . . . . . . . . 48

a. Introduction . . . . . . . . . . . . . . . . . . . 48

b. Constant Refractive Index Gradient . . . . . . . 49

c. Effect of Focussing . . . . . . . . . . . . . . . 57

d. Nernst Boundary Layers . . . . . . . . . . . . . 62

e. Real Boundary Layers . . . . . . . . . . . . . . 63

f. Anodic Boundary Layers . . . . . . . . . . . . . 68

C. Diffraction Effects . . . . . . . . . . . . . . . . . 68

3. Applications . . . . . . . . . . . . . . . . . . . . . . 70

A. Diffusion and Electrophoresis . . . . . . . . . . . 70

B. Mass Transport Boundary Layers . . . . . . . . . . 71

C. Outlook . . . . . . . . . . . . . . . . . . . . . . . 72

IV. Interferometry of Electrode Surfaces . . . . . . . . . . . 73

References . . . . . . . . . . . . . . . . . . . . . . . . . . 76

Figure Captions . . . . . . . . . . . . . . . . . . . . . . . 85

0 0 0 0 3 6 0 0 0 7 8



# DOUBLE BEAM INTERFEROMETRY FOR ELECTROCHEMICAL STUDIES

Rolf H. Muller

Inorganic Materials Research Division, Lawrence Berkeley Laboratory and
Department of Chemical Engineering; University of California
Berkeley, California

## ABSTRACT

Principles of double beam interferometry for the study of refractive index fields and surface topographies are reviewed. Potentials and limitations of different interferometer designs are compared, and an analysis is given of the interpretation of interferometric results.

0 0 0 0 3 6 0 0 9 7 9



# DOUBLE BEAM INTERFEROMETRY FOR ELECTROCHEMICAL STUDIES

## I. INTRODUCTION

### 1. Principles of Interferometry

Interferometry provides an elegant and sensitive tool for the study of refractive index fields. Local refractive index variations of electrochemical interest are due to variations in composition and concentration. Light is particularly well suited as a probe for the study of concentration fields, since it permits continuous observation of an object with a minimum of disturbance, and offers good geometrical resolution. Interferometer measurements usually result in pictures which are intuitively understandable, at least in a semi-quantitative way. It is characteristic of optical techniques that the propagation direction of the light is not equivalent to the two other dimensions of space. The compound effect which results if the light successively traverses areas of different properties can often not be resolved satisfactorily. It is, therefore, desirable that the probe encounters over its entire path the same value of the variable to be measured. Thus, interferometry is best suited for one or two-dimensional refractive index fields.

The refractive index of a solution depends on its composition and is defined as the ratio of the phase velocity c of light in vacuum to the velocity v in the medium

$$n = \frac{c}{v} \qquad (1)$$

Since the refractive index of a medium is affected by all its constituents, as well as its temperature (and pressure), it is desirable to restrict the use of interferometry of concentretion fields to one-component, isothermal solutions.

A plane wavefront of light, entering a medium with locally variable refractive index, will not remain plane, because light travels more slowly in regions of higher refractive index. The resulting local variation in phase is proportional to the refractive index variation $\Delta n$ and the geometrical path length d over which it exists. It is, therefore, convenient to define the product of geometrical path length d and refractive index n as the optical path length p

$$p = n\ d \tag{2}$$

For fixed geometrical path length, the optical path difference is

$$\Delta p = \Delta n\ d \tag{3}$$

The optical path difference can also be expressed in number of wavelengths by use of the wavelength $\lambda_o$ of light in vacuum

$$\Delta z = \frac{\Delta p}{\lambda_o} \tag{4}$$

Similarly, a corresponding phase difference $\Delta\phi$ is formulated as

$$\Delta\phi = \Delta z\ 2\pi \tag{5}$$

Fig. 1 illustrates schematically the effect of a one-dimensional refractive index field (a) in a stratified specimen tank (b) on the propagation of light through it. Due to the local variation in wavelength, different parts of a wave entering the cell in phase, increasingly get out of phase, as they propagate through the cell, while a similar wave, propagating through a reference tank (d) of uniform refractive index (c), remain in phase. In Fig. 1, it is assumed that the optical path length

0 0 0 0 3 6 0 0 7 8 0



in the center of both tanks is the same and that they differ by plus and minus half a wavelength at both edges. A suitable superposition of the light beams issuing from both tanks would result in alternate dark and bright interference fringes,with constructive interference occurring in the center and destructive interference at the edges, as indicated in (e). It is the purpose of a double beam interferometer to provide the two light beams, which possess a stationary point-by-point phase relationship,and to superimpose the exiting beams in such a way that both interference phenomenon and object are imaged. Thus, local variations of phase due to differences between object and reference are made visible as intensity variations (usually in the form of interference fringe displacements), can be quantitatively evaluated.

The principle illustrated above is characteristic of double beam interferometry, where two light beams are brought to interference. Typically, one beam has traversed the specimen, the other serves as a reference with a simple (usually plane) wavefront. In general, the specimen beam is spacially separated from the reference beam and traverses the specimen once (occasionally twice). Due to the simple optical principles of double beam interferometry, measurements derived by this technique are more amenable to the analysis and correction of optical errors than measurements obtained by multiple beam interferometry, where interference is due to the superposition of an infinite series of waves with multiple passes through the specimen. The instrumentation required for double beam interferometry is, however, distinctly more complex.

As can be seen in Fig. 1, light propagating through a medium with refractive variations across the beam suffers a tilt in wave front (dashed line connecting crest of waves). Since the propagation direction is oriented normal to the wavefront, the beam is deflected from its original propagation direction. This effect is utilized in Schlieren-optical devices.

An optical path difference, in addition to being due to a refractive index variation, can also be caused by a change in geometrical path, with constant refractive index of the medium. Thus, double beam interferometry with reflected light can be used for determining the micro-topography of electrode surfaces. In this case, local phase variations are introduced by the different geometrical position of reflecting surface elements.

Holographic interferometry is a special case of double beam interferometry. It can be applied to the observation of refractive index fields or surface topographies and will be discussed in a separate chapter.

It is the purpose of this chapter to discuss the optical principles and to analyze some of the potentials and limitations of double beam interferometry for the mapping of refractive index fields and, to a lesser degree, surface topographies of electrochemical interest. Examples of instrumentation and application have been chosen on the basis of their interest for future development rather than historical completeness.

---

0 0 0 0 3 6 0 0 9 3 1



## 2. Electrochemical Refractive Index Fields

Pure diffusion in solutions provides some of the best defined refractive index fields for observation by interferometry. For binary solutions, the concentration is, in general, uniquely determined by the refractive index, which facilitates the derivation of diffusion coefficients from interferometer data.

In zone electrophoresis, the complete or partial separation of constituents results in refractive index fields which can be observed by interferometry. Components can be identified by their mobility and their amount is determined from the refractive index change.

The study of mass transfer boundary layers due to convective diffusion and migration near electrode surfaces offers some particularly rewarding uses of interferometry. Some interferometers for the study of diffusion layers, together with other techniques, have been discussed by Ibl (67). Electrochemical reactions across a solid-liquid interface, proceeding at a finite rate, require the transport of reactants and products to and from the interface. As a result, mass transfer boundary layers, i.e. regions in which the composition of the fluid phase is different from that in the bulk, are formed along the interface. A typical dimension of such mass transfer boundary layers would be 0.1 mm. Since mass transfer is often the limiting factor for the specific output of electrochemical reactors, a detailed understanding of mass transfer boundary layers is essential to the design and operation of many electrochemical devices. Local mass transfer boundary layers can be observed by interferometric techniques under conditions which are not restricted to operation at limiting current. The sensitivity to

concentration changes typically is in the order of $10^{-4}$ moles/ℓ, the geometrical resolution can be in the range of microns. The observation of electrochemical mass transfer boundary layers presents a special challenge to the use of interferometry, because of the small dimensions and large gradients typically involved. Some of these problems have been of particular interest to the author. Mass transfer boundary layers will, therefore, be referred to most often in the discussions to follow. However, most of the optical analysis applies equally to other electrochemical situations and, with appropriate modifications, even to applications in the areas of heat transfer or gas dynamics.

## II. REFRACTIVE INDEX AND COMPOSITION

### 1. Empirical Correlations

Variations in the refractive index of a solution, determined by interferometry, need to be interpreted as variations in composition. For this purpose, it is necessary to know the relation between the two variables. This relation is most firmly established by refractive index measurement of solutions of known composition. Algebraic expressions can then be developed to represent the data.

The concentration of most isothermal solutions of a single solute, such as copper sulfate in water (Fig. 2), can be unequivocally determined from the refractive index. For some solutions, such as sulfuric acid (Fig. 3), this relationship may not be unique over certain concentration ranges. The composition of multi-component solutions, such as aqueous copper sulfate and sulfuric acid (Fig. 4), cannot be determined from a single refractive index measurement. The number of measurements necessary to establish refractive index correlations of multi-component solutions at different temperatures requires a considerable effort which

0 0 0 0 3 6 0 0 7 8 2



is multiplied if data for different wavelengths are desired. Due to inevitable deviations in composition from the desired values, the results have to be correlated by multiple regression analysis (124). Some wavelengths of interest in interferometry are listed in Table I. The yellow sodium D light has been most commonly used in refractometry. Refractive index data for that light are often designated by a subscript D. The average wavelength between both lines of the doublet is listed in Table I.

## 2. Molar Refractivity

A useful concept for the estimation of the refractive index from density data is the molar refractivity P, which can be defined (12) in terms of refractive index n, molecular weight M and density ρ as

$$P = \frac{M}{\rho} \frac{n^2 - 1}{n^2 + 2} \quad . \quad (6)$$

The molar refractivity is best determined from one set of refractive index and density measurements. Less reliably, it can also be obtained by the addition of atomic refractivities and contributions due to the bonding between the constituent elements in a compound.(107,149) The molar refractivity of gases has been shown to be remarkably independent of density over a 100-fold pressure range (12). The values for water at different temperatures, shown in Table II, show a slightly larger variation. As a result, the refractive indices at different temperatures, computed from the densities at those temperatures and the molar refractivity at 20°C, differ somewhat from the measured refractive indices (Table III). The relative error of the predicted refractive index change decreases from 10 to 5% with increasing temperature change.

Equation (6) can be solved for n by trial and error. Tabulated

TABLE I

Typical Wavelengths of Light Used in Interferometry

| Source | Wavelength, nm |
|---|---|
| Hg arc | 404.7 |
| Hg arc | 435.8 |
| A laser | 488.0 |
| A laser | 514.5 |
| Tl arc | 535.0 |
| Hg arc | 546.1 |
| Kr laser | 568.2 |
| Na arc | 589.3 |
| He Ne laser | 632.8 |
| Kr laser | 647.1 |
| Ruby laser | 694.3 |

0 0 0 0 0 6 0 0 7 8 3



TABLE II

Molar Refractivity of Water at Different Temperatures.

| Temperature °C | Density ρ g/cm$^3$ (61) | Refractive Index $n_D$ (61) | Molar Refractivity P (Eq. 6) |
|---|---|---|---|
| 20 | 0.99823 | 1.33299 | 3.71228 |
| 30 | 0.99567 | 1.33192 | 3.71097 |
| 40 | 0.99224 | 1.33051 | 3.70942 |
| 50 | 0.98807 | 1.32894 | 3.70899 |
| 60 | 0.98324 | 1.32718 | 3.70907 |
| 70 | 0.97781 | 1.32511 | 3.70819 |
| 80 | 0.97183 | 1.32287 | 3.70759 |
| 90 | 0.96534 | 1.32050 | 3.70753 |

TABLE III

Prediction of the Refractive Index of Water at Different Temperatures Based on the Densities Given in Table II and the Molar Refractivity at 20°C.

| Temperature °C | Refractive index, $n_D$ | |
|---|---|---|
| | Predicted (Eq. 6) | Measured (61) |
| 20 | 1.3330 | 1.3330 |
| 30 | 1.3320 | 1.3319 |
| 40 | 1.3308 | 1.3305 |
| 50 | 1.3293 | 1.3289 |
| 60 | 1.3275 | 1.3272 |
| 70 | 1.3255 | 1.3251 |
| 80 | 1.3233 | 1.3229 |
| 90 | 1.3210 | 1.3205 |

0 0 0 0 3 6 0 0 7 8 4



values of the quantity $(n^2 - 1)/(n^2 + 2)$ are provided for this purpose in Table IV. They are well suited for linear interpolation.

For multi-component systems, an average molar refractivity $\bar{P}$ can be based on the contributions from each constituent of molar refractivity $P_i$

$$\bar{P} = \Sigma f_i P_i \tag{7}$$

$f_i$ is the mole fraction of component i and is defined in terms of the molarities $C_i$ (number of gram moles of solute i per liter of solution) of the constituents

$$f_i = c_i/\Sigma c_i \tag{8}$$

If an average molecular weight $\bar{M}$ is similarly defined as

$$\bar{M} = \Sigma f_i M_i \tag{9}$$

Equation 6 becomes for a mixture

$$\Sigma f_i P_i = \frac{\Sigma f_i M_i}{\rho} \frac{n^2 - 1}{n^2 + 2} \tag{10}$$

$\rho$ and n are then density and refractive index of the mixture. The refractive index of mixtures (and solutions) can be estimated by use of Eq. 10 from the molar refractivity of the pure components and the density of the mixture. Results of such an estimate for sulfuric acid-water mixtures are shown in Table V. The predicted change in refractive index over that of pure water seems to be within 5% of the measurements over the entire concentration range (except for a 9% deviation at 5 wt.%). Because no refractive index data of pure sulfuric acid could be found in the literature, an extrapolated value, derived from the average molar

TABLE IV

Values of the Quantity $(n^2 - 1)/(n^2 + 2)$ for Use in Calculating Molar Refractivities.

| n | $\frac{n^2 - 1}{n^2 + 2}$ | n | $\frac{n^2 - 1}{n^2 + 2}$ |
|---|---|---|---|
| 1.330 | 0.204012 | 1.350 | 0.215173 |
| 1.331 | 0.204573 | 1.351 | 0.215727 |
| 1.332 | 0.205134 | 1.352 | 0.216281 |
| 1.333 | 0.205695 | 1.353 | 0.216835 |
| 1.334 | 0.206256 | 1.354 | 0.217388 |
| 1.335 | 0.206816 | 1.355 | 0.217940 |
| 1.336 | 0.207376 | 1.356 | 0.218493 |
| 1.337 | 0.207935 | 1.357 | 0.219045 |
| 1.338 | 0.208494 | 1.358 | 0.219596 |
| 1.339 | 0.209053 | 1.359 | 0.220147 |
| 1.340 | 0.209611 | 1.360 | 0.220698 |
| 1.341 | 0.210169 | 1.361 | 0.221249 |
| 1.342 | 0.210727 | 1.362 | 0.221799 |
| 1.343 | 0.211284 | 1.363 | 0.222348 |
| 1.344 | 0.211840 | 1.364 | 0.222898 |
| 1.345 | 0.212397 | 1.365 | 0.223447 |
| 1.346 | 0.212953 | 1.366 | 0.223995 |
| 1.347 | 0.213509 | 1.367 | 0.224543 |
| 1.348 | 0.214064 | 1.368 | 0.225091 |
| 1.349 | 0.214619 | 1.369 | 0.225639 |

TABLE V

Prediction of the Refractive Index of Sulfuric Acid - Water Mixtures from the Molar Refractivities of the Pure Components Listed in Table VI and the Density of the Mixtures.

| wt. % $H_2SO_4$ | M $H_2SO_4$ | $f_{H_2SO_4}$ (Eq. 8) | $f_{H_2O}$ (Eq. 8) | $\bar{P}$ (Eq. 7) | $\bar{M}$ (Eq. 9) | ρ (115) | $n_D^{20}$ | |
|---|---|---|---|---|---|---|---|---|
| | | | | | | | Predicted (Eq. 10) | Literature (116) |
| 2 | 0.2064 | 0.0037 | 0.9963 | 3.7489 | 18.3151 | 1.0118 | 1.3355 | 1.3355 |
| 5 | 0.5260 | 0.0096 | 0.9904 | 3.8058 | 18.7827 | 1.0317 | 1.3390 | 1.3385 |
| 9 | 0.9719 | 0.0178 | 0.9822 | 3.8863 | 19.4446 | 1.0591 | 1.3437 | 1.3435 |
| 17 | 1.9362 | 0.0363 | 0.9637 | 4.0657 | 20.9198 | 1.1168 | 1.3534 | 1.3525 |
| 35 | 4.4963 | 0.0900 | 0.9100 | 4.5893 | 25.2230 | 1.2599 | 1.3756 | 1.3745 |
| 70 | 11.4906 | 0.2998 | 0.7002 | 6.6325 | 42.0190 | 1.6105 | 1.4222 | 1.4240 |
| 90 | 16.6497 | 0.6231 | 0.3769 | 9.7820 | 67.9080 | 1.8144 | 1.4358 | 1.4325 |

refractivity of the 80% mixture, was used for determining the molar refractivity of sulfuric acid listed in Table VI.

The same procedure has been applied to predict the refractive index of aqueous copper sulfate solutions. The molar refractivity of the solute (Table VI) has been based on the density of the hydrated crystal and the average of its three principal refractive indices (61). The refractive index of solutions, thus derived, is compared in Table VII with measurements from the literature. As had been observed in the case of sulfuric acid, the relative error in the predicted refractive index change (over that of pure water) is largest at low concentrations. The error decreases to about 3% at concentrations above 0.4 M.

The use of the molar refractivities of pure components employed above results in surprisingly good predictions of the refractive index of copper sulfate-sulfuric acid-water mixtures, considering that no adjustable parameters were used in these predictions (Table VIII). Over the range of compositions for which reliable measurements are available, the relative error in the predicted refractive index change is at most 3%.

0 0 0 0 3 6 0 0 0 8 6



TABLE VI

Determination of the Molar Refractivity P of Pure Components from Molecular Weight M, Density ρ and Refractive Index n. Data used in the Computations in Tables V, VII and VIII.

| Component | M | ρ | n | P |
|---|---|---|---|---|
| $H_2O$ | 18.016 | 0.99821 | 1.3330 | 3.7125 |
| $H_2SO_4$ | 98.08 | 1.8305 | 1.4162 | 13.4525 |
| $CuSO_4 \cdot 5H_2O$ | 249.69 | 2.284 | 1.532 | 33.8757 |

TABLE VII

Prediction of the Refractive Index of Aqueous Copper Sulfate Solutions from the Molar Refractivities of the Pure Components Listed in Table VI and the Density of the Solutions.

| M Cu $SO_4$ | $\rho^{20}$ (61) | $n_D^{20}$ Predicted (Eq. 10) | $n_D^{20}$ Literature (116) |
|---|---|---|---|
| 0.05 | 1.007 | 1.3347 | 1.3343 |
| 0.1 | 1.015 | 1.3360 | 1.3357 |
| 0.4 | 1.062 | 1.3440 | 1.3441 |
| 0.7 | 1.108 | 1.3515 | 1.3520 |
| 1.0 | 1.153 | 1.3588 | 1.3596 |
| 1.3 | 1.198 | 1.3661 | 1.3670 |

0 0 0 0 0 6 0 0 9 8 7



TABLE VIII

Prediction of the Refractive Index of Copper Sulfate - Sulfuric Acid - Water Mixtures from the Molar Refractivities of the Pure Components Listed in Table VI and the Density of the Mixtures.

| M $CuSO_4$ | M $H_2SO_4$ | $\rho^{25}$ (124) | $n_D^{25}$ Predicted (Eq. 10) | $n_D^{25}$ Measured (124) |
|---|---|---|---|---|
| 0.0500 | 0.492 | 1.0358 | 1.3393 | 1.3391 |
| 0.0992 | 0.496 | 1.0435 | 1.3406 | 1.3404 |
| 0.2998 | 0.494 | 1.0737 | 1.3454 | 1.3455 |
| 0.0494 | 0.983 | 1.0659 | 1.3445 | 1.3442 |
| 0.1017 | 1.008 | 1.0744 | 1.3457 | 1.3457 |
| 0.2970 | 0.979 | 1.1034 | 1.3508 | 1.3506 |
| 0.5001 | 0.997 | 1.1320 | 1.3546 | 1.3550 |
| 0.0502 | 2.013 | 1.1261 | 1.3543 | 1.3543 |
| 0.2990 | 2.020 | 1.1625 | 1.3599 | 1.3599 |

3. Spectral Dependence of Refractive Index

Refractive indices usually decrease with increasing wavelength (Fig. 5). Any change in sensitivity due to this effect is, however, not significant. The use of shorter wavelengths in interferometry still results in greater sensitivity because of the increased phase difference obtained for a given optical path difference (Eqs. 4 and 5).

Measuring the refractive index of the same solution at different wavelengths, in principle, provides the opportunity to determine the concentration of more than one solute. The optical dispersion has been used for the interferometric determination of temperature and composition of different gas mixtures (118) and plasma diagnostics (63). In order to determine the concentration of e.g. two solutes by this method, a refractive index dependence on composition and wavelength, as illustrated schematically in Fig. 6, is necessary. Unfortunately, the wavelength-dependence of the refractive index of most electrolytes over the visible spectral range is too similar to provide independent measurements. Estimates of the spectral dependence of the refractive index of aqueous cupric sulfate-sulfuric acid solutions, based on molar refractivities given in Table IX, support this conclusion. The optical dispersion of several gases has similarly been found too small to be useful (149).

0 0 0 0 0 6 0 0 1 8 8



4. Temperature Dependence of Refractive Index

Since the effect of temperature on refractive index cannot easily be separated from that of solute content, it is important to know what temperature variations can be tolerated in the analysis of concentration fields.

The temperature coefficient of the refractive index, in general, increases with increasing concentration and temperature. Some examples of refractive indices at different temperatures are given in Fig. 7. For a 1 M $CuSO_4$ solution at 18°C, the change in refractive index per °C is $1.88\times10^{-4}$. A comparison with Fig. 2 shows that, at constant temperature the same change in refractive index corresponds to a change in concentration of $7.8\times10^{-3}$ M. For most interferometric concentration determinations it is therefore necessary to reduce local temperature variations to well below 1°C.

Table IX

Molar refractivities at different wavelengths computed from refractive indices shown in Fig. 5 and densities given in Table VI.

| Wavelength, λ | Molar refractivity, P | | |
|---|---|---|---|
| nm | $H_2O$ | $H_2SO_4$ | $CuSO_4 \cdot 5H_2O$ |
| 434 | 3.7871 | 14.0375 | 34.5004 |
| 486 | 3.7539 | 13.9536 | 34.2099 |
| 589 | 3.7125 | 13.8132 | 33.8438 |
| 656 | 3.6942 | 13.7569 | 33.6840 |

0 0 0 0 3 6 0 3 7 8 9



# III. INTERFEROMETRY OF ELECTROCHEMICAL REFRACTIVE INDEX FIELDS

## 1. Instrumentation

### A. Introduction

Double beam interferometers of greatly varying designs have been described in the literature. Some have been used in gas dynamic (105, 117,151,155) or biological studies (52) and can equally be used for electrochemical purposes. A large number of designs has been developed for other purposes, such as length measurements (22) or the testing of optical components and instruments (18,21,59,146). Some of these interferometers can be adapted for purposes of interest here. Typical representatives of different kinds of interferometers and their characteristic features will be discussed in this section.

For the mapping of electrochemical refractive index fields, in particular, mass transfer boundary layers on electrodes, an interferometer should satisfy the following requirements:

1. provide for arbitrarily spacing and orienting interference fringes, when observing a homogeneous medium.
2. provide for placing the virtual origin (localization) of interference fringes in the object.
3. possess high geometrical resolution.
4. have high image intensity.
5. provide large separation of sample and reference beams.
6. have sample beam crossing specimen only once.
7. be immune to vibration.

The flexibility provided by the feature of arbitrary orientation and spacing of interference fringes allows one to choose optimum conditions for the evaluation of interferograms. It will usually be desirable to orient the fringes parallel to the expected refractive index gradient. A large fringe spacing may be preferred for the observation of small fringe displacements. With infinite fringe spacing, in a homogeneous medium, the condition of "interference contrast" is realized. Under this condition, interference fringes in an inhomogeneous medium follow contour lines of equal optical path. With the interference phenomenon located in the object, a true image of the object can be obtained. Thus, two-dimensional refractive index fields may be observed. If the interference fringes originate at infinity, rather than at the finite object distance, aspheric optical elements have to be employed to focus both planes in one direction each. One-dimensional concentration fields resulting from diffusion (51), sedimentation(109)and electrophoresis(94) can be satisfactorily observed this way.

Most electrochemical applications of interferometry require the observation of small areas at high magnification (112). Good optical resolution is therefore necessary. This requirement is similar to that in interference microscopy (52,79) but runs contrary to the commonly encountered observation of large fields at low magnification in aerodynamic and optical testing applications. Short exposure times are desirable for the observation of transient phenomena. The high image intensity required for that purpose is usually associated with a compact construction, which is also favorable for immunity from vibration. A large separation between sample and reference beam facilitates the use of a well-defined reference medium. Purposefully small separations are used

0 0 0 0 0 6 0 0 9 9 0



for differential measurements.

One of the advantages of double beam interferometry over multiple beam interferometry is the simple optical configuration of single passage of the sample beam through the specimen. The double pass feature, accomplished in some instruments by use of a mirror behind the specimen, although it doubles the sensitivity of the instrument, considerably complicates the quantitative analysis of optical artifacts. Due to light deflection in the object or misalignment of the mirror, the reflected beam does not necessarily retrace the path of the incoming beam. In the schematic instrument diagrams which follow, the simple lenses shown usually represent compound lenses in practice.

Due to the statistical nature of light emission from classical monochoromatic sources, time-independent interference can be observed only between two light beams, which are said to be mutually coherent. Such beams possess a stationary point-by-point phase relationship and can be visualized as replica of each other. Theoretical treatments of coherence and double beam interference have been given by Steel (131). The way by which the two coherent beams are produced provides a frequently-used classification of double beam interferometers (14,30,39,79,130) and is used in Table X for some specific examples. The alternatives basically are division of wavefront, where laterally separated parts of a wave are selected, and division of amplitude, where a wave is normally split by partial reflection and transmission (Fig. 8). Diffraction and polarization can be considered special cases of amplitude division (129). Strictly speaking, the different classes can, however, not be completely separated, e.g. partial polarization is associated with amplitude division by reflection. The use of laser light greatly relaxes the need to produce exact duplicate beams for use in interferometry,

Table X. Classification and characteristics of some double beam interferometers.

| Classification | Example | Observable Refractive Index Fields | Fringe Orientation | Fringe Spacing | Fringe Localization | Geometric Resolution | Intensity | Vibration Sensitivity | Separation of Reference Beam |
|---|---|---|---|---|---|---|---|---|---|
| Division of Wavefront | Rayleigh | One-dimensional | Fixed | Fixed | Fixed | Low | Low | High | Medium |
| Division of Amplitude by | Jamin | One-dimensional | Fixed | Variable | Fixed | Medium | High | Low | Medium |
| Reflection | Mach-Zehnder | Two-dimensional | Variable | Variable | Variable | Medium | High | High | Large |
| Polarization | Lebedev | Two-dimensional | None | None | None | High | High | Low | Small |
| Diffraction | Zernike Phase Contrast | Two-dimensional | None | None | None | High | High | Low | Small |

0 0 0 0 3 6 0 3 9 9 1



because different parts of a single mode laser beam separated longitudinally or laterally possess a high degree of phase correlation at macroscopic distances. Spurious interference patterns due to diffraction are, however, often encountered with the use of laser light.

B. Rayleigh Interferometers

The Rayleigh interferometer is the principal instrument of present interest which employs division of wavefront. Associated with this principle of operation are usually a large instrument size and low image intensity, because the division of wavefront has to occur at a large distance from a small source in order to result in two coherent waves. According to the Van Cittert-Zernike theorem (16), the diameter D of the region illuminated almost coherently by a uniform, quasi-monochromatic circular source of radius r and mean wavelength $\bar{\lambda}$, located at a distance R is

$$D = \frac{R}{r}\, 0.16\bar{\lambda} \qquad (11)$$

According to Eq. 11 a double slit of 5mm spacing would have to be located at least 286cm from a source of 1mm diameter, illuminated by green mercury light.

In its classical form (14), illustrated in Fig. 9, the Rayleigh interferometer can be used only for refractive index determinations of homogeneous specimens, and is therefore more properly called an interference refractometer (23,151). A double slit C illuminated by a small source A produces two coherent beams which are made parallel by lens B. Super-position of the two mutually inclined beams by lens G results in interference fringes parallel to the intersection of wavefronts in the image H of the source. The spacing of interference fringes is determined by the angle between the interfering beams, and infinite fringe spacing can not be achieved. Any change in the optical path length of the specimen

beam with respect to the reference beam results in a lateral displacement of the interference fringes. This shift is either measured by a filar eyepiece I or is restored by the rotation of two mutually inclined glass plates in a Jamin compensator E(141,54). Apart from its early application in refractive index measurements of gases, the Rayleigh interference refractometer has been used for differential measurements between selected narrow regions in a concentration field resulting from diffusion (113).

By the addition of a cylindrical lens (109), the Rayleigh interferometer can be used for the observation of one-dimensional refractive index fields (51,94). The resulting arrangement is shown in Fig. 10. The purpose of the cylindrical lens F is to focus the specimen in combination with the spherical lens E in the direction in which refractive index variations occur (e.g. vertical) without disturbing the formation of Rayleigh interference fringes. The slit source remains focused in the direction normal to the first one (e.g. horizontal) by lenses B and E with the cylindrical lens acting as a plano-parallel plate. Refractive index variations along the vertical direction of the cell result in a localized horizontal displacement of the vertical interference fringes (H).

An example of the resulting interferograms is shown on the left side of Fig. 11. The interference fringes on the right side represent the refractive index derivative. Such fringes have been obtained by mechanical (134) or purely optical (135) differentiation.

The basic Rayleight interferometer can be modified in many ways. A simplification consists in omitting the second spherical lens E. Source A is then focused on the image plane G by lens B alone. As a result, the object is traversed by a slightly converging light beam. Without the cylindrical lens, this arrangement is also called the Young interferometer. The use of a single spherical lens can be combined with that of a parallel

0 0 0 0 3 6 0 0 9 9 2



beam by placing a plane mirror behind the cell (109). Characteristics of the resulting double-pass instrument have been discussed in Section A above. A greatly increased image intensity can be obtained by the use of multiple light sources (137). These multiple sources (slits or pinholes) are arranged in such a way that the interference pattern due to each source alone is in registry with that of the neighboring source. Thus, in contrast to the small number of fringes with decreasing intensity from the center, obtained with a single source (23,154), a large number of fringes of equally high intensity can be obtained. A schematic of a multiple source instrument which also employs double light pass through the cell is given in Fig. 12 (108). Lens D, since it is traversed in both directions, serves the purpose of the two lenses B and E in Fig. 10. Because the cylindrical lens is now part of a magnifying system of the primary interferogram, its axis is at right angles to the one shown in Fig. 10. An example of an interferogram from an instrument with 162 point sources is given in Fig. 13 (62). A modified Rayleigh interference refractometer with three apertures has been reported for the resolution of very small optical path changes (0.001$\lambda$) by electro-optical means (76).

C. Jamin Interferometers

The Jamin Interferometer employs division of amplitude by reflection from front and back of a plano-parallel glass plate. Like the Rayleigh interferometer, it has originally been used as a refractometer for uniform media (14). The same compensator can be used for both. Characteristics of the two refractometers have been compared by Kuhn (83). By the addition of a cylindrical lens, as with the Rayleigh interferometer, one dimensional refractive index fields can be observed. The schematic of such an instrument is given in Fig. 14 (64). A collimated beam from a vertical slit C (Fig.14) is reflected from front and back sides of a

plano-parallel plate D. The resulting two beams traverse object and reference cells E and are re-united by plate F, identical to D in thickness. Diaphragm G selects the desired reflections. The spherical lens H images the source (and therefore the interference fringes) in the vertical direction, the cylindrical lens I with vertical axis images the object in the horizontal direction without disturbing the formation of interference fringes which originate at infinity. Interferograms obtained with this instrument are given in Fig. 15.

A detailed theory of the Jamin refractometer (without cylindrical lens) has been given by Schoenrock (123). He shows that horizontal interference fringes which are straight, evenly spaced and of low interference order can be produced by tilting the Jamin plates around a horizontal axis with respect to each other. Rotation of a plate around a vertical axis is found to displace horizontal fringes in a proportionate way and has been used in a compensating Jamin interferometer (2). Usable vertical interference fringes cannot, however, be produced this way. The introduction of two tilted plates as additional optical elements has been described by Antweiler (3) for producing vertical interference fringes with a Jamin interferometer. The Jamin plates are aligned parallel to each other in this arrangement and a cylindrical lens provides an image of the cell in the vertical direction.

Several modifications of the Jamin interferometer have been proposed by Lotmar (96) who also described the construction of a compact single plate, double pass instrument (97) schematically shown in Fig. 16. Interferograms of a diffusion experiment observed with this equipment are shown in Fig. 17. Operation with Jamin plates in parallel position has been reported by Antweiler (1). A spherical lens with a large depth of field (small relative aperature) is employed to simultaneously bring cell

0 0 0 0 3 6 0 0 9 9 3



and interference phenomenon into focus. In this mode of operation, illustrated in Fig. 18, a homogeneous specimen appears of uniform intensity and interference fringes form only in regions of varying refractive index. Variations smaller than those necessary for a change in optical path by a full wavelength manifest themselves in gradual intensity changes. The resulting image resembles one obtained by Schlieren techniques, which has led to the term "interferometric Schlieren system" for this mode of operation (which can be achieved with other interferometer arrangements too). The term "interference contrast" seems more appropriate, because the local image intensity is still a measure of refractive index, not refractive index derivative, as in Schlieren pictures.

The plano-parallel Jamin plates are responsible for the fact that the interference fringes originate at infinity, because interfering rays leave the plate assembly parallel to each other. Replacing the Jamin plates by wedge-shaped plates provides a means of moving the virtual origin of the interference phenomenon to a finite distance. This possibility is realized in the Sirks-Pringsheim interferometer (14,80), which employs plates with vertical apex (Fig. 19) that result in vertical interference fringes. Their virtual origin C can be placed inside the object B by slight rotation of one of the plates around a vertical axis. Possibilities for application of this instrument remain largely unexplored.

Wedge-shaped Jamin plates are also employed in the Dyson interference microscope shown in Fig. 20 (8,37,80,128). The beam splitting plate B provides a reference for each ray passing through the object by reflection on a totally reflecting center section. Reference rays pass through the periphery of the specimen and are united with the corresponding specimen rays by plate D. The purpose of the element E with spherical reflecting surface is to produce an image of the object in the non-reflecting center

part of the surface. This image is accessible for examination by a high-power (short working distance) microscope objective F. Translation, rotation and tilting of plates B and D provide for the manipulation of interference fringes, including observation with interference contrast (infinite fringe spacing). Although the Dyson interference microscope offers some attractive features for purposes of interest here, no applications in this area seem to have been reported.

Although light intensities achieved with Jamin interferometers are inherently greater than those of a Rayleigh interferometer, it may be desirable to increase intensity. This could be necessary for observing transient phenomena or to compensate for restrictions in the observed area in order to maintain one-dimensionality of concentration profiles. A simple means to increase the light output, which does not seem to have received much attention, consists in altering the reflectivities of the Jamin plate surfaces. The plates normally employed have no coating on their front which results in a reflectivity of about 4% (89). The solid mirror coating on the back can be assumed to have 95% reflectivity. As illustrated in Fig. 21a, the reflection of a beam from such a plate results in highly uneven intensities of the first two reflected beams which are used in an interferometer. Equal intensity in these two beams can be achieved by a uniform coating on the front side of the plate (Fig. 21b). However, the total optical power contained in the two is now lower with the balance being wasted in higher order reflections. These losses can be reduced by applying a coating over only part of the front surface in such a way that the incident beam is divided by the coating while the first reflection from the back of the plate exits through the uncoated section (Fig. 21c). Application of an anti-refection coating to this section would result in a further gain of about 3%.

0 0 0 0 3 6 0 0 7 9 4



Combinations of the above Jamin beam splitting plates with identical beam uniter plates are illustrated in Fig. 22. It can be seen that the simple coating of the front faces (b) can result in an almost 4-fold increase in the intensity available as compared to the uncoated case (a). Partial coating results in an 8-fold improvement.

The principal advantage of the Jamin interferometer is its simple, compact construction. The instrument is surprisingly insensitive to vibration, easy to operate and provides good light intensity. These advantages primarily derive from the stiff connection between two mirror-pairs (front and back side of Jamin plates) which is also the cause of the main shortcomings of the design: the separation of the two coherent beams is limited by the thickness of available plano-parallel glass plates and the interference fringes are localized at infinity. The aspherical lens system bridges the gap between the finite object distance and the infinite fringe origin by sacrificing one coordinate direction of the object geometry. Only one-dimensional concentration fields (like in the Rayleigh interferometer) can therefore be investigated. Any significant variation in the refractive index profile over the area observed would result in a blurring of all interference fringes (which are replicas of each other). In many electrochemical applications, one-dimensional refractive index fields can be produced (at the expense of light intensity) by restricting the observed area to a sufficiently narrow region with an optical slit. In order for refractive index variations to result in lateral interference fringe displacements, the refractive index gradient should be parallel to the direction of the fringes.

Care must be taken in orienting the axis of the cylindrical lens normal to the interference fringes. Its rotation around the optical axis

can result in distortions of the interference fringes which have not been adequately investigated.

D. Mach-Zehnder Interferometers

The four-plate or Mach-Zehnder configuration is probably the most versatile interferometer for the observation of refractive index fields. This instrument has been extensively used in heat transfer (32) and wind-tunnel measurements were usually large areas have to be observed (46,125). The primary characteristic of the Mach-Zehnder interferometer is that it allows one to arbitrarily orient, space and localize the interference fringes. Fringes and object can simultaneously be brought to focus with ordinary spherical lenses and, thus, two-dimensional refractive index fields can be observed.

The classical arrangement of components is shown in Fig. 23. Collimated light from a point or extended source A is divided by a partially reflecting mirror E (division of amplitude). The resulting mutually coherent beams pass through object and reference chambers I and F and, after reflection by the completely reflecting mirrors G and H, are united by another partially reflecting plate J. An objective lens K forms an image of the object I, together with the interference pattern, on the film plane L. The light throughput is optimized by use of multi-layer dielectric coatings with negligible absorption on the beam splitting and beam uniting plates. The position of the objective lens K after the beam uniter plate J introduces a large separation between object and objective, a configuration which is necessary for the observation of large objects but is not favorable for high optical resolution.

When used with conventional light sources, alignment of the instrument requires the use of elaborate procedures (57,156) in order to insure that light emitted at a given instant from any point of the source A, after traversing one arm EGJ of the interferometer, arrives at the same

0 0 0 0 3 6 0 0 7 9 5



point at the same time in the image plane L as the light which had traversed the other arm EHJ. Otherwise, due to the time and space dependence of the phase of light emitted from an incoherent source, no interference phenomena can be observed. One can imagine that the adjustment of the four mirror plates E, G, H and J, with their many translated and rotatory degrees of freedom, to satisfy the above requirements, is no small task (47,86,155). The reference cell F serves to equalize the optical path length of the two interfering beams, which should be the same within a fraction of a wavelength, if white light is to be used, and can be different by as many as a hundred wavelengths with typical monochromatic sources. The colorless zero order interference fringe, resulting from the use of white light, is used to establish fringe displacements across unresolved steep gradients or discontinuous boundaries (121). The large separation between specimen and reference beams, another characteristic of the Mach-Zehnder interferometer, results in large-sized instruments which often have to be placed on massive foundations to reduce the effect of vibrations on the stability of optical components.

Detailed analysis of the Mach-Zehnder interferometer can be found in the literature (11,55,75,121,156). Qualitatively, the formation and localization of interference fringes, characteristic of extended light sources, can be explained with the help of Fig. 24 (14,55). A coherent pair of sample and reference beams can be arranged to enter the objective lens K slightly displaced and mutually inclined with respect to each other. Their common virtual origin P determines the localization of the interference phenomenon, which can be made to coincide with the object. Orientation and spacing of the interference fringes are determined by the angle between the two beams. Let $W_1$ and $W_2$ represent mutually

coherent wave fronts in specimen and reference beams originating from the same wave front before division by the beam splitter. For the formation of low-order interference fringes in the object, the interferometer plates are adjusted in such a way that the virtual location $W_1'$ and $W_2'$ of the two corresponding wave fronts intercept in the virtual origin P of the interference phenomenon. The image formed in the film plane L then shows a bright interference fringe at the image P' of P oriented parallel to the line of intersection of $W_1'$ and $W_2'$ with neighboring dark and bright fringes determined by the local separation between the two wave fronts, similar to the interference in a tapered film. Infinite fringe spacing, (interference contrast), is obtained with $W_1'$ and $W_2'$ parallel to each other.

The use of laser light sources greatly reduces the alignment requirements of double beam interferometers. Any part of the cross section of a single mode laser beam interferes with any other part of that cross section, due to the complete lateral (also called spacial) coherence of such a beam. At the same time, the great longitudinal (also called temporal) coherence of laser light makes it possible that large path differences between the two arms of an interferometer (meters for a He-Ne laser) can be tolerated without noticeable decrease in the contrast of interference fringes.

A modified Mach-Zehnder interferometer, which takes advantage of the flexibilities offered by the use of laser light (6), is illustrated in Fig. 25. In contrast to the conventional version of the instrument, the beam-splitting plate has been omitted and the two mutually coherent light beams are derived from the opposite ends of a helium-neon gas laser B, placed in one arm of the interferometer and adjusted for single-mode

0 0 0 0 3 6 0 0 9 9 6



output. This arrangement results in a compact construction which is not sensitive to vibration. The location of the objective F between specimen E and beam uniter plate G allows the use of lenses with high numerical aperture (and associated resolution) close to the object, but necessitates the use of a reference lens H to provide a reference beam of a convergence equal to that of the object beam. Since high contrast interference fringes are obtained with unequal path between the two coherent beams, the reference cell could be omitted. As a result, the interferometer can be used in a travelling mode, e.g. for scanning boundary layers in a flow channel with its inadvertently varying dimensions, without continuous adjustment of a reference cell.

A common problem in the use of laser light is the formation of spurious diffraction patterns due to light scattering from optical imperfections, such as dust particles, anywhere in the light path. A diaphragm I (Fig. 25), which acts as a spacial filter and is located in the convergence plane of sample and reference beams, serves to attenuate such scattered waves, since they do not come to a focus in this plane. If, in order to eliminate undesired interference patterns, the diaphragm has to be closed sufficiently to impair the geometric resolution of the objective, a slit can be used with its long dimension in the direction in which the full resolution of the lens (presently $5x10^{-4}$ cm) is desired.

The fringe pattern is photographed by a camera back J with focal plane shutter. Due to the high light intensity available from even a low-powered laser, exposure times of $10^{-3}$ sec have been found sufficient for a film of intermediate sensitivity (Kodak Plus X). Beam expanders have later been added between mirrors A,D and C,G in order to enlarge the area of uniform intensity in the center of the beam (7).

Interferograms obtained with the laser interferometer sketched in Fig. 25 are shown in Fig. 26. They illustrate the development of an electrochemical mass transfer boundary layer under laminar forced convection conditions, with copper being deposited from a 0.1 M copper sulfate solution at 66 mA/cm$^2$. It can be seen that, 2 seconds after the beginning of electrolysis, the boundary layer is still growing. After about 8 seconds a steady state concentration profile is reached, which is the same as that shown after 20 seconds.

Ease of operation and high geometrical resolution have been achieved in a special way in another variation of the four-plate interferometer principle, the Leitz-Horn interference microscope, schematically shown in Fig. 27. The mirror surfaces are provided by two sets of prisms A and D which accomplish a superposition of the images of two identical microscopes, one looking at the object, the other at a reference (8, 43,80). Matched microscope objectives of numerical aperture up to 1.36 can be used in this equipment resulting in a diffraction-limited resolution of about 0.25 microns. Specimen and reference beams are 6.2cm apart. Compensators, located in both arms of the interferometer between prism A and condenser B as well as between objective D and prism E (133) provide for equalizing the optical path in both arms of the interferometer for use of white light and allow the user to arbitrarily space and orient interference fringes.

E. Michelson Interferometers

The Michelson interferometer, schematically shown in Fig. 28, employs the same partially reflecting plate B for beam splitting and uniting. By its nature, the instrument is of a double-pass type with large separation between sample and reference beams. Different interference

0 0 0 0 3 6 0 3 9 9 7



phenomena can be observed (5,130) which have been analyzed quantitatively (132,142). Of interest here are fringes of equal thickness or Fizeau fringes, originating near the virtual locations of the mutually inclined sample and reference mirrors and running parallel to the line of intersection between them. These fringes are similar to thin film interference in an air wedge formed by the two mirror surfaces E and D', provided that the difference in phase change between internal and external reflection on the beam splitter B is properly considered. However, the fringe profile shows a strictly sinusoidal intensity distribution, characteristic of double beam interference.

In order to equalize the optical path through glass in both arms of the interferometer, necessary for use of white light, a compensating plate G of equal thickness and dispersion as the beam splitter B can be added (41). With identical path length in both arms a colorless, zero order fringe is then observed with white light in the center of the field of view (or over the entire field with parallel plates). In contrast to Michelson's original arrangement, a collimated light source is commonly used now (132). With a sufficiently small source the interference phenomenon can be de-localized to appear in focus together with the object F.

Many modifications of the Michelson interferometer have been reported (5,143). Among them, the Twyman-Green interferometer is extensively used for the testing of optical components. The Zeiss-Linnik interference microscope for examining reflecting surfaces will be discussed in a later section. Despite its popularity in many applications, the Michelson principle has been rarely used for the observation of refractive index fields in fluids.

F. Polarizing Interferometers

The birefringence (double refraction) of optically anisotropic media can be used to produce two coherent light beams. Devices of principal interest for this purpose (35,133) are the Savant plate (147) which produces two parallel beams and the Wollaston prism (71) which produces two divergent beams as shown in Fig. 29. The two resulting beams are polarizing at right angles to each other. In order to bring two cross-polarized beams to interference, mutually parallel components of the electric vector have to be selected for superposition. Polarizing elements (filters or prisms) are used for this purpose as polarizers and analyzers on both sides of the beam splitters.

A large number of interferometer designs based on the above beam splitters and their modifications have been developed in recent years (37,42). In many of these instruments, the phase in the image of the object is compared with that of another image of the object rather than with that of a reference object. Interferometers of this type are also called shearing interferometers (18,139). They are widely used in optical testing (59, 133, 146) in order to avoid the use of a percise reference component. The two images may show an angular or a linear displacement (shear). If the lateral displacement is larger than the object, a blank area in the object plane may serve as a reference. If the displacement of the two images is smaller than the geometrical resolution of the optical system, a differential interferogram, indicative of the optical path gradients, results. Linear shear in the axial direction results in the superposition of a sharp image of the object with one which is out of focus. The local phase of the latter represents an average of an extended area of the specimen and may therefore be uniform (80,133). An inadvertent axial shear, due to an optical path difference between ordinary and

0 0 0 0 3 6 0 0 9 9 8



extraordinary rays in the beam splitter, is often associated with lateral shear. Radial shear (58,59,129) employs two concentric images of different magnification. Rotational and folding shear are also used (131). Different kinds of shear are illustrated in Fig. 30. They are associated with different ambiguities in the interpretation of results (80).

The Lebedev interference microscope (also called Jamin polarizing interferometer) employs a beam splitter with lateral shear. It is available in several commercial forms and is shown schematically in Fig. 31 (8,30). A birefringent crystal plate C provides a lateral shear (like a Savart plate), which depends on the thickness of the plate and is chosen depending on the power of the objective lens, (typically 50-500μ). A half-wave retardation plate D rotates the plane of polarization of both beams by 90° so that they are re-united in a symmetrical way by a second identical crystal plate F. In an early electrochemical boundary layer study, the lateral beam separation has been large enough to have the object illuminated entirely by the extraordinary beam. Straight interference fringes have been introduced with a quartz-wedge compensator (119).

The Smith interference mocroscope (Fig. 32) is based on the use of Wollaston prisms as beam splitters. The Nomarski interferometer is a variation of this principle for use with high power objectives (44,103). It produces a differential interferogram and can also be adapted for use with reflected light. Another modification for the simultaneous recording of concentration and concentration gradient profiles has been reported by Weinstein (153). Wallaston prisms can also be used for the observation of macroscopic objects (42), larger than the size of the prisms. Equipment of this type for the use in gas dynamic studies has been described by Oertel (104).

Polarizing beam splitters can also be used for producing a double image in the eyepiece of a microscope (8,37,80). In another form of polarizing interferometers beam splitting is achieved by the use of double focus lenses, made from birefringent materials (30,44,52,129).

G. Gouy Interferometer

The Gouy interferometer probably requires the smallest instrumental effort of any interferometer (48). Interference is due to the superposition of different parts of a beam which have been deflected by a refractive index field. The technique could be classified as an interferometric one, employing division of amplitude, but, in part, it is also a Schlieren technique, because it employs light deflection.

The schematic of an instrument employing parallel light through the specimen is shown in Fig. 33. Refractive index variations in the object D, typically due to a diffusing boundary, cause locally varying light deflection (50,51). Equally deflected beams, from symmetrical parts of the boundary, are superimposed in the focal plane F of the objective E. Depending on their phase difference, a dark or bright interference fringe results. If lens E is omitted, the object can be made to be traversed by converging light.

A detailed analysis of fringe formation has been given by Gosting and Kegeles (73), and experimental tests of the technique have been performed by Longsworth (92). The general use of the Gouy interferometer is restricted by the requirement that the refractive index profile in the object be symmetrical and its general shape be known for the interpretation of results.

0 0 0 0 3 6 0 0 9 9 9



H. Diffraction Interferometers

Different orders of diffracted light coming off a diffraction grating (Fig. 34) are mutually coherent and can therefore be used for interferometry (91). Gratings of the reflection or transmission type may be used. They should be blazed in such a way as to concentrate the light flux in the desired diffraction orders. A diffraction interferometer employing four transmission gratings in a collimated monochromatic light beam is sketched in Fig. 35 (151). The gratings are analogous to the four plates of a Mach-Zehnder interferometer. The beam splitting and uniting gratings D and I work in plus and minus first order, the beam deflection gratings F and E in second order. Two gratings in a converging beam have been used in the original Kraushaar diffraction interferometer (77) and a later modification of it (106). For complete separation of adjacent diffraction orders it becomes necessary under these conditions to superimpose zero and first order beams resulting from the extreme angles of incidence (151) (Fig. 34b).

The principal advantage of diffraction grating interferometers, apart from low cost, seems to be that the alignment of gratings is much less critical than that of corresponding mirrors. Weinberg (151) has shown that the two types of beam splitters differ by a factor of at least 368 in sensitivity to angular misalignment. Low optical speed, due to the poor efficiency of gratings, is one of the shortcomings of grating interferometers, an other is the appearance of spurious interference fringes due to grating imperfections (151). Although fringe spacing can be controlled by a tilting of gratings, the condition of interference contrast can, therefore, usually not be achieved. The combination of a diffraction grating with a double beam interferometer and its use for

adjusting zero path difference has been analyzed by Kahl and Sleator (72).

Diffraction in the object is the beam-splitting process employed in the Zernike phase contrast microscope. Phase and amplitude of diffracted and undiffracted light are altered in such a way that interference of the two in the image results in intensity variations which are sensitive to small local phase variations in the object. Thus, the diffracted light from a phase object is converted to simulate that of an amplitude object. Several detailed analyses of phase contrast principles (10,157, 158) as well as more qualitative discussions(9,36,127) are available in the literature. The schematic of a commonly used form of phase contrast microscope is given in Fig. 36 (8). An annular diaphragm A in the focal plane of the condenser B provides a hollow cone of illumination on the object C. Undiffracted light, originating from a given point in diaphragm A (solid lines), passes as a parallel beam through the object, while diffracted light (dashed lines) is deflected in the object. In the rear focal plane of the objective lens, the undiffracted light forms an image of the annular diaphragm while most of the diffracted light passes through other parts of this plane. The spacial separation of diffracted and undiffracted light makes it possible to adjust relative amplitude and phase of both by means of an annular phase plate. Typically, the undiffracted light is attenuated by partial absorption and advanced in phase by a quarter wavelength. Superposition of diffracted and undiffracted light in the image plane F then results in an interference contrast picture. Variations in intensity repeat themselves with every increment of one wavelength optical path difference in the object. Since interference fringes cannot be introduced at will in the picture to resolve ambiguities of interference order, and estimating fractional orders requires local photometry, the phase contrast microscope is not

0 0 0 0 3 6 0 0 0 0 0



particularly suited for quantitative analysis (150), although optical path differences of about $5 \times 10^{-4}$ wavelengths can be recognized (36). Nevertheless, the phase contrast principle has been used as a refractometer for the precise determination of $D_2O$ in $H_2O$ (69). A phase contrast telescope (120) can be used for the observation of large objects.

Division of amplitude by diffraction is also employed in holographic interferometry, which will be discussed in the chapter by Srinivasan.

## 2. Interpretation of Interferogram

### A. Conventional Interpretation

In the conventional interpretation of interferograms, the changes in optical path length (or phase) of the light through a specimen of fixed dimension are taken as a direct measure of local refractive index variations. Corrections to this first order approximation, due to light deflection and diffraction, are neglected in this approach and will be considered later.

As pointed out in discussing the capabilities of different interferometers, interferograms of most instruments can be classified as being obtained with either "finite" or "infinite" fringe spacing. Kinder (75 ) has compared interferograms of several objects with finite and infinite fringe spacing. The interpretation of both is different (53). In the first case, a field of continuously varying phase, generated by the instrument, is superimposed on the object and results in an interference pattern, typically straight fringes, with an object of uniform thickness and refractive index (47 ). A sketch of such a field is given in Fig. 37a. Any change in local phase due to the object is added to the predetermined instrumental phase variation and results in a displacement of interference fringes (Fig. 37b), because a different phase (interference order) is now associated with a given point in the image, and interference fringes represent lines of constant total phase. Since fringe displacement is a measure of optical path change due to the object, originally straight, equidistant fringes, deformed by a one-dimensional concentration field, can be interpreted as plots of concentration vs. distance (67 ). Why this interpretation is valid only for equidistant fringes

0 0 0 0 3 6 0 3 0 0 1



and one-dimensional refractive index fields can be seen with the aid of Fig. 37b, where the heavy lines represent the center of interference fringes, with the associated interference order noted in wavelengths. A fringe of zero order is arbitrarily chosen here. With white light, it would be the colorless high contrast fringe. Along a line AD, following the original straight fringe of zero order, the local interference order increases by one wavelength each, as successive fringes are intersected at points B, C and D and is the same as in points E, F and G, respectively. With the distance DJ equal to AG, etc. the local displacement of the zero order fringe is a measure of the local phase change. If all fringe spacings AE, EF etc. are equal, the curved fringe AJ represents a linear plot of interference order or phase, and to a good approximation of concentration c versus distance x. It must be remembered, however, that the curved fringe AJ represents the phase at the location of the fringe, and, only for a one-dimensional refractive index field is the local fringe displacement, eg. distance DJ, a measure of the local phase along the original, straight fringe, e.g. in point D.

The conventional evaluation of a two-dimensional interferagram, such as the one shown in Fig. 38, requires that one establish the local phase variation due to the object along a desired cross-section, preferably parallel to the original fringe pattern. Graphical interpolation techniques for this purpose have been discussed by Schardin (121).

With infinite fringe spacing (interference contrast), the interferogram of an object of uniform optical thickness is of uniform intensity throughout and can assume any value between constructive and destructive interference. Phase variations due to the object result in local

intensity variations which repeat themselves with each wavelength of optical path increase. As a result, interference fringes, which represent lines of constant phase change due to the object, appear. The interferogram of a concentration field, like the one shown in Fig. 37b for finite fringe spacing, is sketched in Fig. 39 for infinite fringe spacing. The concentration profile along a selected cross-section is derived in the familiar way from the interference fringes, which now represent concentration contours (Fig. 39b). The same procedure can be applied to two-dimensional refractive index fields, like the one shown in Fig. 40.

The reconstruction of three-dimensional refractive index fields from (two-dimensional) interferograms presents special problems. A theoretical discussion has been given by Iwata and Nagata (70 ). Some fields of rotational symmetry have been analyzed by decomposing them into concentric layers of finite thickness and numerically integrating the optical path length (155,121). In an effort to provide additional data of a three-dimensional object, focusing refractometry has been employed to obtain refractive index profiles at a cell wall (7 ). More generally applicable methods, such as the use of simultaneous interferometric views from different directions, possibly by holographic techniques, need to be developed.

The resolution of interferometric refractive index determinations depends on what minimum change in interference order can be detected. With finite fringe spacing, a fringe displacement of 0.1 fringe separations can usually well be detected visually. The unaided estimation of fractional orders with infinite fringe spacing is more

problematical. In either case, interference colors, resulting from the use of white light, provide increased visual resolution of small phase variations. Tables of interference colors (40 ) show that in the more sensitive regions of the color series, changes in optical path of 10nm (approx. 0.02λ) result in distinct color changes. However, the dispersive properties of the object will have to be considered under these circumstances (23,26 ). Apart from noise due to optical imperfections, photographic grain etc., the gradual intensity variation across a double beam interference fringe is often responsible for some uncertainty in defining fringe position. Photographic processes are available to introduce steep flanks or equidensity lines in the fringe profile (78,82, 88 ). Photoelectric scanning devices, which resolve a fringe pattern into finite density increments, have recently become available to serve a similar purpose more quantitatively. A resolution of 0.01λ should be expected from such instruments. The direct photometry of interference fringes has been shown to resolve optical path differences of 0.001λ (76 ). Microdensitometry of photographed interference patterns can yield a similar resolution.

According to Eq. 3,

$$\Delta n = \frac{\Delta p}{d} \tag{12}$$

the minimum resolvable refractive index variation Δn for a given resolution limit for the change in optical path length Δp is inversely proportional to the extent d of the object in the light propagation direction (cell thickness). Refractive index and concentration changes

resulting in an optical path change of a full wavelength are given in Fig. 41 as a function of cell thickness. The minimum resolvable refractive index or concentration variation would be 0.1 to 0.001 times the values indicated, depending on the resolution of fringe displacement.

B. Consideration of Light Deflection

a. Introduction

Valid refractive index profiles can often not be derived from interferograms by the conventional techniques of interpretation. The reason for this difficulty is that light does not propagate along a straight line in the presence of refractive index variations normal to the propagation direction. Errors due to this effect can be particularly large in condensed media, because large refractive index gradients are frequently encountered there. Errors in interferograms due to light deflection have been considered by several authors and found negligible. In part, the validity of such conclusions is limited to gaseous media (47, 155 ) and refractive index variations of small extent at a large distance from the imaging optics (20 ).

The physical reason for light deflection (or refraction) in refractive index fields lies in the dependence of propagation velocity on refractive index (Eq. 1) and is illustrated in Fig. 42. Different elements of a wavefront $W_1$ advance to different degrees in a time interval dt, resulting in a tilted wavefront $W_2$. Similarly, the direction of the wave normal $N_1$, which indicates the propagation direction of the wave or ray, is changed by an angle $d\phi$. The angle of deflection is proportional to the component of the refractive index gradient normal to the propagation direction and the distance over

0 0 0 0 3 6 0 0 0 0 2



which the light encounters this gradient

$$d\phi \sim \frac{\partial n}{\partial y} x \tag{13}$$

Eq. 13 is also the basis of Schlieren optics (122).

Light deflection results in two kinds of errors in an interferogram. The first is a geometrical distortion due to the lateral displacement and change in direction of transmitted light. The second error is a distortion of the measured refractive index, because the deflected light travels on a longer path and passes through regions of different refractive index.

b. Constant Refractive Index Gradient

For a one-dimensional, linear refractive index profile with planes of constant refractive index parallel to the incident beam, the geometrical light path, responsible for geometrical distortions, as well as the optical path length, responsible for refractive index distortions, can be derived in closed form. Since linear refractive index approximations can be used to gauge the magnitude of possible errors in more complex fields, some essential results are derived below.

Geometrical light path. One approach to calculate the light path in an isotropic inhomogeneous refractive index field of constant gradient is based on the principle of Fermat (13,60) which states that the medium is traversed by the light in such a way that the optical path length, or the time necessary for traversal is minimum. The light path can then be found by use of the techniques of variational calculus. Geometrical and refractive index coordinates to be used are defined in

Fig. 43. The optical path length is

$$\int n(y)\, ds \equiv \int n(y) \sqrt{\left(\frac{dx}{dy}\right)^2 + 1}\, dy = \min \quad . \qquad (14)$$

or, with Eq. 1 $n = c/v$

$$\int \frac{ds}{v(y)} \equiv \int \frac{\sqrt{\left(\frac{dx}{dy}\right)^2 + 1}}{v(y)}\, dy = \min \quad . \qquad (15)$$

Any extremum has to satisfy Euler's equation, i.e. for the integrand of Eq. 14

$$F(y) \equiv n\,(y) \sqrt{\left(\frac{dx}{dy}\right)^2 + 1} \qquad (16)$$

the condition for minimum is

$$\frac{\partial F}{\partial x} - \frac{d}{dy}\left(\frac{\partial F}{\partial \frac{dx}{dy}}\right) = 0 \quad . \qquad (17)$$

Inserting Eq. 16 in Eq. 17 results in

$$0 - \frac{d}{dy}\left(\frac{n(y)\,\frac{dx}{dy}}{\sqrt{\left(\frac{dx}{dy}\right)^2 + 1}}\right) = 0 \quad . \qquad (18)$$

Integration of Eq. 18 gives

$$\frac{n(y)\,\frac{dx}{dy}}{\sqrt{\left(\frac{dx}{dy}\right)^2 + 1}} = C_1$$

0 0 0 0 0 6 0 0 0 0 3



or

$$\frac{dx}{dy} = \frac{1}{\sqrt{\left(\frac{n}{C_1}\right)^2 - 1}}$$

therefore

$$x = \int \frac{dy}{\sqrt{\left(\frac{n(y)}{C_1}\right)^2 - 1}} + C_2 \quad . \tag{19}$$

For the special case of a linearly increasing refractive index, depicted in Fig. 43

$$n(y) = k\ y \tag{20}$$

the light path is determined as follows: insert Eq. 20 into Eq. 19 and change variables

$$\frac{ky}{C_1} = z \ , \ \frac{dy}{dz} = \frac{C_1}{k}$$

so that

$$x = \frac{C_1}{k} \int \frac{dz}{\sqrt{z^2 - 1}} + C_2$$

which can be integrated ( 29) to give

$$x = \frac{C_1}{k} \cosh^{-1} \left(\frac{ky}{C_1}\right) + C_2 \quad . \tag{21}$$

Since a general expression of the form

$$X = B \cosh^{-1} Y + C$$

is equivalent to

$$Y = \cosh \frac{X - C}{B}$$

one obtains from Eq. 21

$$y = \frac{C_1}{k} \cosh \frac{k(x - C_2)}{C_1} \quad . \tag{22}$$

The constants of integration $C_1$ and $C_2$ are determined with the initial conditions, which are

$$\text{for } x = 0 \text{ , } y = y_o$$
$$n = ky_o \equiv n_o \tag{23}$$
$$\frac{dy}{dx} = 0.$$

Insert Eq. 23 into Eq. 22

$$\frac{y_o k}{C_1} = \cosh \frac{-k\ C_2}{C_1} \tag{24}$$

Eq. 24 must be true for all values of k, for $k \rightarrow 0$

$$\frac{n_o}{C_1} = \lim_{k \rightarrow 0} \cosh \frac{-k\ C_2}{C_1} = 1$$

therefore

$$C_1 = n_o \quad . \tag{25}$$

With Eq. 23 and Eq. 25 it follows from Eq. 24 that

$$\cosh \frac{-k\ C_2}{n_o} = 1$$

and therefore, because $k \neq 0$ and $n_o$ finite

$$C_2 = 0 \quad . \tag{26}$$

0 0 0 0 3 6 0 6 0 0 4



Thus Eq. 22 for the curved light path becomes

$$y = \frac{n_o}{k} \cosh \frac{kx}{n_o} \quad . \tag{27}$$

the chain line Eq. 27 may be developed in a series

$$y = \frac{n_o}{k} + \frac{k\,x^2}{n_o\,2!} + \frac{k^3\,x^4}{n_o^3\,4!} + \frac{k^5\,x^6}{n_o^5\,6!} + \ldots. \tag{28}$$

or, with $y_o = n_o/k$

$$y = y_o + \frac{x^2}{y_o\,2!} + \frac{x^4}{y_o^3\,4!} + \ldots$$

A hyperbolic cosine function for the light path (60) and an equivalent formulation (47) can be found in the literature. An approximate form of Eq. 28 has been given by several authors (46,51,148). The angular light deflection $\alpha$, due to a refractive index gradient k normal to the propagation direction experienced over a distance x, is

$$\tan \alpha = \frac{dy}{dx} = \sinh \frac{kx}{n_o} \tag{29}$$

$$\tan \alpha = \frac{kx}{n_o} + \frac{k^3\,x^3}{n_o^3\,3!} + \frac{k^5\,x^5}{n_o^5\,5!} + \ldots \tag{30}$$

Due to refraction at the cell-air interface the inclination $\beta$ of a deflected beam, after entering into air (Fig. 44) is larger than the angle $\alpha$ given by Eq. 29 . Application of Snell's law for the angle of refraction then results in

$$\sin \beta = (n_o + ka) \sin[\tan^{-1} (\sinh \frac{kx}{n_o})] \tag{31}$$

where a is the lateral beam displacement at the cell exit given by Eq. 33 and $n_o$ is the refractive index where the beam enters the cell. Numerical data for α and β are given in Fig. 45. It can be seen that deflection angles of several degrees can be commonly expected. The current density, added in a separate scale to this figure and included on some of the following ones, results in interfacial concentration gradients of the magnitude indicated, under consideration of diffusion and migration in a 0.5M $CuSO_4$ solution ($D = 4.62 \times 10^{-6}$, $t_{cat} = 0.304$ (33,45 )).

The local lateral displacement of a deflected beam

$$a = y - yo \tag{32}$$

is indicated in Fig. 44. From Eq. 27 it is found to be

$$a = -\frac{n_o}{k} + \frac{n_o}{k}\cosh\frac{kx}{n_o} \tag{33}$$

$$a = \frac{kx^2}{n_o\,2!} + \frac{k^3\,x^4}{n_o^3\,4!} + \frac{k^5\,x^6}{n_o^5\,6!} + \ldots. \tag{34}$$

These equations can be found in the literature (67,87 ). Some computed data are given in Fig. 46. They show that for all but the thinnest cells, the lateral beam displacement a can easily exceed $10^{-2}$ cm, the order of magnitude of typical diffusion layers. Angular light deflection and lateral displacement will be used as input parameters in subsequent computations.

The curved light path in a linear refractive index field can also be derived by integation of Snell's law of refraction (66,87). For this

0 0 0 0 3 6 0 0 0 0 5



purpose, the refractive index field is divided into layers of constant refractive index with light refraction occurring at each boundary. Eq. 27 also results from this approach.

Optical path length. The optical path length p observed in the interferogram, is found for a deflected beam by integrating the geometrical path length s over the local refractive index n

$$p_2 = \int_0^x n \, ds \tag{35}$$

with Eq. 20 and Eq. 27

$$n = n_o \cosh\left(\frac{kx}{n_o}\right)$$

and

$$ds = \sqrt{1 + \sinh^2\left(\frac{kx}{n_o}\right)} \, dx$$

the optical path length becomes

$$p_2 = n_o \int_0^x \cosh^2\left(\frac{kx}{n_o}\right) dx \tag{36}$$

$$= \frac{n_o^2}{k} \left[\frac{1}{4} \sinh \frac{2kx}{n_o} + \frac{kx}{2\, n_o}\right]_o^x + C$$

Since for $x = 0$, $p = 0$, the constant of integration is $C = 0$. Therefore

$$p_2 = \frac{n_o\, x}{2} + \frac{n_o^2}{4k} \sinh \frac{2kx}{n_o} \tag{37}$$

Expansion in a series results in

$$p_2 = n_o x + \frac{1}{3!} \frac{2}{n_o} k^2 x^3 + \frac{1}{5!} \left(\frac{2}{n_o}\right)^3 k^4 x^5 + \ldots . \tag{38}$$

These expressions have also been given by Ibl ( 67 ), and the first two terms of Eq. 38 have been derived by Caldwell (19).

The error in optical path length, due to light deflection, is responsible for the error in concentration derived from an interferogram. The error can be defined most simply as the difference in optical path length p between the deflected beam 2 (Fig. 47) and a hypothetical undeflected beam either entering (beam 1) or leaving (beam 3) the cell at the same point as the deflected one. The resulting errors are

$$p_2 - p_1$$

and

$$p_2 - p_3$$

They can be expressed in number of fringe shifts by dividing the optical path length error by the wavelength of light. For one-dimensional, constant refractive index gradient fields, the error can be computed in closed form. With Eq. 37

$$p_2 = \frac{n_o x}{2} + \frac{n_o^2}{4k} \sinh \frac{2kx}{n_o}$$

and, according to Fig. 43

$$p_1 = n_o x \tag{39}$$

the first error is

$$\underline{p_2 - p_1 = -\frac{n_o x}{2} + \frac{n_o^2}{4k} \sinh \frac{2kx}{n_o}} \tag{40}$$

or

$$p_2 - p_1 = \frac{1}{3!} \frac{2}{n_o} k^2 x^3 + \frac{1}{5!} \left(\frac{2}{n_o}\right)^3 k^4 x^5 + \ldots \tag{41}$$

U U U U U 6 U U U U 6



The other reference optical path length is

$$p_3 = (n_o + ka)\, x$$

with Eq. 33

$$p_3 = n_o x \cosh \frac{kx}{n_o} \tag{42}$$

The second error therefore is

$$\underline{p_2 - p_3 = \frac{n_o x}{2} + \frac{n_o^2}{4k} \sinh \frac{2kx}{n_o} - n_o x \cosh \frac{kx}{n_o}} \tag{43}$$

or

$$p_2 - p_3 = -\frac{k^2 x^3}{3!\, n_o} + \frac{3k^4 x^5}{5!\, n_o^3} + \ldots . \tag{44}$$

Optical path length errors derived in the literature (34,114,138) cannot easily be compared with the above results. Numerical results of Eq. 40 and Eq. 43 are illustrated in Fig. 48. The fringe shifts given there can be related to refractive index (or concentration) errors by use of Fig. 41. In a 1 cm thick cell, for instance, an error of 100 fringes corresponds to an error in concentration of 0.2M. An important result of this analysis is that the two errors are of opposite sign. In order to place reliable limits on possible interferometric errors, however, the optical path length analysis will have to be further refined, as indicated below.

c. Effect of Focusing

The above analysis does not consider the effect of the imaging optics in an interferometer. The purpose of this optics is to bring a selected plane in the object to focus in the image. This plane is

optically conjugate to the image plane. It will be referred to in the following as "plane of focus", but should not be confused with the planes which contain the primary and secondary focal points of the objective lens. If light deflection occurs in the object, the image is determined by the virtual origin of the deflected light in the plane of focus. Under these circumstances the shape of the image can be expected to depend on the choice of the plane of focus. This effect is illustrated in Fig. 49 for a cathodic boundary layer with the electrode shadow as the object. A light beam C, entering the cell at the surface of electrode B and parallel to it, is deflected toward the bulk of the solution A and leaves the cell at point D. With the objective lens G focused on the cell wall facing the camera (Fig. 49a), the shadow of the cathode surface in this plane appears at D and its image in film plane I is H. Thus, the electrode shadow appears advanced into the solution side of the interface due to the presence of the refractive index gradient. Focusing on the cell wall facing the light source (Fig. 49c) results in a virtual origin L of the same deflected beam. The electrode shadow now appears receded into the electrode. For an intermediate focusing position (Fig. 49b), the virtual origin K of the deflected beam coincides with the electrode surface. The electrode shadow is, therefore, not displaced in the image.

In the schematic of Fig. 49, refraction at the cell exit as well as inside the cell wall has been neglected. Even in the absence of refractive index gradients, these effects result in an axial displacement of the virtual location E' of an immersed object E (Fig. 50). Since the light is assumed here to be incident normal to the first cell wall,

0 0 0 0 3 6 0 3 5 0 7



refraction in the second one (facing the camera) will only be considered.

The application of Snell's law (Eq. 45)

$$n \sin \varepsilon = n_g \sin \varepsilon' = \sin \eta \qquad (45)$$

results in Eq. 46 for the virtual location m of an immersed object (Fig. 50).

$$m = \cot \eta \; (w \tan \varepsilon + d \tan \varepsilon') \qquad (46)$$

For small angles $\varepsilon$ from the optical axis, this equation reduces to

$$m = \frac{w}{n} + \frac{d}{n_g} \qquad (46a)$$

w is the thickness of the medium of refractive index n and d is the thickness of the glass wall of refractive index $n_g$. Thus, a real plane of focus F inside the cell is transformed into a virtual plane of focus F' by refraction effects. (F' would be the real plane of focus in the absence of the cell, Fig. 50.) If the imaging optics of an interferometer are focused on an immersed target in plane F, a preferred experimental procedure, the image is determined by the virtual location of the target in plane F'.

The effect of focusing in the presence of light deflection is illustrated in Fig. 51 for an arbitrary plane of focus F in the cell (with associated virtual plane of focus F'). A deflected light beam ABC appears to originate from point E' with a lateral displacement g from its true origin A. This lateral displacement can be formulated as

$$g = a - (x - e) \tan \alpha \qquad (47)$$

Values for the variables a and $\alpha$ are obtained from Eqs. 33 and 29 respectively.

As Eq. 47 and Fig. 52 show, the lateral beam displacement g is independent of the thickness d of the cell wall for a given choice of the plane of focus F. Some typical results are given in Fig. 53. A positive displacement signifies a movement toward the solution side of a cathodic boundary layer, a negative displacement, a movement toward the electrode side. The results illustrate that the lateral displacement of the virtual beam origin (and therefore the geometrical distortion of an image) strongly depends on the location of the plane of focus and that it can assume values larger than the dimension of typical mass transfer boundary layers.

The location $e_o$ of the plane of focus $F_o$ (inside the cell) which results in no lateral beam displacement (e.g. no movement of the electrode shadow) in a medium of constant refractive index gradient can be calculated similarly (Fig. 54)

$$e_o = x - a \cot \alpha \tag{48}$$

The location of this special plane of focus is independent of the glass wall thickness. Thpical results of Eq. 48, given in Fig. 55, show that its position, very close to half way across the cell, is almost unaffected by changes in refractive index gradient. Although some geometrical distortions in boundary layers can be avoided by this choice of plane of focus, its use is not of great practical interest because it is difficult to establish and does not minimize errors of other parameters in an interferogram (e.g. local concentration) (7). Most of the analysis to follow will be restricted to focusing on an immersed object on the inside face of the cell wall facing the light source. (This is the preferred mode of operation for the observation of cathodic boundary layers (7) because it avoids the superposition of beams with different phase.)

0 0 0 0 3 6 0 3 0 0 8



The error in phase due to light deflection can be represented by the difference in optical path length between a deflected beam AC of length $p_4$ (Fig. 56) and a hypothetical undeflected beam EI of length $p_5$ passing through the same virtual origin E' in the virtual plane of focus. Points C and I lie on a circle centered in E'. Beyond points C and I, the imaging optics introduces no phase difference between both beams. The optical path length error for a point in the interferogram which corresponds to the image of E' is

$$p_4 - p_5 = (p_2 + \overline{BC}\, n_g) - [x(n_o - k\,\overline{AE}) + dn_g + \overline{HI}]$$

$$= \left(p_2 + \frac{d\, n_g}{\cos\left[\sin^{-1}\left(\frac{\sin\beta}{n_g}\right)\right]}\right)$$

$$- \left[n_o x - kx(x\tan\alpha - a) + d\, n_g\right.$$

$$\left. - \cot\beta\left(x\tan\alpha + d\tan\left(\sin^{-1}\left(\frac{\sin\beta}{n_g}\right)\right)\right)\left(1 - \frac{1}{\cos\beta}\right)\right] \quad (49)$$

As defined before, x and d are the thickness of cell and glass wall, respectively, $n_o$ and $n_g$ are the refractive indices at the light entrance into the liquid and inside the glass wall, respectively, k is the refractive index gradient normal to the direction of the entering light and $p_2$ is the optical path length of the deflected beam between points A and B. The values of $p_2$, a, $\alpha$ and $\beta$ have to be inserted from Eqs. 37, 33, 29 and 31, respectively.

The effect of an increase in glass wall thickness on the optical path length error is indicated in Fig. 57. By comparison with Fig. 56, the optical path $\overline{BC}$ of the deflected beam inside the glass wall is increased

more than the path $\overline{GH}$ of the undeflected comparison beam. However, the component $\overline{HI}$ of the latter is increased, so that the path difference between deflected and undeflected beams remains very closely the same. In effect, the independence of g, $e_o$ and $(p_4 - p_5)$ on wall thickness is achieved by a displacement of the imaging optics, necessary to keep the real plane of focus F in a fixed location while the thickness d is changed.

Some results of Eq. 49, expressed in fringe shifts, are given in Fig. 58. They illustrate that, for focusing on an immersed object at the entrance side of the light into the cell, the glass wall thickness is not an important source of optical path (concentration) error.

0 0 0 0 3 6 0 0 0 0 9



d. Nernst Boundary Layer Model

All the considerations of light deflection discussed so far have been based on an unlimited linear refractive index profile (Fig. 59a). For the consideration of light deflection errors in mass transfer boundary layers (Fig. 59c), the Nernst model (Fig. 59b) can be used as a first approximation. This model has the advantage in that analytical solutions of the kind outlined above can be employed. For deflected beams which remain entirely inside the boundary layer, the previous solutions are directly applicable. The discontinuous change of refractive index gradient at the edge of the boundary layer results in optical artifacts which, although generally more severe than with more realistic refractive index profiles, serve to illustrate some problems of light deflection in boundary layers.

Near the outer edge (solution side) of a Nernst-type boundary layer, a light beam propagates only over part of the cell depth $\ell$ within the boundary layer, as indicated in Fig. 60. The curved part AB can be described by the previously derived equations, while the straight part BC continues with the slope of the curve at point B. The lateral displacement b of a beam beyond the boundary layer can be derived by use of Eq. 30. Disregarding third order terms, it is

$$b = \frac{kx}{n_o} (\ell - x) \tag{50}$$

where x is the abscissa of point B (Fig. 60). The displacement b reaches a maximum value $b_m$ for a beam which leaves the boundary layer in the middle of the cell ($x = \ell/2$)

$$b_m = \frac{k\ell^2}{4\ n_o} \qquad (51)$$

For a beam DE, which travels entirely inside the diffusion layer, the lateral beam displacement $a_n$ is, according to Eq. 34, approximately

$$a_n = \frac{k\ell^2}{2\ n_{oo}} \qquad (52)$$

It can be seen from Eq. 50 that a pair of deflected beams 1 and 2 of different optical path exit at any point located within a distance $b_m$ outside the Nernst diffusion layer (Fig. 61). In addition, an undeflected beam 3 also passes through the same points.

The optical path length $p_9$ of a deflected beam near the edge of the boundary layer can be determined as the sum of the path lengths $p_7$ and $p_8$ of the curved and straight parts (Fig. 60). For focusing on the light exit side of the cell, the optical path difference between boundary layer and bulk, a measure of the local fringe shift, is

$$p_9 - p_{10} = p_7 + p_8 - \ell n_b \qquad (52)$$

An example of this computed optical path profile is given in Fig. 62, curve B. The superposition of three different fringe shifts, due to rays 1 to 3 shown in Fig. 61, immediately outside the boundary layer, can be expected to result in a superposition of different fringe systems in this region. To a good approximation, the linear part of the fringe runs parallel to the true refractive index profile.

3. Realistic Boundary Layers

Mass transfer boundary layers in convective diffusion show a refractive index profile of the shape illustrated in Fig. 59C. The refractive index gradient and, therefore, the degree of light deflection are largest

0 0 0 0 3 6 0 0 0 1 0



at the electrode and decrease continuously toward the bulk solution. The deflected light successively traverses regions of varying refractive index gradient and may, as seen in the Nernst model, enter the uniform bulk solution. Numerical techniques are best suited to analyze light propagation in such media.(7)

In order to compute an interference fringe pattern based on an assumed refractive index profile, the optical paths of a small number (10-20) of deflected beams, which enter the cell parallel to each other and usually parallel to the electrode surface, but at different distances from it, are determined. Each beam is divided into a large number (100-200) of straight segments, as schematically shown in Fig. 63b. The slope of a typical segment HJ is determined from the slope of the previous segment, the length of the segment, the refractive index $n_i$ at its center (Fig. 63a) and the component of the refractive index gradient in the direction normal to the beam at the center of the segment.

The optical path length of a deflected beam, including refraction KL in the cell wall, is obtained by summing the product of local refractive index $n_i$ and geometrical path length HJ of each beam element. From position and slope of the beam M leaving the cell, the virtual origin E' of the deflected beam in the virtual plane of focus is determined. The fringe shift in the interferogram relative to the bulk solution is due to the difference in optical path length between deflected beam GL and a hypothetical undeflected beam EO of the same virtual origin E', passing through a cell filled with bulk solution. Thus, phase and position of one point in the interferogram have been established. Repetion of this procedure with 10-20 beams yields a computed interference fringe.

Figure 64 illustrates how the above procedure can provide computed

interference fringes b to e for an assumed refractive index profile (a) with different choices of plane of focus. It can be seen that both boundary layer thickness and interfacial concentration are seriously falsified by the light deflection, and the error strongly depends on the choice of the plane of focus. A common observation with such computed interference fringes is that the location of the outside edge of the boundary layer is not affected by light deflection (except with very unfavorable focus as in Fig. 64e).

Observed interference fringes similar to the computed ones of Fig. 64 are shown in Fig. 65. The dependence of apparent boundary layer thickness and interfacial concentration on the choice of the plane of focus can be seen. The double value of phase, found in Fig. 64e seems to be responsible for the extraneous interference fringe system seen in Fig. 65c and d. This effect, due to the crossing of differently deflected rays, is best avoided by focusing on the side of the cell where the light enters (farthest from the camera).

The numerical analysis of light deflection in refractive index fields can easily be adapted to investigate the effect of other parameters on the interferogram. For instance, the effect of misalignment of the cell, with the light not incident parallel to the electrode surface has been described.(7)

Due to the large number of variables involved in the numerical analysis of light deflection in refractive index fields, it is difficult to generalize results. An attempt has been made in Figs. 67-69 to correlate data which should allow an experimenter to estimate interferometric light deflection errors under a wide range of experimental conditions for three quantities: interfacial concentration, interfacial

0 0 0 0 3 6 0 3 0 1 1



concentration gradient and boundary layer thickness. The computations have been based on a refractive index profile of the algebraic form given in Eq. 53 for a cathodic boundary layer of constant thickness $\delta$ (0.4 mm), constant bulk refractive index $n_b$ (1.3468) and variable interfacial refractive index $n_i$ (1.333 - 1.345). ($\partial n/\partial c = 0.027$ $(M\ CuSO_4)^{-1}$ for all computations).

$$\frac{n - n_i}{n_b - n_i} = 1 - e^{-Y^2}\left[\frac{A}{1 + BY} - \frac{C}{(1 + BY)^2} + \frac{D}{(1 + BY)^3}\right] \qquad (53)$$

This profile (an approximation to an error function complement) has been found to approximate a boundary layer under convective diffusion (7). In Eq. 53, n is the refractive index at a distance y from the electrode surface. The dimensionless distance Y from the electrode is

$$Y = \frac{y}{\delta} \qquad (54)$$

where $\delta$ is a mathematical boundary layer thickness. Physical boundary layer thicknesses of different definition can be determined from Fig. 66. The quantities used for the other parameters in Eq. 53 are

$$A = 0.34802 \qquad B = 0.47047$$

$$C = 0.09588 \qquad D = 0.74786$$

Concentration profiles employed in the computations are given in Fig. 66. All the results presented in Figs. 67-69 hold for focusing on an object located at the inside of the cell wall farthest from the camera. This procedure largely compensates for the effects of variable cell wall thickness. The scatter of points is due to the graphical evaluation of computed interference fringes, made up of a limited number of points.

The error in concentration at the interface is shown in Fig. 67. For a 2 mm thick cell, the error is unexpectedely negative and amounts

to at most -8% of the bulk concentration. This error is 2/3 of the largest one computed for an unlimited linear concentration profile (Fig. 58). For the 1 cm cell, the error changes sign and increases up to 16% with increasing current density, which is much less than the error shown in Fig. 58.

The error in concentration gradient at the interface, shown in Fig. 68, is at most 1% for the 2 mm cell and up to 50% for the 1 cm cell. Because of the parallel displacement of the interferogram near the interface due to refraction in the glass wall, the influence of the wall thickness is expected to be very small.

Since, with the present choice of focal plane, the outside of a boundary layer (solution side) is normally not affected by light deflection, the error in boundary layer thickness (Fig. 69) is entirely due to the displacement of the electrode shadow, as demonstrated in Figs. 64 and 65. For a 1 cm cell, the error is comparable to the one calculated for a constant refractive index gradient (Fig. 53) at interfacial refractive index gradient 0.1, but only 1/5 at $k = 0.4$. In agreement with the previous results, the effect of cell wall thickness is not noticeable.

Similar to the analysis of a constant refractive index gradient, the position $e_o$ of the plane of focus $F_o$ inside the cell (Fig. 54) can be calculated, for which the image of the electrode (electrode shadow in interferogram) is not displaced by light deflection. Figure 70 gives some results. Compared to the previous computation (Fig. 55), the position of the plane of focus in the cell for zero electrode displacement is slightly closer to the entrance side of a 1 cm thick cell and slightly farther from it for the 2 mm thick cell.

0 0 0 0 3 6 0 0 0 1 2



It can be concluded that computations for a constant refractive index gradient often provide a reasonable estimate of light deflection errors in boundary layers.

For the precise interpretation of measured interference fringes as refractive index profiles, a second step has to be added to the above computations. Based on a comparison of observed and computed interference fringes, the assumed refractive index profile has to be modified to improve agreement between the two, and the computation is repeated. Several cycles are usually necessary to produce satisfactory agreement (7).

f. Anodic Boundary Layers

The considerations of the two preceeding sections have been restricted to boundary layers with refractive index decreasing toward the electrode surface. Boundary layers with refractive index increasing toward the electrode surface, such as those typically encountered in anodic metal dissolution, cause the light to be deflected toward the electrode. If all the light which strikes the electrode surface is adsorbed, rays entering the cell closer to the electrode than the lateral beam displacement do not contribute to the picture (Fig. 71b). In contrast to the cathodic boundary layers, an overlapping of differently deflected beams is now best avoided by focusing the cell on the plane where the light exits. If the electrode is sufficiently smooth, light which strikes the surface is reflected (Fig. 71c), and a much more complex optical situation exists, particularly if a reflected beam is deflected back to the electrode surface and reflected again.

## C. Diffraction Effects

The closest distance to an electrode, to which the composition of a solution can be determined by interferometry, is basically limited by light diffraction. For a two-dimensional (infinitely thin) object in

focus, the diffraction-limited resolution of a microscope is usually formulated as

$$r = 0.61 \frac{\lambda_o}{N.\ A.} \qquad (55)$$

where $\lambda_o$ is the light wavelength in vacuum and N. A. the numerical aperture of the objective lens defined as

$$N.\ A. = n \sin \theta \qquad (56)$$

n is the refractive index in the object space, $\theta$ the angle between the optic axis and the marginal ray entering the objective at its periphery. For coherent illumination, the numerical factor in Eq. 55 is 0.77 (15).

Even the simplest flat electrode is, however, of finite thickness, and diffraction effects can be expected to be more complex. The microscopic resolution limit is, therefore, usually not attained in electrochemical interferometry. Since a theory of diffraction from a planar object does not seem to be readily available, a dicussion of diffraction problems will have to remain largely qualitative.

Only a selected cross-section of an extended electrode can be in focus, with other parts being out of focus to various degrees. It is these defocused regions which are probably the most serious cause for degraded resolution due to diffraction in an interferometer. These regions can be expected to produce diffraction fringes similar to those observed behind a straight edge. Their real or virtual origin is projected in the plane of focus. The interaction of these diffraction fringes with the interferogram can result in local changes of geometry and apparent phase.

Amplitude and phase of a Fresnel diffraction pattern behind a straight edge can be derived from Cornu's spiral (71). An example is given in Fig. 72. It is important to keep in mind that across the diffraction

9 0 0 0 3 6 0 0 0 1 3



pattern, the phase varies continuously. Superposition with the continuously varying phase of an interferogram can, therefore, lead to quite unexpected results (Fig. 73). The distance of diffraction maxima and minima from the geometrical shadow depends on the distance behind the straight edge (degree of defocusing) as shown in Fig. 74. It can be seen that for a 1 mm defocusing, the separation between the first two intensity maxima is 0.02 mm. Such a diffraction pattern will be resolved by interferometers of interest here. If half the distance between the first diffraction maximum and the true location of the edge is taken as the uncertainty of the location of the edge, diffraction from one end of a 1 cm wide electrode, focused on the other end, introduces an uncertainty of electrode position of 0.003 cm. This distance is much smaller than the light deflection in the same cell under most conditions.

A more realistic appraisal of diffraction phenomena in interferometry, in addition to being based on a better theory of diffraction, will also have to include the effect of light deflection.

## 3. Applications

### A. Diffusion and Electrophoresis

The determination of diffusion coefficients by interferometric techniques involves the observation of the concentration profile which develops between two solutions of different concentration as a function of time. Evaluations of results with different degrees of sophistication can be found in the literature (25,27,85,136). A technique which is based on the observation of regions far removed from the liquid junction, where concentration gradients are small, and light deflection errors are more likely to be negligible, has been employed by Chapman (24). This technique is also unaffected by the sharpness of the initial junction.

Differential interferometers have been used for very low concentration differences between solutions at the liquid junction. The derivation of diffusion coefficents from such measurements is somewhat different (17,139).

Diffusion coefficients have been determined with different types of interferometers, among them Jamin-types (25,85), Rayleigh-types (20,27,93), Mach-Zehnder (19), Polarizing (17,111,139) and Gouy (28,49) types. Interferograms of diffusing liquid junctions are shown in Figs. 11, 13, and 17. Optical techniques for diffusion studies have been reviewed by Gosting (51).

Electrophoresis has lost some of its importance for the application of interferometry because the use of zone electrophoresis has been replaced to a large extent by paper electrophoresis. New developments, such as electrophoresis in free-flowing liquids (100) could, however, reverse the situation again. The evaluation of an electrophoretic separation observed with a Jamin interferometer is illustrated in Fig. 75 (74) A number of similar examples can be found in the literature (84, 98). A review of electrophoretic techniques has been given by Longsworth (95).

B. Mass Transport Boundary Layers

Boundary layers on working electrodes have been investigated by interferometry under forced (90) and natural (64,65) convection conditions, as well as in the absence of convection (62,144,145). Interferometers employed in these studies include Jamin (64,65), Mach-Zehnder (90,144,145) and Rayleigh (62) types. Interferograms of mass transfer boundary layers have been shown in Figs. 15, 18 and 26. Data on boundary layer thickness and interfacial concentration, derived from interferograms, are given in Figs. 76 and 77. While concentration profiles derived by the conventional method at low current densities are close to those expected (Fig. 78), deviations found at higher current densities (90) could well be due to light deflection effects. A displacement of the electrode shadow at high

0 0 0 0 3 6 0 0 0 1 4



current densities has been demonstrated (145). In the presence of a supporting electrolyte, the interferogram represents a superposition of two boundary layers which possess opposite concentration gradients and are, in general, of different thickness. The result can be a maximum in the refractive index profile (Fig. 79b) or a more abrupt change from the bulk refractive index compared to the boundary layer with a single solute (Fig. 79a). Qualitatively, interferograms of electrochemical boundary layers are similar to those found in heat transfer and non-electrochemical mass transfer (31,126).

C. Outlook

Recent advances in the quantitative understanding of electrochemical processes require a detailed knowledge of transport properties. To a large extent, interferometry is capable of providing data for use in models of transport processes. Together with the application of established interferometric techniques, the use of a number of instruments not previously considered for such purposes could result in important advances in the design and use of electrochemical devices.

The systematic consideration of light deflection errors, barely initiated at present, should make it possible to produce results of greatly improved reliability. The computational techniques developed for the consideration of light deflection can be adapted for the analysis of some 3-dimensional concentration fields. It is to be hoped that the present limitation of interferometry to one-component electrolytic solutions can be overcome by a combination with other techniques, such as spectroscopic ones.

# IV. INTERFEROMETRY OF ELECTRODE SURFACES

Among optical techniques used for surface finish evaluation (152), double beam interferometry provides some particularly attractive techniques for observing the micro-topography of electrode surfaces (4). Compared to multiple beam interferometry, usually considered for this purpose (133,140), double beam interference microscopes are basically capable of using objectives of higher numerical apertures, because of the absence of a reference mirror between lens and object. Also, they avoid the sampling of an extended region to contribute to the interference phenomenon at one point of the image (82). Thus, smaller surface features can be resolved. Another advantage is that the specimen surface does not have to be coated with a highly reflecting material, (4,80) but can be inspected without alteration. The sinusoidal intensity distribution, typical of double beam interference fringes, is often considered a disadvantage for surface topographic studies (4). It will be shown, however, that this feature can be turned into an advantage by the use of micro-densitometry.

Complete separation of sample and reference beams for the examination of opaque surfaces is realized in a modification of the Michelson interferometer, the Zeiss-Linnik interference microscope (8,43,143), schematically shown in Fig. 80. This instrument employs pairs of matched objective lenses in specimen and reference beams and a replaceable reference mirror, which can be chosen with a reflectivity close to that of the specimen for good fringe contrast. Auxiliary optical elements, not shown in Fig. 80, allow one to control spacing and orientation of interference fringes.

A sample interferogram of an optically polished metal surface is shown in Fig. 81. For the interpretation of such an interferogram, it must be remembered that optical path differences are doubled because

0 0 0 0 3 6 0 5 0 1 3



of the reflection of light from the specimen. An interference fringe shift of one fringe spacing therefore represents a local displacement of the reflecting surface of only half a wavelength of the light employed. Thus, the displacement of interference fringes of approx. 0.08 fringe spacings due to the few prominent scratches seen on Fig. 81, represent a surface deviation of about 200 Å.

The depth of the finer polishing marks is difficult to estimate by visual inspection of the interferogram. However, a micro-densitometer scan of an enlarged transparency along the shoulder of an interference fringe (parallel to its main direction) provides a quantitative analysis of these details (Fig. 82 solid line). The local optical transmission can be correlated with the fringe displacement by a similar scan normal to the direction of the interference fringes (Fig. 82, broken line) and a contour scale can be derived from such a scan based on the linear change in phase between fringes. This scale automatically takes all photographic non-linearities and process variations into account. Since the scale is compressed at both ends, the surface profile scan is preferably chosen in the center part of the transmission range, where variations in surface position of 5 Å seem to be resolvable. This compares with a resolution of 20-30 Å reported for the use of photographically generated equidensity lines (82). In good agreement with the visual estimate, the deepest local surface variation found in Fig. 82 is about 200 Å. This figure is further confirmed by the electron micrograph of a replica of the same surface, shadowed at a small angle (Fig. 83). The more shallow polishing marks, recorded in Fig. 82, are also visible in Fig. 83.

The detailed analysis of interferograms assumes all intensity changes

to be due to interference. It should be asserted separately (e.g. by blocking the reference beam) that other factors affecting local image intensity, such as scattering or absorption in the object, or the effect of imperfections in the instrument, can be neglected. Since the phase of the object wave is measured relative to that of the reference wave in the Zeiss-Linnik interference microscope and many other interference microscopes for reflected light (80), smoothness and flatness of the reference mirror are essential for reliable results. Any effect of the reference mirror on the interferogram could be detected by slightly displacing the object in the field of view. Instrument designs which avoid the use of a reference plane have been discribed by Krug et al. (81).

Polarizing interference microscopes for reflected light (44) usually produce differential interferograms in which the image intensity is a measure of the surface slope in a given direction. This mode of operation produces a relief-like appearance of the object which can be very pleasing to the eye, but is less suited for quantitative evaluation. Other types of interference microscopes for reflected light have been described (38, 80).

Interference microscopy can be expected to find increasing use for the characterization of electrode topographies. New applications dealing with crystallographic and metallurgical factors can be forseen as well as in situ observations of electro-crystallization and dissolution processes.

Acknowledgments

This work was conducted in part under the auspices of the U. S. Atomic Energy Commission. Some of the analyses given in sections Bb, Bd and C have originally been carried out at the Swiss Federal Institute of Technology in collaboration with Prof. N. Ibl.

0 0 0 0 3 6 0 0 0 1 5



## REFERENCES


1. H. J. Antweiler, Z. Elektrochem. 44, 719 (1938).
2. H. J. Antweiler, Kolloid Z. 115, 130 (1949).
3. H. J. Antweiler, Chem. Ing. Technik 24, 284 (1952).
4. K. M. Baird, in Advanced Optical Techniques, A. C. S. Van Heel, ed., North-Holland, Amsterdam; Wiley, New York, 1967, Ch. 4.
5. K. M. Baird and G. R. Hanes, in Applied Optics and Optical Engineering, Vol IV part I, R. Kingslake, ed., Academic Press, New York, 1967, Ch. 9.
6. K. W. Beach, R. H. Muller and C. W. Tobias, Rev. Sci. Instr. 40, 1248 (1969).
7. K. W. Beach, Ph.D. Thesis, Dept. of Chem. Engr., University of California, Berkeley, UCRL-20324 (1971).
8. J. R. Benford and H. E. Rosenberger, in Applied Optics and Optical Engineering, Vol. IV part I, R. Kingslake, ed., Academic Press, New York, 1967, Ch. 2.
9. A. H. Bennett, H. Jupnik, H. Osterberg and O. W. Richards, Phase Microscopy, Wiley, New York, 1951, Ch. II.
10. ibid., Ch. VII.
11. F. D. Bennett and G. D. Kahl, J. Opt. Soc. Am. 43, 71 (1953).
12. M. Born and E. Wolf, Principles of Optics, 2nd ed., MacMillan Co., New York, 1964, Ch. II.
13. ibid., Ch. III.
14. ibid., Ch. VII.
15. ibid., Ch. VIII.
16. ibid., Ch. X.

17. O. Bryngdahl, Acta Chem. Scand 11, 1017 (1957).

18. O. Bryngdahl, in Progress in Optics, Vol. IV, E. Wolf, ed., North Holland Publ. Co., Amsterdam, 1965, Ch. II.

19. C. S. Caldwell, Ph. D. thesis, University of Washington, Department of Chemical Engineering, 1955.

20. E. Calvert and R. Chevalieras, J. de chimie physique 43, 37 (1946).

21. C. Candler, Modern Interferometers, Hilger and Watts, Ltd., 1951, Ch. VI and VII.

22. ibid, Ch. VIII and IX.

23. ibid, Ch. XX.

24. T. W. Chapman, Ph.D. Thesis, Department of Chemical Engineering, University of California, Berkeley, Nov. 1967 (UCRL-17768).

25. A. Chatterjee, J. Am. Chem. Soc. 86, 793 (1964).

26. E. C. Craven, Proc. Phys. Soc. 57, 97 (1945).

27. J. M. Creeth, J. Am. Chem. Soc. 77, 6428 (1955).

28. P. J. Dunhop and L. J. Gosting, J. Am. Chem. Soc. 75, 5073 (1953).

29. H. B. Dwight, Tables of Integrals and other Mathematical Data, MacMillan Co., New York, 1960, 3rd ed. p. 160.

30. J. Dyson, in Concepts of Classical Optics, J. Strong, Freeman, San Francisco, 1958, Appendix B.

31. E. R. G. Eckert and R. M. Drake, Heat and Mass Transfer, McGraw Hill, 1959, Ch. 9,11.

32. ibid, Ch. 11.

33. A. Emanuel and D. R. Olander, J. Chem. Engr. Data 8, 31 (1963).

34. R. Forsberg and H. Svensson, Optica Acta 1, 90 (1954).

35. M. Françon, in Proc. Symposium Interferometry, Natl. Phys. Lab., 1959, H. M. Stationery Office, London 1960, p. 129.

36. M. Françon, Progress in Microscopy, Row, Peterson & Co, Evanston, Ill, 1961, Ch. II.

37. ibid, Ch. III.

38. ibid, Ch. IV.

39. M. Françon, Optical Interferometry, Academic Press, New York, 1966, Ch II.

40. ibid, Ch. III.

41. ibid, Ch. IV.

42. ibid, Ch. VII.

43. ibid, Ch XVI.

44. M. Françon, in Advanced Optical Techniques, A.C.S. Van Heel, ed., North-Holland, Amsterdam, Wiley, New York, 1967, Ch 2.

45. J. J. Fritz and C. R. Fuget, J. Phys. Chem. 62. 303 (1958).

46. R. J. Goldstein, Rev. Sci. Instr. 36, 1408 (1965).

47. P. A. Gooderum, G. P. Wood, and M. J. Brevoort, 36th Ann. Rep. Natl. Adv. Comm. Aeronautics p. 289, U. S. Gov. Print. Office 1951, Report 963.

48. L. J. Gosting, E. M. Hanson, G. Kegeles and M. S. Morris, Rev. Sci. Instr. 20, 209 (1949).

49. L. J. Gosting, J. Am. Chem, Soc., 72, 4418 (1950).

50. L. J. Gosting and L. Onsager, J. Am. Chem. Soc., 74, 6066 (1952).

51. L. J. Gosting, in Advances in Protein Chemistry, Vol XI, M. L. Anson, K. Bailey and J. T. Edsall, eds., Academic Press, New York, 1956, p. 429.

52. A. J. Hale, The Interference Microscope in Biological Research, Livingstone Ltd, Edinburgh, 1958, Ch. II.

53. ibid, Ch III, IV.

54. G. Hansen, Z. Instr. kunde 50, 460 (1930).

55. G. Hansen, Z. Techn. Phys. 12, 436 (1931).

56. G. Hansen, Zeiss Nachr. 3, 302 (1940).

57. G. Hansen, Z. Instr. kunde 60, 325 (1940).

58. P. Hariharan and D. Sen, J. Sci, Instr. 38, 428 (1961).

59. P. Hariharan and D. Sen, Optica Acta 9, 159 (1962).

60. E. v. Heydebrand und der Lasa, Ann. der Physik [5] 37, 589 (1940).

61. C. D. Hodgman, R. C. Weast and S. M. Selby, eds., Handbook of Chemistry and Physics, 38th ed., Chemical Rubber Publ. Co., Cleveland, Ohio, 1956 .

62. L. Hsueh, Ph.D. Thesis, Department of Chemical Engineering, University of California, Berkeley, Dec. 1968 (UCRL 18597).

63. H. Hugenschmidt and K. Vollrath, in Proc. Ninth Intl. Congr. High-Speed Photography, W. G. Hyzer and W. G. Chace, eds., Soc. Motion Picture and Television Engineers, New York, 1970, p. 86.

64. N. Ibl, Y. Barrada and G. Truempler, Helv. Chim. Acta 37, 583 (1954).

65. N. Ibl and R. Muller, Z. Elecktrochem, 59, 671 (1955).

66. N. Ibl, Private communication 1956.

67. N. Ibl, Proc. Seventh Meet. Int. Comm, Electrochem. Thermodynamics and Kinetics, Lindau 1955, Butterworths Publ., London, 1957, p. 112.

68. N. Ibl, Proc. Eighth Meet. Int. Comm. Electrochem. Thermodynamics and Kinetics, Madrid 1956. Butterworths Publ., London 1958, p. 174.

69. E. Ingelstam, E. Djurle and L. Johansson, J. Opt. Soc. Am. 44, 472 (1954).

0 0 0 0 3 6 0 0 0 1 7



70. K. Iwata and R. Nagata, J. Opt. Soc. Am. 60, 133 (1970).

71. F. A. Jenkins and H. E. White, Fundamentals of Optics, McGraw Hill Co, 1957, 3rd ed., Part II.

72. G. D. Kahl and D. B. Sleator, Rev. Sci, Instr. 36, 993 (1965).

73. G. Kegeles and L. J. Gosting, J. Am. Chem. Soc. 69, 2516 (1947).

74. Kern Optical Company, Aarau, Switzerland, Micro-Electrophoresis Apparatus LK 30, Pamphlet.

75. W. Kinder, Optik 1, 413 (1946).

76. R. E. Kinzly, Appl. Optics 6, 137 (1967).

77. R. Kraushaar, J. Opt. Soc. Am. 40, 480 (1950).

78. W. Krug and E. Lau, Phys. Blaetter 15, 11 (1959).

79. W. Krug, J. Rienitz and G. Schulz, Contributions to Interference Microscopy, Hilger and Watts. London, 1964, Ch. 3.

80. ibid, Ch. 4.

81. ibid, Ch. 8.

82. ibid, Ch. 9.

83. H. Kuhn, Rep. Progr. Phys. 14, 64 (1951).

84. H. Labhart and H. Staub, Helv. Chim. Acta 30, 1954 (1947).

85. H. Labhart, W. Lotmar and P. Schmid, Helv. Chim. Acta 34, 2449 (1951).

86. E. Lamla, Z. Instr. kunde 62, 337 (1942).

87. O. Lamm, Z. Phys. Chem. A 138, 313 (1928).

88. E. Lau and W. Krug , Die Aequidensitometrie, Akademie Verlag, Berlin 1957.

89. L. Levi, Applied Optics, Wiley and Sons, New York, 1968, p. 332.

90. C. S. Lin, R. W. Moulton and G. L. Putnam, Ind. Eng. Chem. 45, 640 (1953).

91. A. Lohmann, Optica Acta 9, 1 (1962).

92. L. G. Longsworth, J. Am. Chem. Soc. 69, 2510 (1947).

93. L. G. Longsworth, Rev. Sci, Instr. 21, 524 (1950).

94. L. G. Longsworth, Anal. Chem. 23, 346 (1951).

95. L. G. Longsworth, in Electrophoresis, M. Bier, ed., Academic Press, 1959, Ch. 4.

96. W. Lotmar, Helv. Chim. Acta 32, 1847 (1949).

97. W. Lotmar, Rev. Sci. Instr. 22, 886 (1951).

98. W. Lotmar, Plasma 1, 209 (1953).

99. F. L. McLarnon, Private communication, 1971.

100. H. C. Mel, J. Chem. Phys. 31, 559 (1959).

101. H. E. Merwin, in Int. Crit. Tables, vol 7, E. W. Washburn, C. J. West, N. E. Dorsey and M. D. Ring, eds., McGraw-Hill Book Co, New York, London, 1930, p. 21.

102. W. Nebe, Analytische Interferometrie, Akademische Verlagsges. Leipzig, 1970.

103. M. G. Nomarski, J. de Phys. Radium [8] 16, 9S (1955).

104. H. Oertel, in Proc. 5th Intl. Congress High-Speed Photography, J. S. Courtney-Pratt, ed., Soc. Motion Picture and Televison Engrs. New York, 1962, p. 525.

105. A. K. Oppenheim, P. A. Urtiew and F. J. Weinberg, Proc. Roy, Soc. A 291, 279 (1966).

106. T. P. Pandya and F. J. Weinberg, Proc. Roy. Soc. A279, 544 (1964).

107. J. R. Partington, An Advanced Treatise on Physical Chemistry, vol 4, Physico-Chemical Optics, Longman Green Co, New York, 1953, Sec. XA.

0 0 0 0 3 6 0 0 0 1 8



108. Perkin Elmer Corp., Norwalk, Conn. Instructions, Model 238 Electrophoresis Apparatus, Sept. 1963.

109. J. St. L. Philpot and G. H. Cook, Research Appl. in Industry, 1, 234 (1948).

110. R. H. Pickard, A. H. J. Houssa and H. Hunter, in Int. Crit. Tables, vol 7, E. W. Washburn, C. J. West, N. E. Dorsey and M. D. Ring, eds., McGraw-Hill Book Co, New York, London, 1930, p. 65.

111. A. V. Podalinskii, Russ. J. Phys. Chem. 37, 636 (1963).

112. J. Rienitz, U. Minor and E. Urbach, in Optical Instruments and Techniques, K. J. Habell, ed., Chapman and Hall, London, 1962.

113. H. Roegener, Z. Elektrochem. 47, 164 (1941).

114. H. Roegener, Kolloid Z. 105, 110 (1943).

115. W. A. Roth and K. Scheel, eds. Landolt-Boernstein, Physikalisch-Chemische Tabellen, vol I, Springer Verlag, Berlin, 1923, Table 87m.

116. W. A. Roth and K. Scheel, eds. Landolt-Boernstein, Physikatisch-Chemische Tabellen, vol II, Springer Verlag, Berlin, 1923, tables 174, 179, 185, 186.

117. R. L. Rowe, Instrument Soc. Am. (ISA) Trans. 5, 44 (1966).

118. G. V. Sadovnikov, B. M. Smolskiy and V. K. Shchitnikov, Heat Transfer Solviet Research, 1, 32 (1969).

119. A. G. Samarcev, Z. Phys. Chem. A 168, 45 (1934).

120. M. J. Saunders and A. G. Smith, J. Appl. Phys. 27, 115 (1956).

121. H. Schardin, Z. Instr. kunde 53, 396, 424 (1933).

122. H. Schardin, in Ergebnisse der exakten Naturwissenschaften, vol. 20, F. Hund and F. Trendelenburg, eds., Springer Verlag, Berlin, 1942, p. 303.

123. O. Schoenrock, Z. Instr. kunde. 62, 209, 241 (1942).

124. J. R. Selman, Ph.D. Thesis, Department of Chemical Engineering, University of California, Berkeley, June 1971 (UCRL 20557), also: S. K. Arapskoske and J. R. Selman, UCRL 20510 (March 1971).

125. K. Shaftan and D. Hawley, Photographic Instrumentation, Soc. Phot. Instrumentation Engrs., Washington D.C. 1962, p. 19, 98.

126. H. A. Simon and E. R. G. Eckert, Int. J. Heat Mass Transfer 6, 681 (1963).

127. E. M. Slayter, Optical Methods in Biology, Wiley-Interscience, 1970, Ch. 13.

128. ibid, Ch. 14.

129. W. H. Steel, in Progress in Optics, vol V, E. Wolf, ed., North Holland Publ., 1966, Ch. III.

130. W. H. Steel, Interferometry, Cambridge University Press, 1967, Ch. 1.

131. ibid, Ch. 4 and 5.

132. ibid, Ch. 6.

133. ibid, Ch. 9.

134. H. Svensson, Acta Chem. Scand. 3, 1170 (1949).

135. H. Svensson, Acta Chem. Scand. 4, 1329 (1950), 7, 159 (1953).

136. H. Svensson, Acta Chem. Scand. 5, 72 (1951).

137. H. Svensson, Acta Chem. Scand. 5, 1301 (1951).

138. H. Svensson, Optica Acta 1, 25 (1954).

139. W. J. Thomas and E. McK. Nicholl, Appl. Optics 4, 823 (1965).

140. S. Tolansky, Surface Microtopography, Interscience, New York, 1960.

141. S. Tolanski, An Introduction to Interferometry, Wiley and Sons, New York, 1962, 3rd ed. Ch. 5.

142. ibid, Ch. 8.

143. ibid, Ch. 9.

144. A. Tvarusko and L. S. Watkins, Electrochim . Acta 14, 1109 (1969).

145. A. Tvarusko and L. S. Watkins, J. Electrochem Soc. 118, 248 (1971).

146. F. Twyman, Prism and Lens Making, Hilger and Watts, London, 1952, 2nd ed. Ch. 12.

147. A. C. S. Van Heel, in Concepts of Classical Optics, J. Strong, Freeman and Co, San Francisco, 1958, Appendix D.

148. F. J. Weinberg, Optics of Flames, Butterworths, London, 1963, Ch. 1.

149. ibid, Ch. 2.

150. ibid, Ch. 4.

151. ibid, Ch. 8.

152. H. von Weingraber, in Proc. Intl. Production Engr. Res. Conf., Carnegie Inst. Tech., Sept. 1963, M. C. Shaw, ed., Am. Soc, Mech. Engrs., New York, 1963, p. 659.

153. W. Weinstein, Nature 172, 461 (1953).

154. W. E. Williams, Applications of Interferometry, Methuen, London; Wiley, New York, 1950, p. 10

155. J. Winckler, Rev Sci Instr. 19, 307 (1948).

156. E. H. Winkler, Naval Ordnance Laboratory Report, NOLR 1077.

157. H. Wolter, in Encylopedia of Physics, vol 24, S. Fluegge, ed., Springer Verlag, Berlin , 1956, p. 589.

158. F. Zernike, Physica 9, 686, 974 (1942).

FIGURE CAPTIONS

Fig. 1. Principle of double beam interferometry

A - Variable refractive index in specimen cell

B - Specimen cell with different parts of a plane light wave which enter the cell in phase and get increasingly out of phase during propagation through it

C - Uniform refractive index in reference cell

D - Reference cell with different parts of a plane wave which stay in phase during propagation

E - Interference pattern due to the superposition of specimen and reference waves. Local optical path difference in wavelengths.

Fig. 2. Concentration-dependence of the refractive index of aqueous copper sulfate solutions at 20°C (116).

Fig. 3. Concentration-dependence of the refractive index of sulfuric acid (116).

Fig. 4. Refractive index of mixtures of sulfuric acid and copper sulfate (124).

Fig. 5. Refractive indices at different wavelengths, literature data $H_2SO_4$, 99.5%, 23°C (116), $CuSO_4 \cdot 5H_2O$ (101), $H_2O$ (116).

Fig. 6. Determination of the concentration of two separate components of a solution from the refractive index at two different wavelengths (schematic).

Fig. 7. Temperature dependence of refractive index $H_2SO_4$, 95-96% (110), 1 M KCl(116), 1 M $CuSO_4$ (116), $H_2O$ (61).

Fig. 8. Production of two coherent light beams. (a) Division of wave-front by a double slit (b) Division of amplitude by partial reflection.

0 0 0 0 3 6 0 3 0 1 9



Fig. 9. Rayleigh interference refractometers.

A - point source

B,G - spherical lenses

C,F - double slits

D - specimen and reference chambers

E - compensator

H - plane of interference fringe formation

I - eyepiece.

Fig. 10. Rayleigh interferometer for the observation of vertical refractive variations, plan view diagram.

A - point or slit source

B - spherical lens

C - double slit

D - specimen and reference cells (refractive index variations in vertical direction)

E - spherical lens for imaging slit A (with interference fringes)in horizontal direction

F - cylindrical lens with horizontal axis for imaging cell D in vertical direction

G - film plane

H - fringe pattern in film plane for a diffuse liquid junction.

Fig. 11. Rayleigh interferograms, observation of the diffusion of a 0.2% solution of sucrose against water (Svensson 134).

Left: refractive index profile (normal interferogram)

Right: refractive index derivative profile, obtained with two identical diffusion boundaries, slightly shifted with respect to each other

Fig. 12. Multiple source Rayleigh interferometer with double pass through the specimen (Perkin-Elmer 108, Chapman 24).

A - monochromatic lamp

B - multipoint source

C - narrow mirror above reflected beams D, G

D - spherical lens

E - specimen and reference cells

F - plane mirror

G - spherical lens for imaging cell in vertical direction

H - cylindrical lens with vertical axis for imaging interference fringes in horizontal direction (with lens G)

I - photographic plate

Fig. 13. Multiple source Rayleigh interferogram. Diffusion of 1.081 vs. 1.180 M $CuSO_4$, 1.5 hrs after forming boundary (Hsueh 62).

Fig. 14. Jamin interferometer arranged for the observation of horizontal refractive index variations, plan view diagram (Ibl, Barrada and Truempler 64 ).

A - mercury arc lamp with filter for 546.1nm line

B - condenser

C - vertical slit

D - beam splitting Jamin plate

E - object and reference cells

F - beam uniting Jamin plate (tilted around horizontal axis for producing horizontal interference fringes)

G - diaphragm for selection of reflected beams

0 0 0 0 3 6 0 0 0 2 0



H - spherical lens for imaging fringes from infinity in vertical direction

I - cylindrical lens with vertical axis for imaging object in horizontal direction

J - image plane

Fig. 15. Jamin interferogram of cathodic mass transfer boundary layer in 0.6M $CuSO_4$ obtained with the interferometer described in Fig. 14. Scale 1mm, shadow of electrode on the right. (Ibl and Muller 65).

a. before electrolysis

b. current density 2.2mA/$cm^2$, natural convection, vertical cathode.

Fig. 16. Lotmar interferometer (97).

A - monochromatic light source

B - collimator lens

C - Jamin plate

D - cell and reference mirror

E - field lens

F - objective lens

G - image plane

Fig. 17. Lotmar interferograms of the diffusion of two cadmium sulfate solutions (9% vs. 19%) observed with increasing time (97).

Fig. 18. Jamin interference contrast pictures of the anomalous convection on a mercury drop electrode (Antweiler 1).

1. Undisturbed diffusion layer during the reduction of a 0.02 N $FeCl_3$ solution.

2-4. Downward convection in the above solution, at lower potential.

5. Undisturbed diffusion layer during the reduction of a 0.02N

$NiCl_2$ solution.

6. Bell-shaped upward convection in the above solution, at lower potential.

7-8. Eddy convection during the reduction of a 0.1 N $NiCl_2$ solution.

Fig. 19. Sirks-Pringsheim interferometer.

A,E - wedge-shaped glass plates

B - object and reference

C,D - virtual origin of interference fringes

F - objective lens

G - image plane

Fig. 20. Dyson interference microscope.

A - condenser

B - wedge-shape beam splitting plate with partially reflecting right face and totally reflecting center on left face

C - object with surrounding reference

D - wedge-shape beam uniting plate with partially reflecting faces

E - portion of glass sphere with central opening on totally reflecting surface, where image of object is formed

F - microscope objective

G - image plane

H - eyepiece

0 0 0 0 3 6 0 0 3 2 1



Fig. 21. Intensities of beams reflected from a Jamin plate with opaque reflecting coating on back side (95% reflectivity) and different front surfaces:

(a) bare (4% reflectivity)

(b) uniform (loss-free) coating of 37.3% reflectivity

(c) partial coating of 47.7% reflectivity.

Fig. 22. Light intensities in a Jamin interferometer obtainable with differently coated plates. Cases a, b and c as in Fig. 21.

Fig. 23. Classical form of Mach-Zehnder interferometer.

A - source

B - pinhole

C - color filters

D - collimating lens

E - beam splitting plate

F - reference cell

G, H - deflection mirrors

I - specimen cell

J - beam uniter plate

K - objective lens

L - image plane

Fig. 24. Localization and orientation of interference fringes in the Mach-Zehnder interferometer. $W_1$, $W_2$ coherent wave fronts in specimen and reference beams respectively. $W_1'$, $W_2'$ virtual location of $W_1$ and $W_2$ as imaged by the objective lens K on film plane L.

Fig. 25. Modified form of Mach-Zehnder interferometer with laser light source (Beach, Muller and Tobias 6).

A,C,D - first surface deflection mirrors

B - HeNe gas laser with dual beam output

E - specimen cell

F - objective lens

G - beam uniter plate with dielectric coating

H - reference lens

I - spatial filter (slit)

J - image plane

Fig. 26. Boundary layer development observed with interferometer of Fig. 25. Cathode, 4 cm from leading edge, 66 mA/cm$^2$, 0.1M $CuSO_4$, Re = 1100. Before electrolysis, 2 and 20 seconds after start of electrolysis.

Fig. 27. Leitz-Horn interference microscope.

A - beam splitting prism assembly

B - condensers

C - object and reference

D - matched objectives

E - beam uniting prism assembly

F - eyepiece

Fig. 28. Michelson interferometer.

A - collimated light source

B - beam spliting and uniting plate

C,F - object and reference cells

D,E - object and reference mirrors

D' - virtual position of mirror D

G - compensating plate

H - objective lens

I - image plane

0 0 0 0 3 6 0 0 0 2 2



Fig. 29. Beam splitting devices for polarizing interferometers. Ordinary (O) and extraordinary (E) rays with polarization indicated by direction of electric vector. (a) Savart plate, producing linear shear (b) Wollaston prism, producing angular shear.

Fig. 30. Shearing interferometry. Superposition of a specimen wavefront. (—) with another form of it, serving as reference (----)

(a) complete lateral shear

(b) differential lateral shear

(c) angular shear

(d) radial shear

(e) longitudinal shear

Fig. 31. Lebedev interference microscope.

A - polarizer

B - condenser

C,F - birefringent crystal plates

D - half wave plate

E - object and reference

G - objective lens

H - analyzer

I - image plane

J - eyepiece

Fig. 32. Smith interference microscope.

A - light source

B - condenser

C,I - polarizer

D,H - Wollaston prisms

E,G - objective lenses

F - object

J - eyepiece

K - image plane

Fig. 33. Gouy interferometer (side view).

A - illuminator

B - horizontal slit

C - collimating lens

D - cell (with refractive index profile)

E - objective lens

F - image plane

G - undeflected slit image

H - deflected slit image

Fig. 34. Beam splitting by diffraction gratings. Diffraction orders indicated by Roman numerals. (a) parallel beam, (b) convergent beam.

Fig. 35. Four diffraction grating interferometer (Weinberg 151 ).

A - monochromatic light source with condenser

B - pinhole

C - collimating lens

D,I - diffraction gratings operating in plus and minus first order

0 0 0 0 3 6 0 0 0 2 3



E,F - diffraction gratings operating in second order

G - object

H - virtual location of object

J - objective lens

K - image plane

Fig. 36. Zernike phase contrast microscope .

A - diaphragm with annular opening

B - condenser lens

C - object

D - objective lens

E - annular phase plate in rear focal plane of objective

F - image plane

Fig. 37. Interpretation of an interferogram with finite fringe spacing

(a) instrumentally generated interference fringes with local phase given in wavelengths

(b) displaced fringes due to a refractive index field

Fig. 38. Two-dimensional interferogram with finite fringe spacing. Heated horizontal tube in air under natural convection (Hansen 56).

Fig. 39. Interpretation of an interferogram with infinite fringe spacing

(a) uniform object

(b) concentration field like the one used in Fig. 37b.

Fig. 40. Two-dimensional interferogram with infinite fringe spacing, heated horizontal tube in air under natural convection. (Eckert and Drake (32), used with permission of McGraw-Hill Book Company).

Fig. 41. Refractive index increment $\Delta n$, and corresponding concentration increment of a 0.5M $CuSO_4$ solution (n = 1.3468), necessary to shift interfence fringes by one fringe spacing ($\Delta p = \lambda$) in a cell of thickness d. (Eq. 12) Single pass interferometer, green Hg light (546.1 nm). Practical resolution limits of interferometry are 0.1 to 0.001 times the values indicated.

Fig. 42. Tilting of a wave front W due to different propagation rates in a refractive index field.

Fig. 43. Light deflection in uniform refractive index gradient field. Definition of coordinates.

Fig. 44. Light deflection due to a constant refractive index gradient. Angular light deflection $\alpha$ and lateral beam displacement a. Refraction at cell exit results in deflection angle $\beta$.

Fig. 45. Angular light deflection $\beta$ and $\alpha$ due to constant refractive index gradient with and without consideration of refraction at the cell exit, respectively (Eqs. 31 and 29). Cell thickness x = 0.2, 0.5, 1 and 2 cm. Concentration gradient associated with refractive index gradient valid for 0.5M $CuSO_4$ (n = 1.3468, $\partial n/\partial c = 0.027/M$). Current densities indicated result in the associated concentration gradient at the surface of a cathode in 0.5M $CuSO_4$ in the absence of convection.

Fig. 46. Lateral beam displacement at the cell exit due to a constant refractive index gradient (Eq. 33). Cell thicknesses x = 0.2, 0.5, 1 and 2 cm. Refraction inside cell wall not considered. Concentration gradient and current density scales as in Fig. 45.

0 0 0 0 3 6 0 5 0 2 4



Fig. 47. Optical path length errors due to light deflection near a working electrode. a) refractive index profile, b) cross-section of electrolysis cell.

Deflected beam 2 and undeflected reference beams 1 and 3 which enter and leave, respectively, the refractive index field with the deflected beam.

$p_1$, $p_2$, $p_3$ - optical path lengths of the three beams inside the cell

A,D - cell walls

B - electrolyte

C - electrode

Fig. 48. Errors in optical path length due to light deflection in constant refractive index gradient for cell thickness x of 0.2, 0.5, 1 and 2 cm. Wavelength 546.1 nm, refractive index n = 1.3468 (0.5M $CuSO_4$), effects of cell wall and focusing not considered. Concentration gradient and current density scales as in Fig. 45.

Fig. 49. Effect of choice of focal plane on geometrical distortion due to light deflection. a) exit side of cell focused b) optimum focus c) entrance side of cell focused (refraction at cell-air interface and in cell wall not shown).

A - electrolyte

B - electrode

C - deflected beam

D,K,L - virtual locations of electrode surface

E - auxiliary ray

F,F' - focal points of objective lens

G - objective lens

H - image of electrode surface

I - image plane

J - picture of electrode shadow

Fig. 50. Focusing in the absence of light deflection. E-real, immersed object, E'-virtual location of E, F-real plane of focus in cell, F'-virtual plane of focus (focus in air).

Fig. 51. Focusing in the presence of light deflection. ABC-deflected light beam, F-real plane of focus, F'-virtual plane of focus, e-location of plane of focus, g-lateral displacement of virtual beam origin.

Fig. 52. Effect of cell wall thickness d on lateral beam displacement g.

Fig. 53. Lateral displacement g of virtual beam origin due to focusing in a medium of constant refractive index gradient k. Independent of cell wall thickness. Cell thickness x = 1 cm.

Fig. 54. Determination of the location $e_o$ of the plane of focus (inside cell) for which the virtual origin $E_o'$ of a deflected light beam (e.g. electrode shadow) is not displaced laterally.

Fig. 55. Location $e_o$ of plane of focus for zero displacement of electrode shadow due to light deflection in a constant refractive index gradient. Independent of cell wall thickness. Cell thickness x = 0.2, 0.5, 1 and 2 cm.

Fig. 56. Determination of the optical path error due to light deflection. Plane of focus at entrance of light into a medium of variable refractive index.

U U U U U U U U U 2 5



AB - optical path length $p_2$

AC - optical path length $p_4$

EI - optical path length $p_5$

Fig. 57. Effect of cell wall thickness d on error in optical path length.

Fig. 58. Error in optical path length $(p_4 - p_5)/\lambda$ due to light deflection in a refractive index field of constant gradient k. Plane of focus on side of cell at which light enters the liquid medium (e = o). Cell thickness x = 0.2, 0.5 and 1 cm, $n_o$ = 0.3468, $\lambda = 5.461 \times 10^{-5}$ cm, curves 1, 2 - cell wall thickness d = 0 and 1 cm, respectively, cell wall refractive index $n_g$ = 1.51.

Fig. 59. Models of mass transfer boundary layers for light deflection a) constant concentration gradient, b) Nernst model c) realistic concentration profile.

Fig. 60. Light deflection at the edge of a Nernst-type boundary layer.

$p_7$ - optical path length of deflected curved beam AB inside boundary layer

$p_8$ - optical path length of deflected straight beam BC outside boundary layer

$p_9 = p_7 + p_8$

$p_{10}$ - optical path length in bulk refractive index

Fig. 61. Near the edge of a Nernst-type boundary layer two deflected (1, 2) and one undeflected (3) beam exit at every point C

Fig. 62. Computed interference fringe B for a Nernst-type boundary layer of refractive index profile A (Eq. 52). Focus on cell exit, effect of cell wall thickness neglected. C-location of electrode surface, D-image of electrode surface. Bulk refractive index $n_b = 1.3468$, refractive index gradient $k = 0.33 cm^{-1}$, cell width $\ell = 0.5$ cm, wavelength $\lambda = 5.461 \times 10^{-5}$ cm. (Beach 7, McLarnon 99).

Fig. 63. Numerical computation of a deflected light beam GL in a boundary layer. A,D - cell walls, B - electrolyte, C - electrode, P - equiphase circle centered in virtual beam origin E'.

Fig. 64. Interference fringes (b) to (e) computed for refractive index

profiel (a) for different choices of the plane of focus (inside cell). Cell width 1 cm, glass wall thickness 1.27 cm current density 4.5 mA/cm$^2$, wavelength 5.461x10$^{-5}$ cm (Beach 7).

b - focus 3.4 mm inside glass wall farthest from the camera

b - focus on inside face of glass wall farthest from the camera

d - focus inside cell, 3.75 mm from the inside face of the glass wall farthest from the camera

e - focus inside cell, 7.5 mm as above

Fig. 65. Effect of the change of focal plane (inside cell) on the appearance of interference fringes for a cathodic deposition boundary layer (Beach 7)

a. interferogram with the focal plane inside the glass wall farthest from the camera

b. interferogram with the focal plane on inside face of the glass wall farthest from the camera

c. interferogram with the focal plane approximately half way across the cell.

d. Interferogram with the focal plane near the inside of the glass wall near the camera

E. incoming collimated light

F. glass wall farthest from the camera

G. electrolyte and electrode

H. glass wall near the camera

J. camera lens

current density = 5.0 ma/cm$^2$; cell width 1.9 cm; glass width = 1.27 cm. The zero of the vertical scale defines the electrode shadow before the boundary layer was formed.

Fig. 66. Concentration profiles of boundary layers models employed for computations in Figs. 67-70 (McLarnon 99).

Fig. 67. Error in apparent interfacial concentration due to light deflection in a boundary layer model for convective diffusion (Fig. 66). Cell thickness 0.2 and 1 cm, wall thicknesses as indicated below. Boundary layer thickness 0.4 mm, bulk concentration 0.5 M $CuSO_4$, focusing on immersed target on inside surface of cell wall where light enters (McLarnon 99).

| curve | cell thickness x, cm | wall thickness d, cm |
|---|---|---|
| □ | 0.2 | 0.2 |
| ▲ | 0.2 | 0.5 |
| △ | 1.0 | 0.2 |
| ● | 1.0 | 0.5 |
| ○ | 1.0 | 1.0 |

Fig. 68. Error in apparent interfacial concentration grandient due to light deflection in a boundary layer. Other data as in Fig. 67 (McLarnon 99).

Fig. 69. Error in apparent boundary layer thickness due to light deflection. Other data as in Fig. 67. (McLarnon 99).

Fig. 70. Location $e_o$ of plane of focus in cell for zero displacement of electrode shadow due to light deflection in a boundary layer. Other data as in Fig. 67 (McLarnon 99).

Fig. 71. Light deflection in anodic boundary layer a) refractive index profile, b) undeflected beam in the bulk and deflected beam which leaves cell at the electrode surface, c) reflection of deflected beams at the electrode surface.

Fig. 72. Amplitude and phase in a diffraction image 9.2 mm behind a straight edge located at abszissa zero. Wavelength 546.1 nm.

Fig. 73. Diffraction effects in an interferogram near an electrode surface.

Fig. 74. Position of diffraction maxima (solid lines) and minima (broken lines) as a function of distance (defocusing) behind a straight edge. Wavelength 546.1 nm, numbering of maxima and minima as on Fig. 72.

Fig. 75. Electrophoretic separation of normal human serum, descending branch after 37 minutes at 8.5 V $cm^{-1}$. Bottom: Interferogram, top: evaluation (Kern 74)

Fig. 76. Boundary layer thickness (defined as distance from the electrode at which concentration reduction is 10% of that at the interface) on a 3 cm high vertical cathode, observed 1 and 2 cm from the bottom, under natural convection. 0.6 M $CuSO_4$ (Ibl 68).

Fig. 77. Interfacial concentration reduction at a vertical cathode at distance x from the bottom, under natural convection. 0.6M $CuSO_4$, 1 $mA/cm^2$. (Ibl 68).

Fig. 78. Comparison of an interferometrically measured concentration profile (x) with a theoretical one (——) 0.1 M $CuSO_4$, 0.32 $mA/cm^2$ (Ibl 68).

Fig. 79. Boundary layers in stagnant electrolytes at constant voltage, observed with a Rayleigh interferometer. (Hsueh 62)

a) 0.0385 M $CuSO_4$, initial current density 0.244 $mA/cm^2$, times:40, 103, 263 and 475 min.

b) 0.1 M $CuSO_4$ + 1 M $H_2SO_4$, times:9, 40, 106 and 450 min.

Fig. 80. Zeiss-Linnik interference microscope

A - Illuminating system

B - beam splitter

C,F - matched objective lenses

D - Reference mirror

E - object

G - image plane

H - eyepiece

Fig. 81. Interferogram of an optically polished surface of type 316 stainless steel. Wavelength 535.0 nm, Zeiss-Linnik interference microscope. Objective 60×, N.A. 0.63.

Fig. 82. Microdensitometry of interference micrograph shown in Fig. 81. Solid line: scan parallel to interference fringe, resulting in surface profile. Broken line: scan normal to interference fringes, resulting in (non-linear) surface profile scale shown on the right.

Fig. 83. Electron micrograph of a replica of the surface shown in Figs. 81 and 82. Diameter of latex spheres 0.53 micron. Depth of deepest scratches 200 Å.

0 0 0 0 3 6 0 0 0 2 6



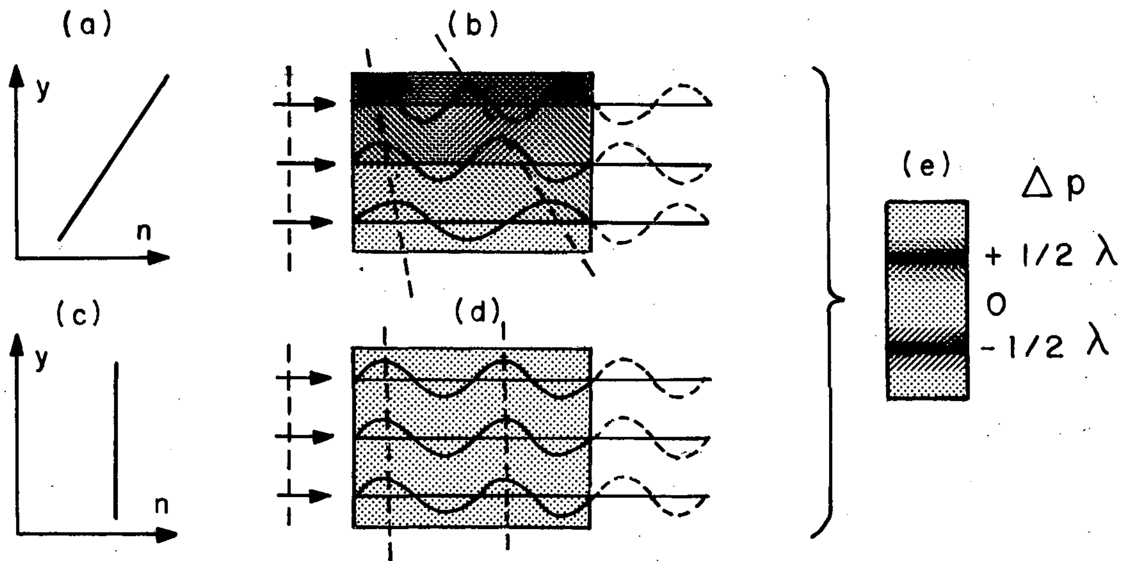


Fig. 1

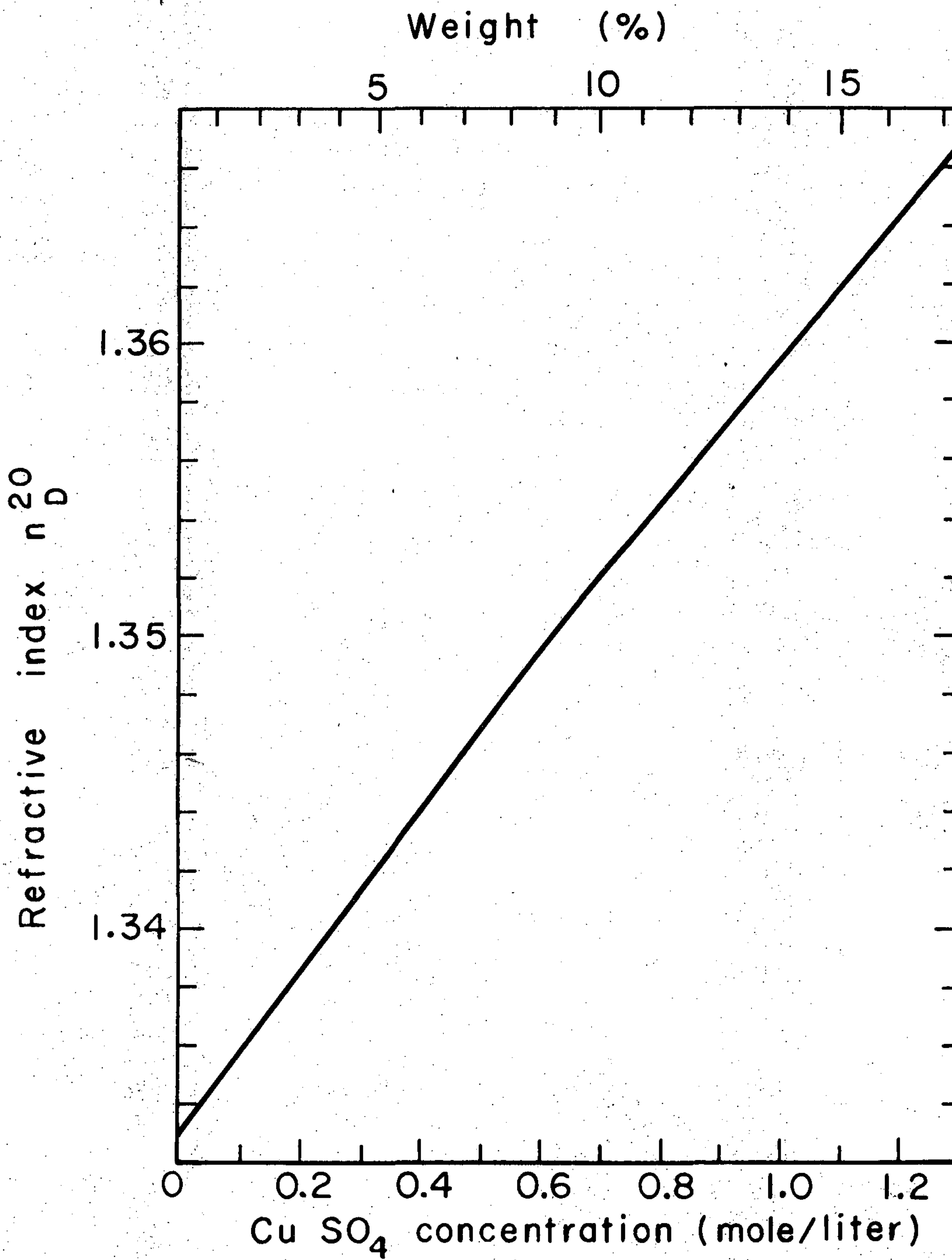


Fig. 2

0 0 0 0 3 6 0 0 0 2 7



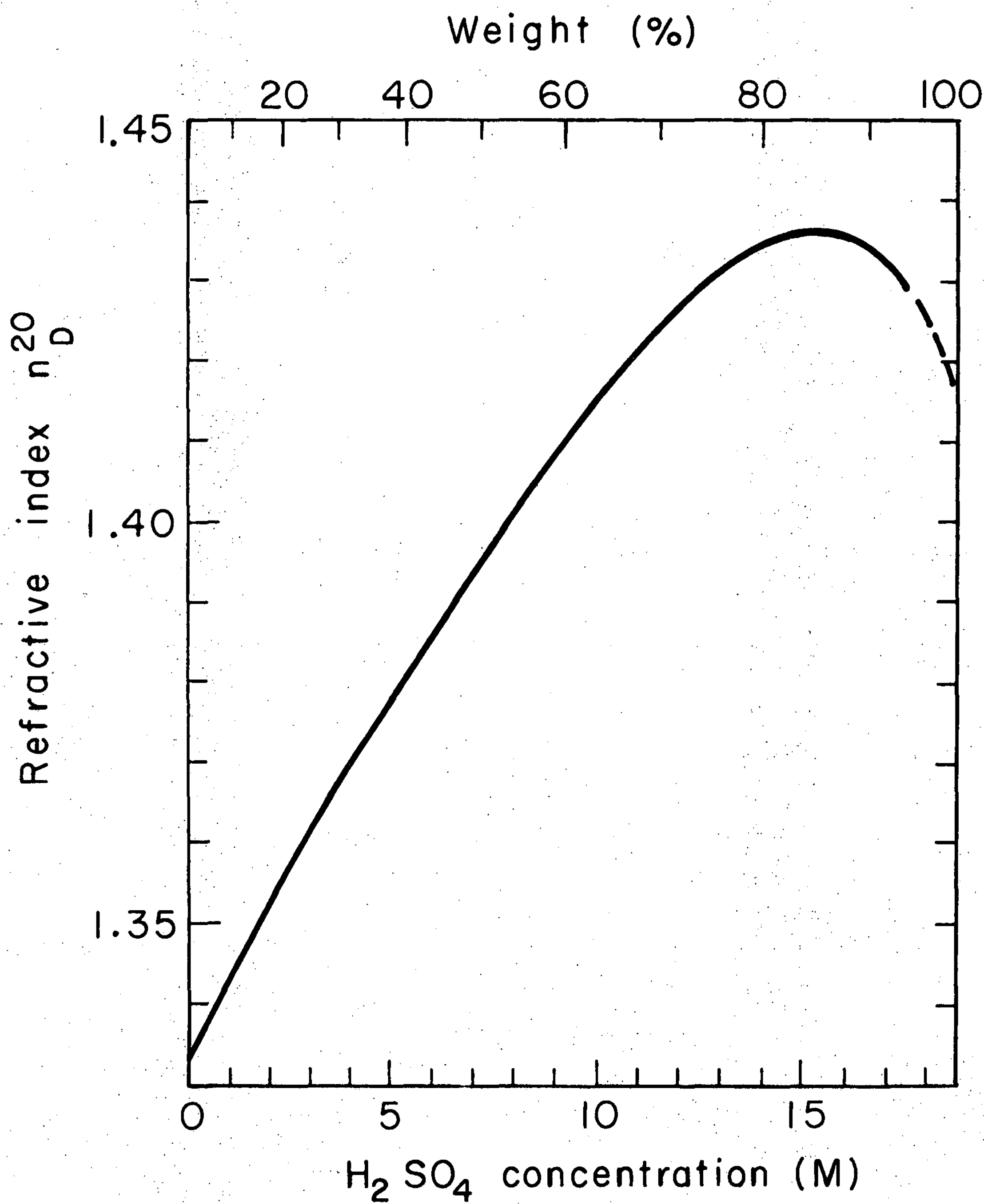


Fig. 3

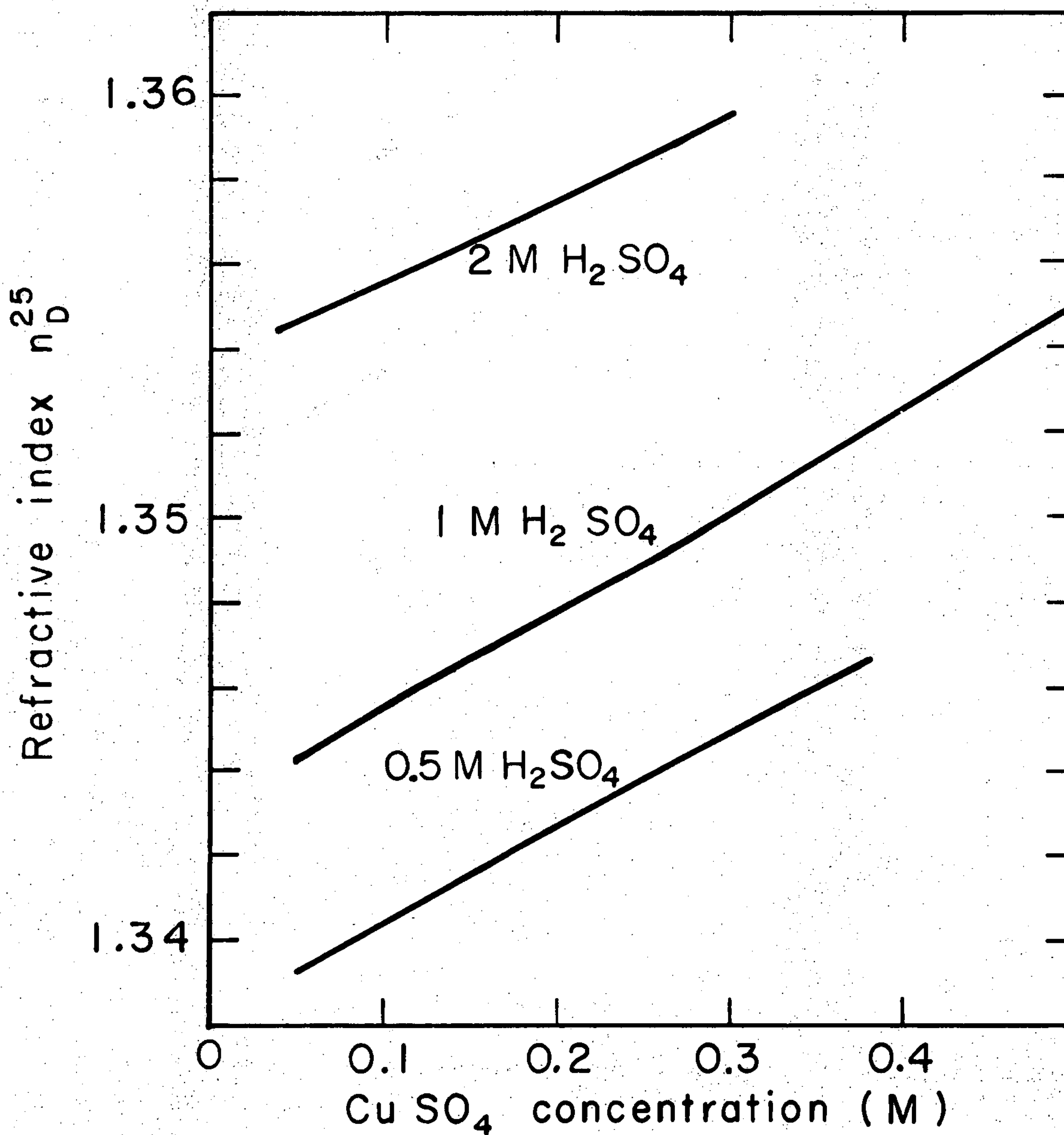


Fig. 4

0 0 0 0 3 6 0 0 0 2 8



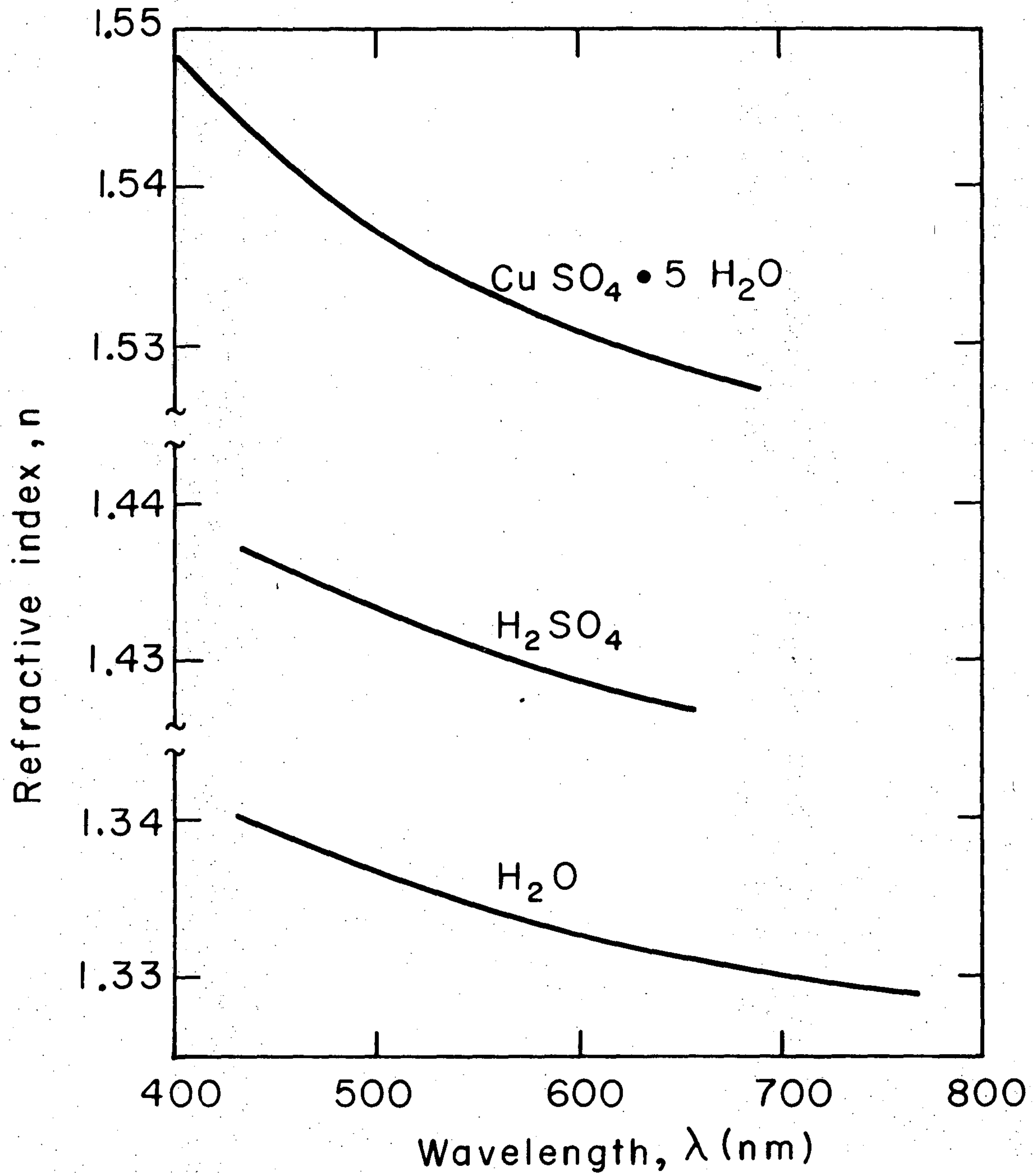


Fig. 5

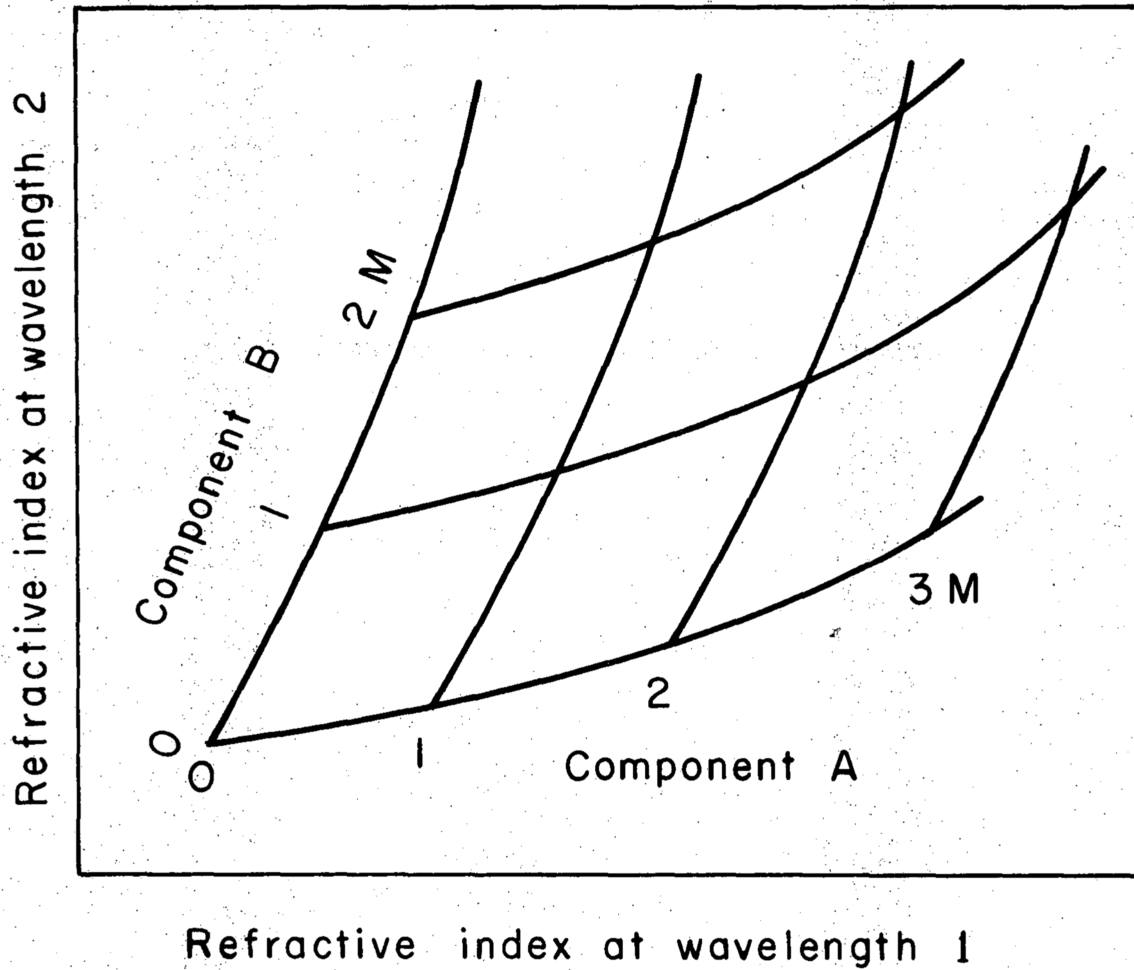


XBL714-3288

Fig. 6

0 0 0 0 3 6 0 0 0 3 3



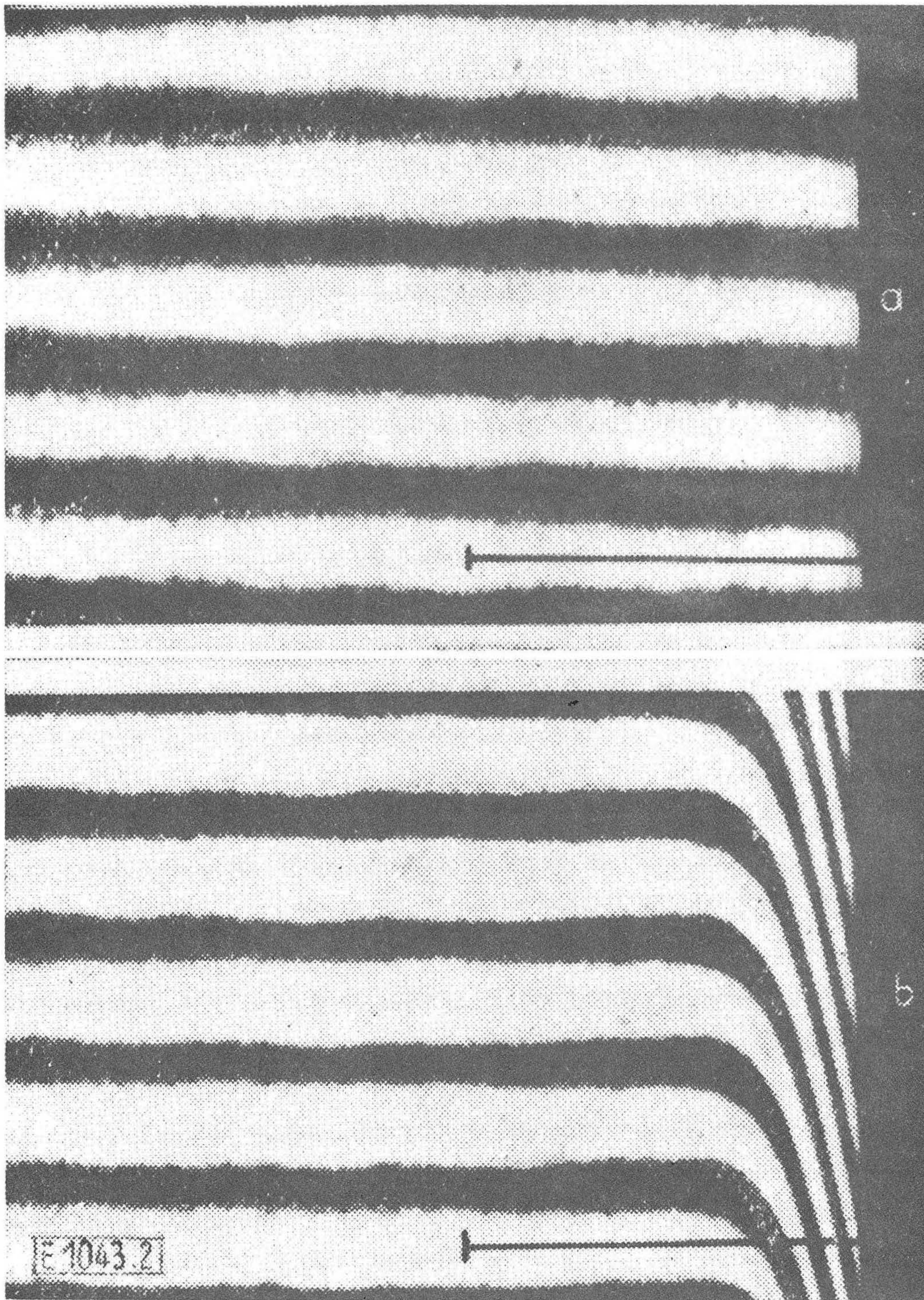


IM 1584

Fig. 15

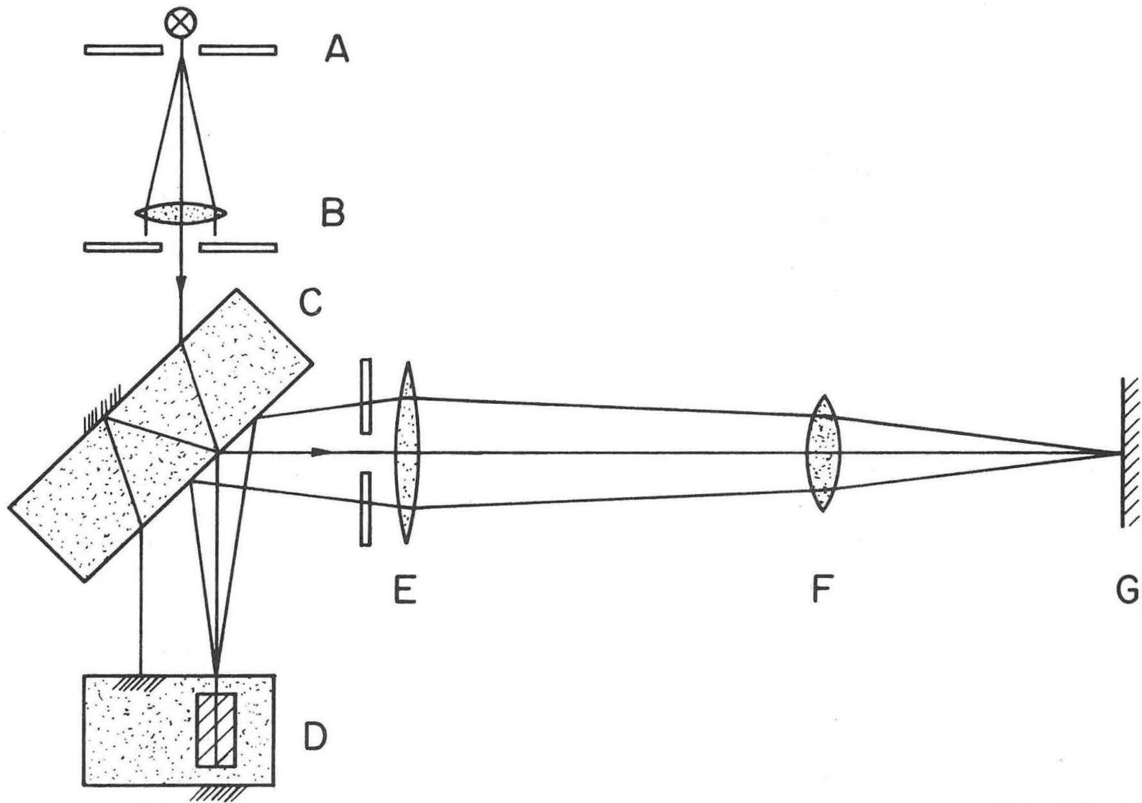


Fig. 16

0 0 0 0 3 6 0 0 0 3 4



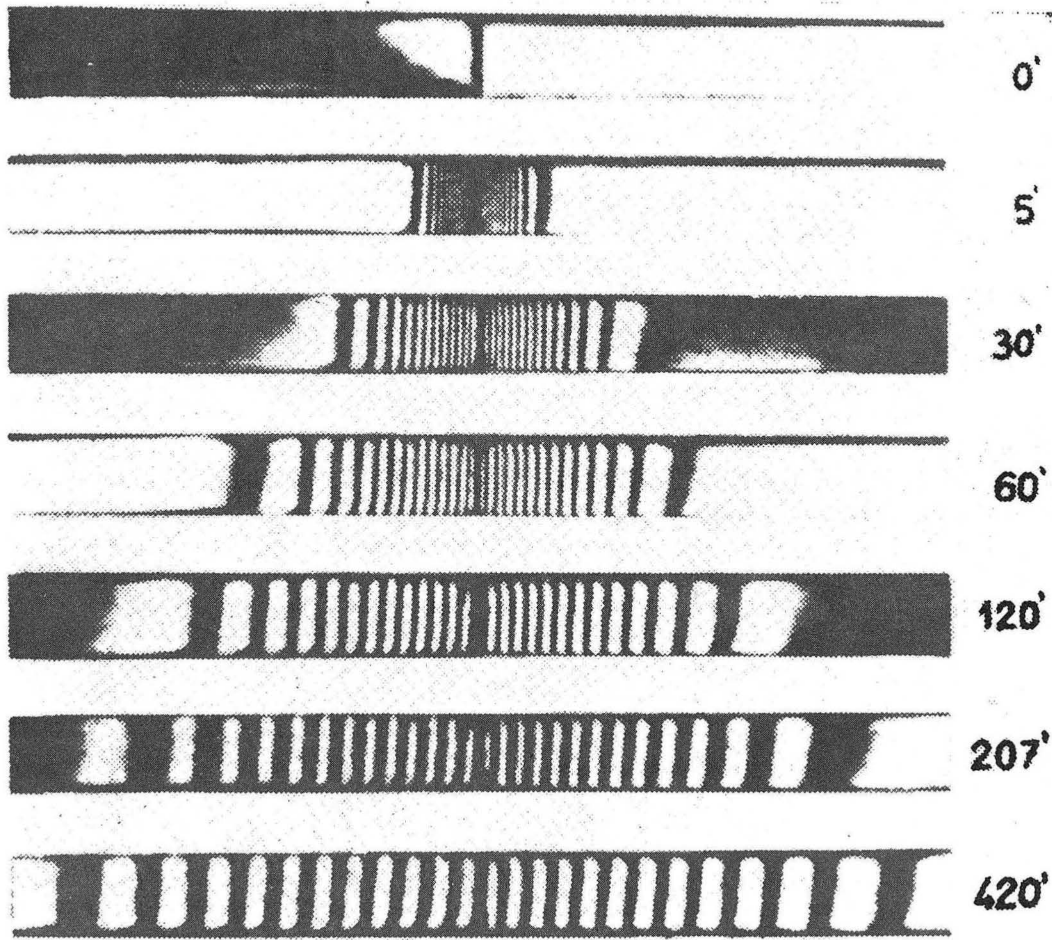


IM 1583

Fig. 17

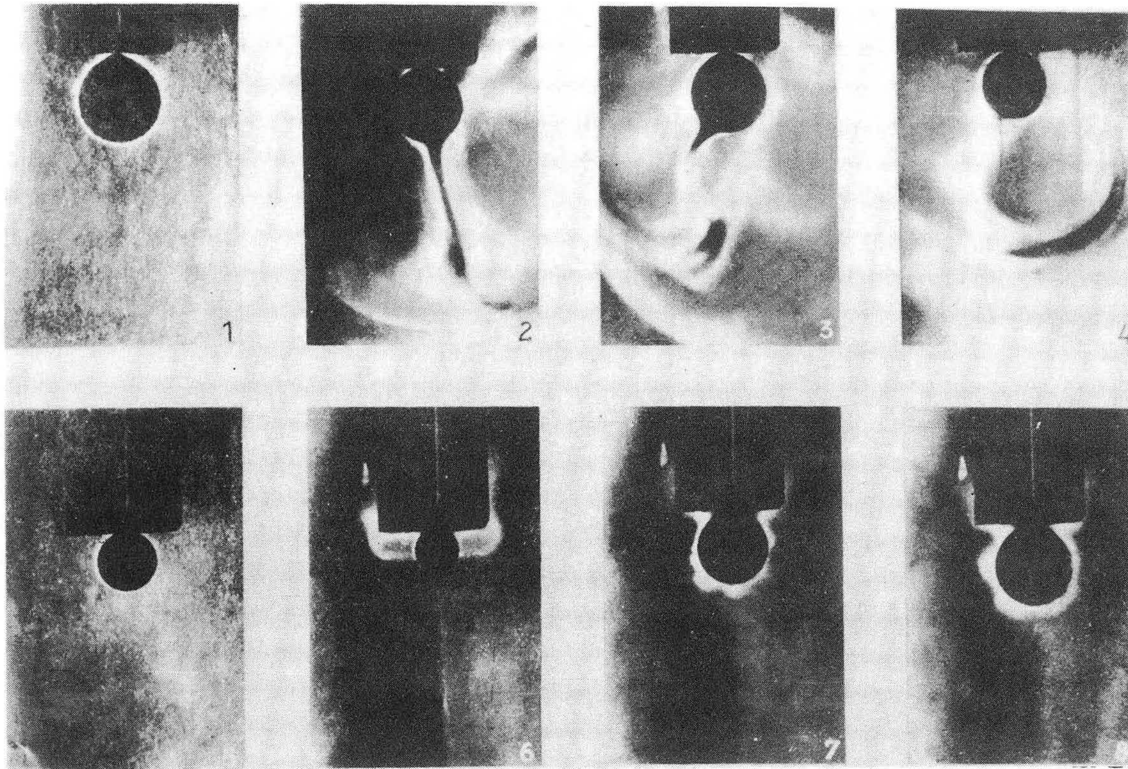


IM 1587

Fig. 18

0 0 0 0 3 6 0 0 0 3 5



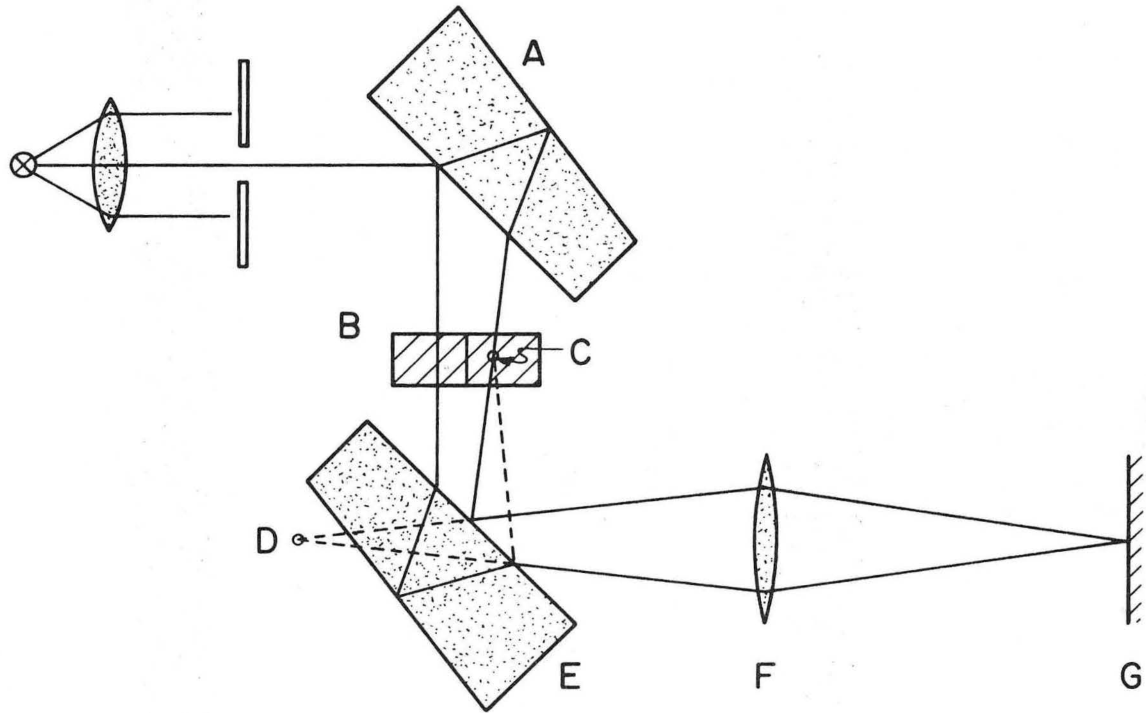


Fig. 19

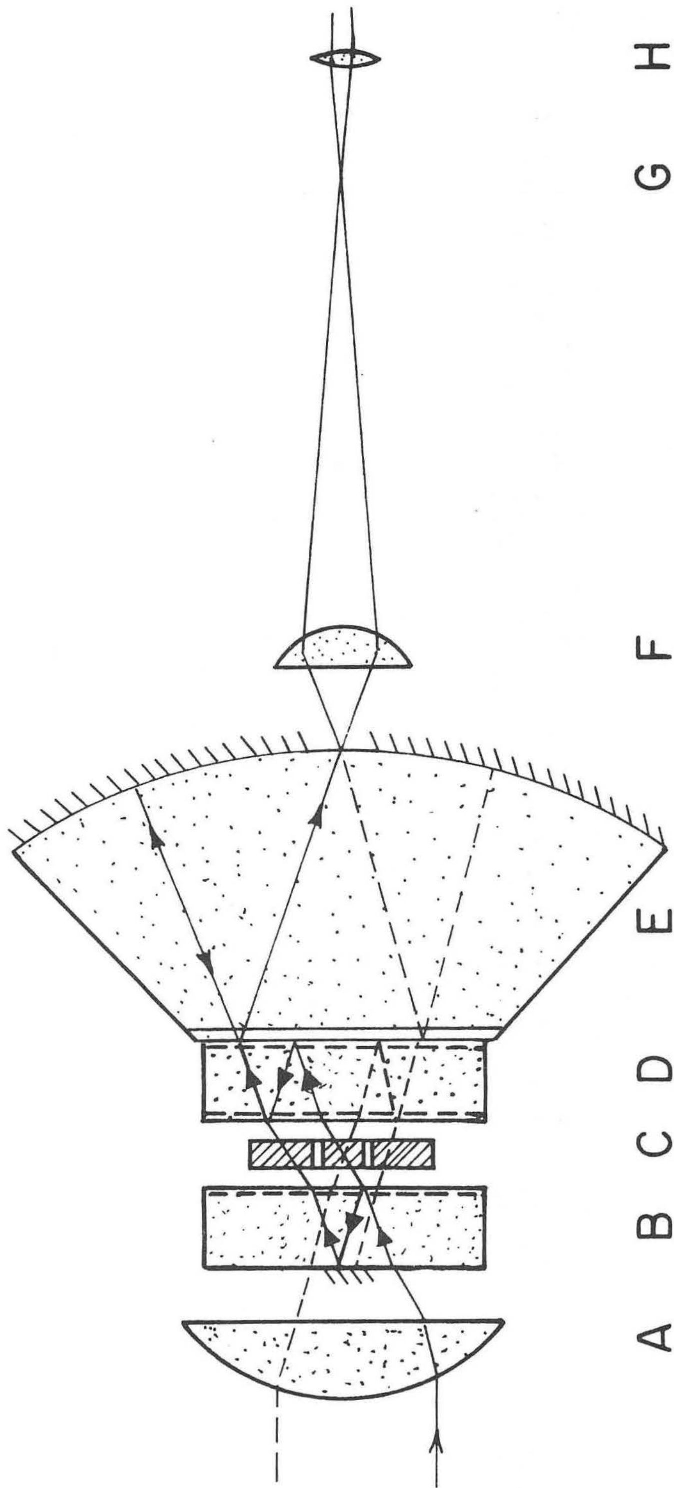


Fig. 20

0 0 0 0 3 6 0 5 0 3 6



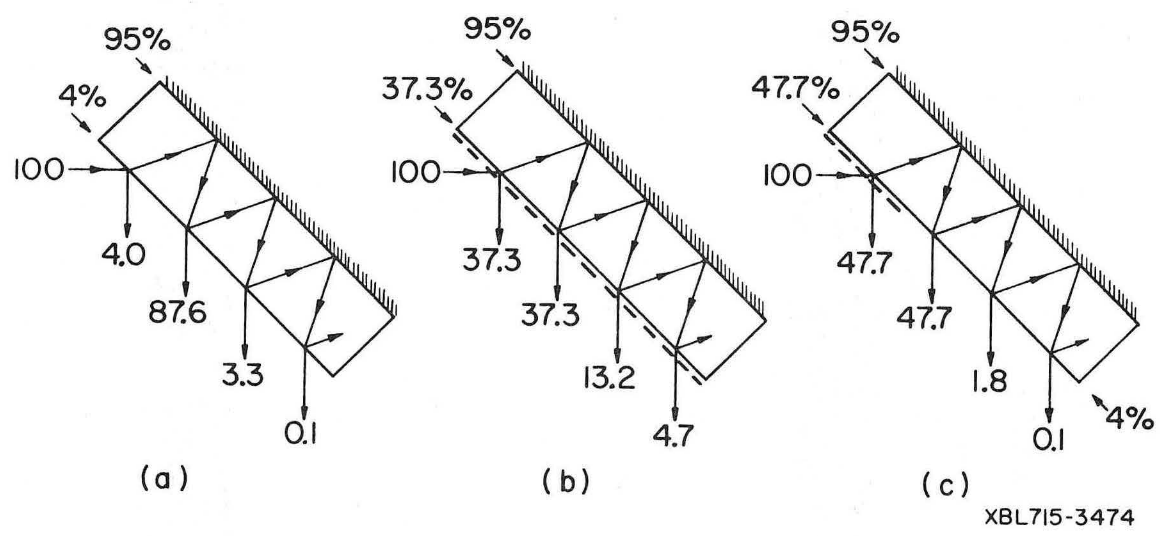


Fig. 21

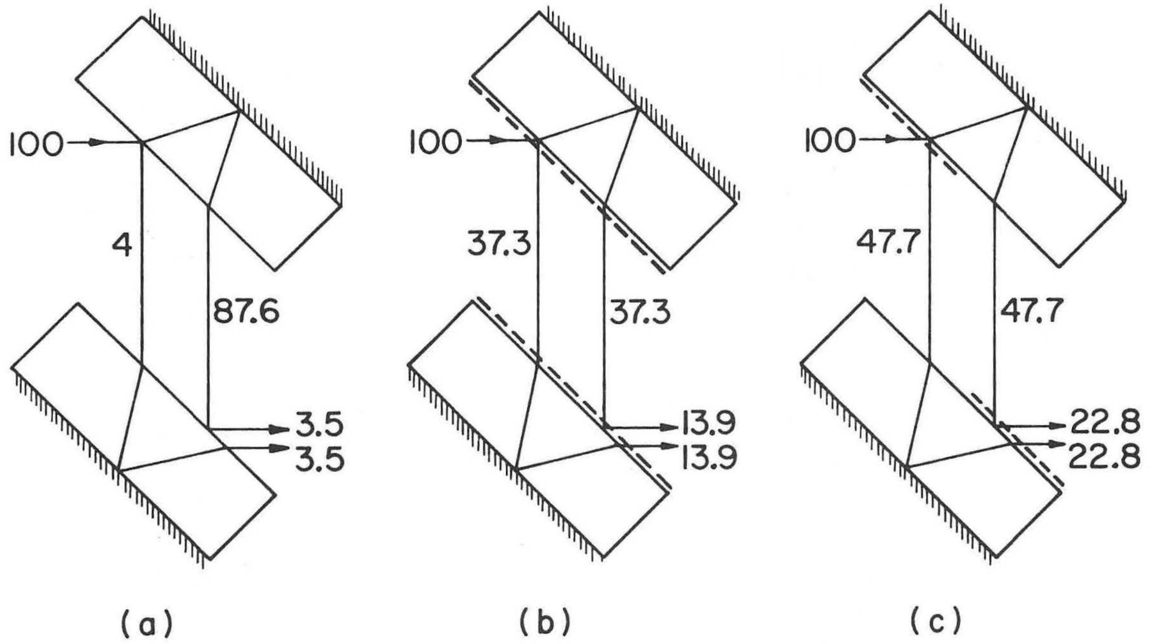


Fig. 22

0 0 0 0 3 6 0 0 0 3 7



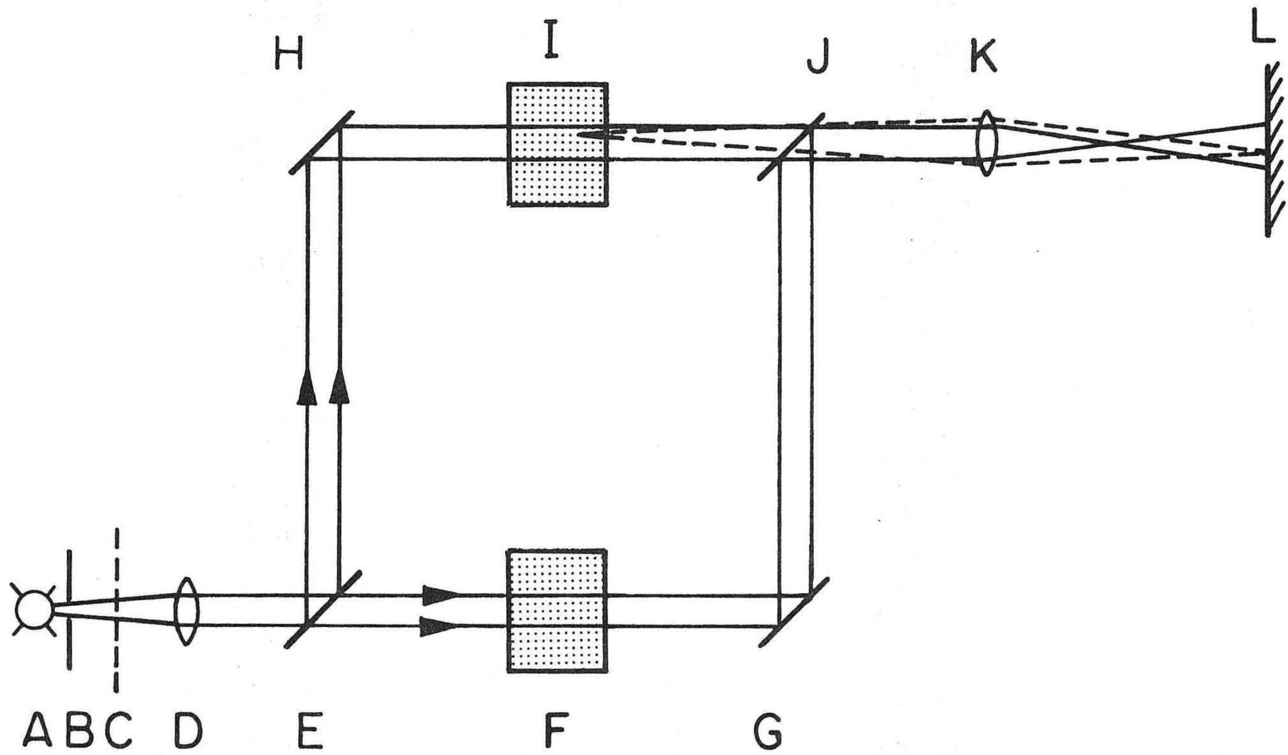


XBL697-3198

Fig. 23

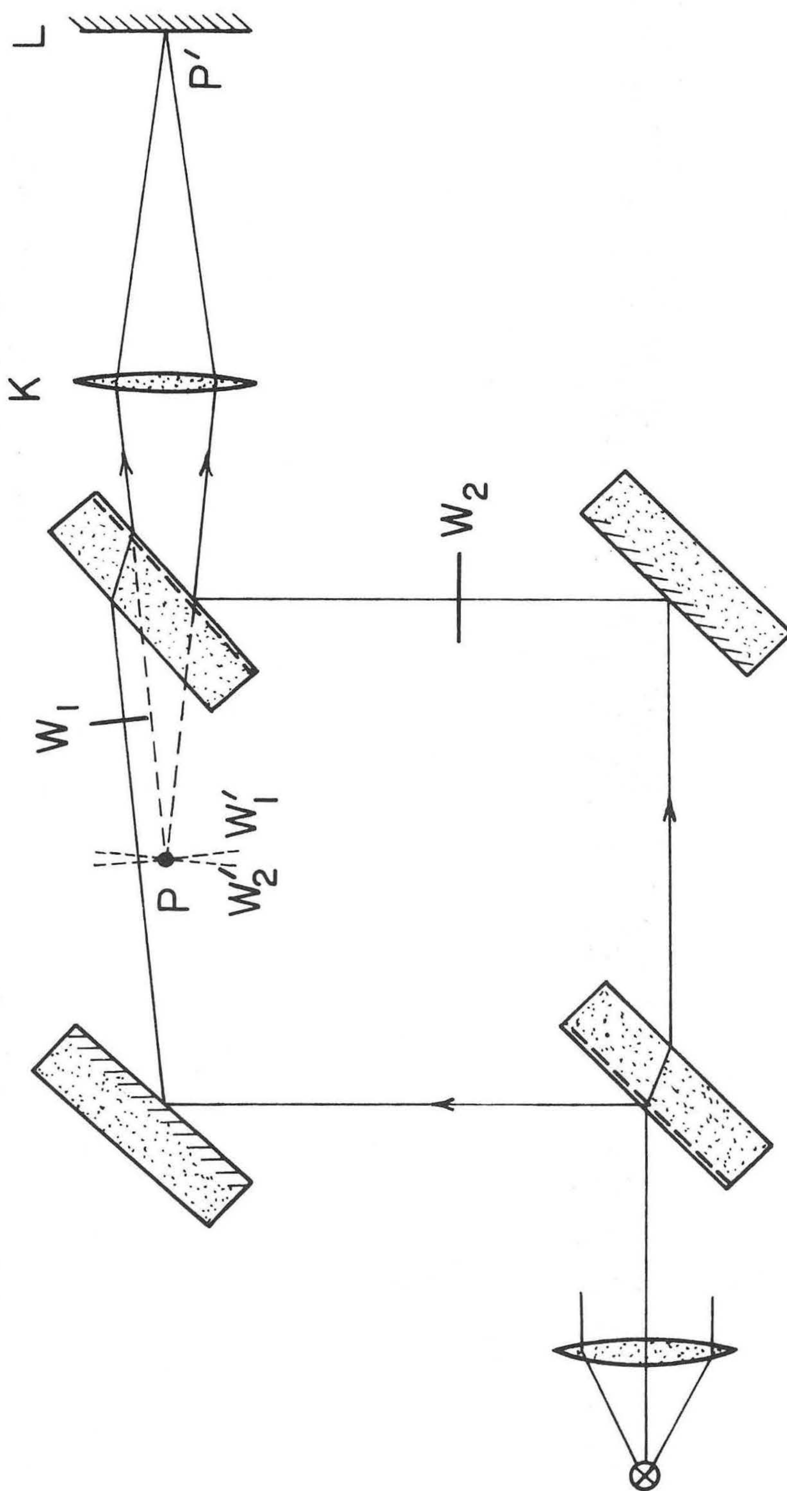


Fig. 24

0 0 0 0 3 6 0 0 0 3 8



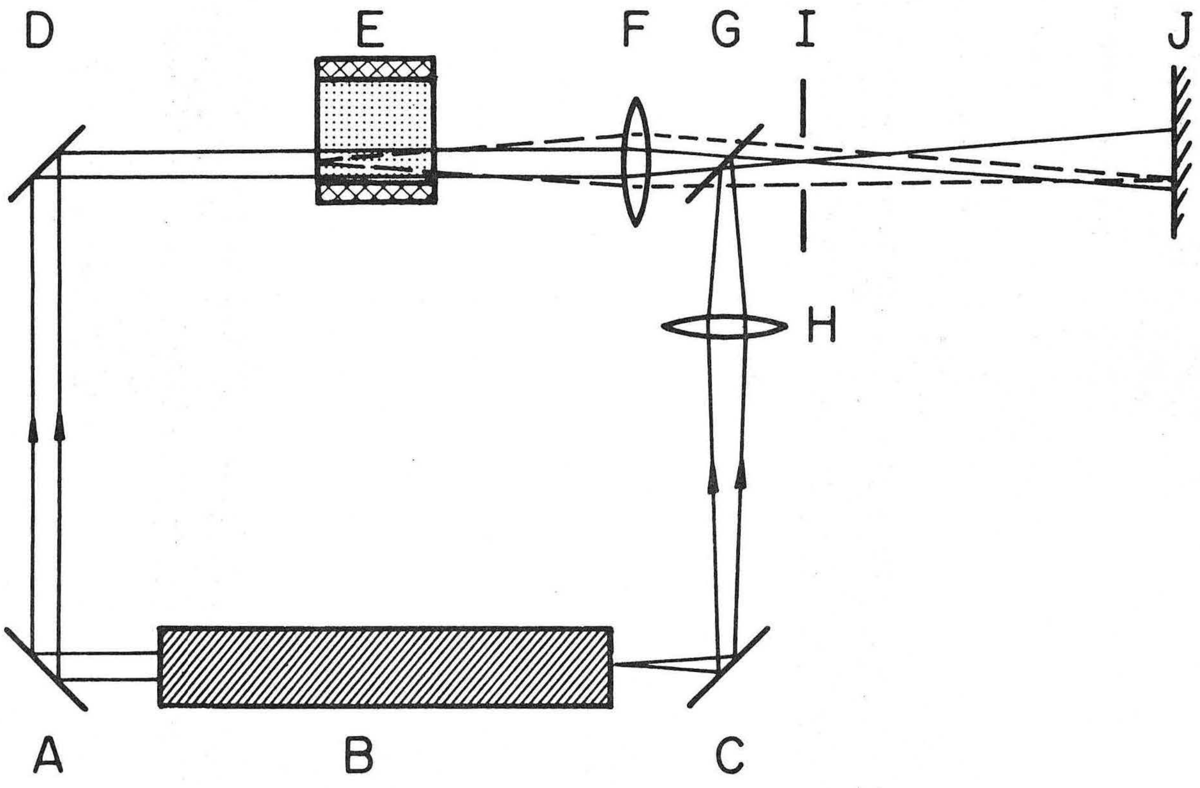


Fig. 25

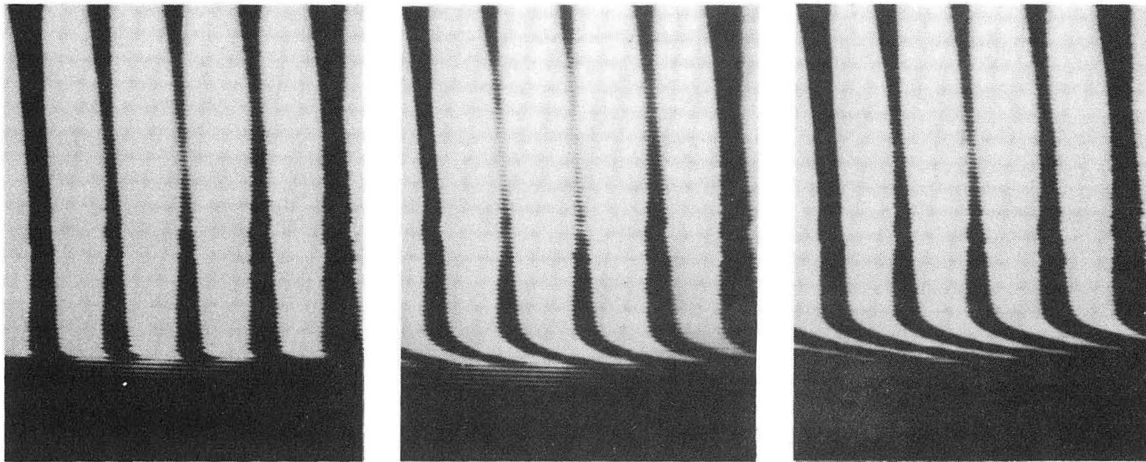

0 sec 2 sec 20 sec

BOUNDARY LAYER DEVELOPMENT

4 cm from leading edge, 66 mA/$cm^2$, 0.1M $CuSO_4$, Re = 1100

XBB 694-2708

Fig. 26

0 0 0 0 3 6 0 0 0 3 9



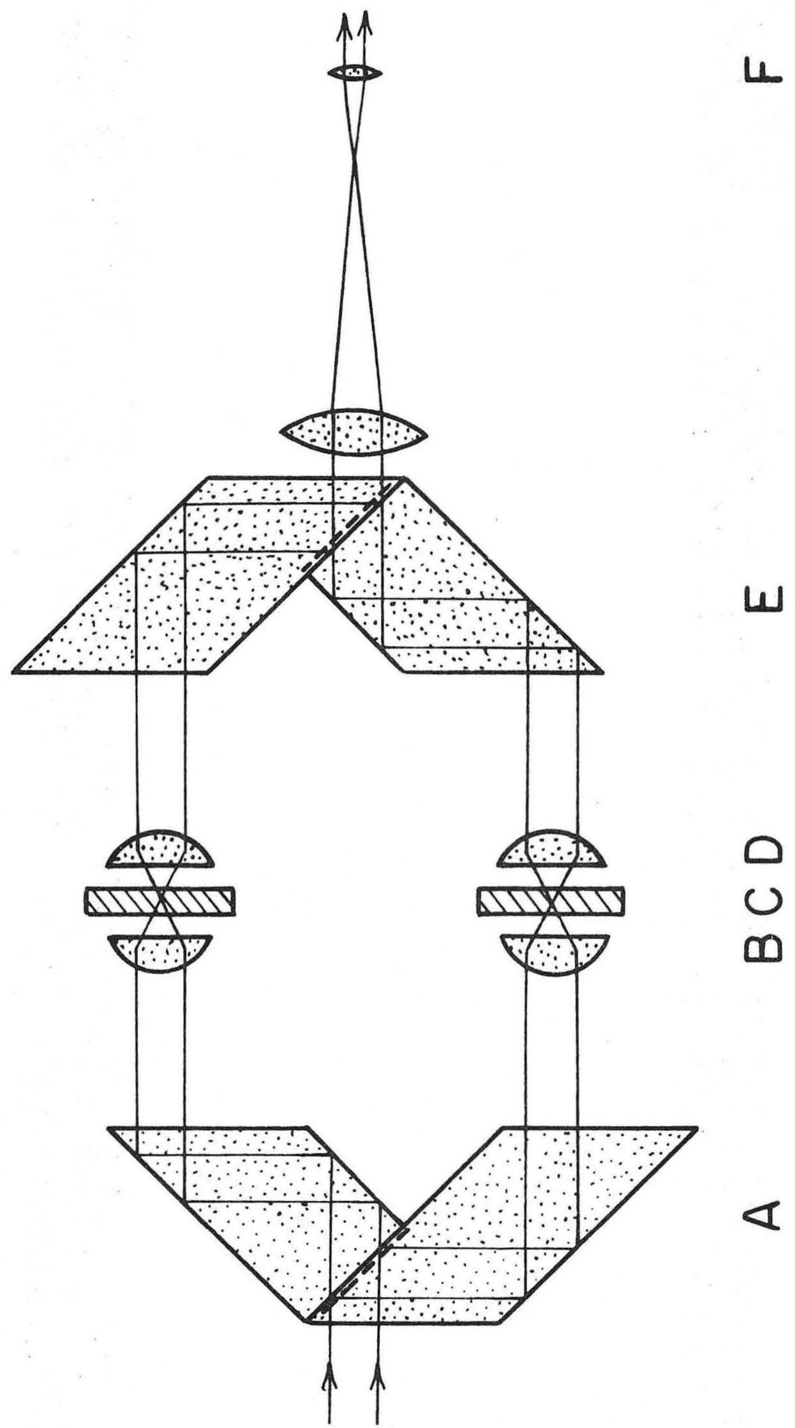


Fig. 27

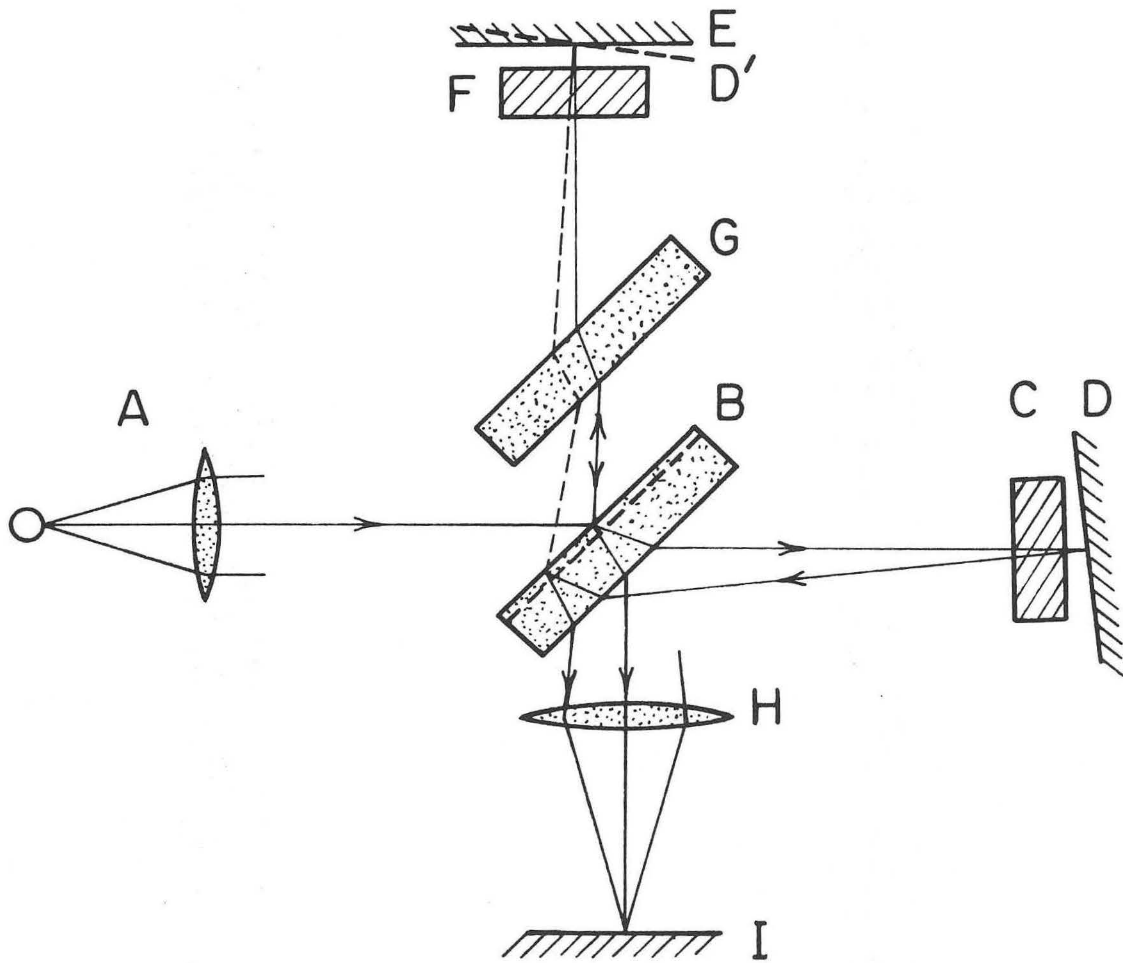


Fig. 28

0 0 0 0 3 6 0 0 0 4 0



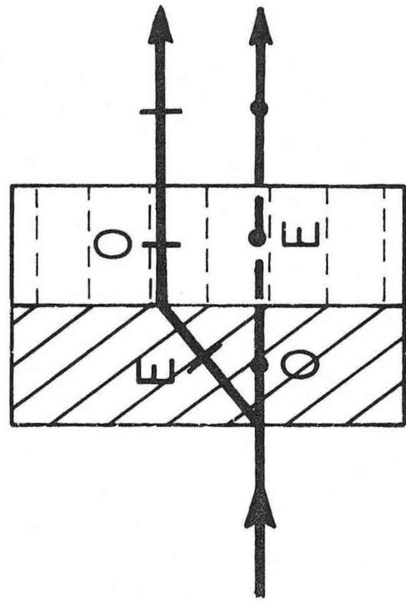


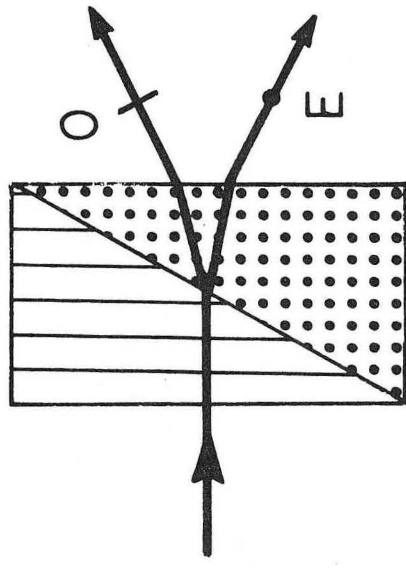


Fig. 29

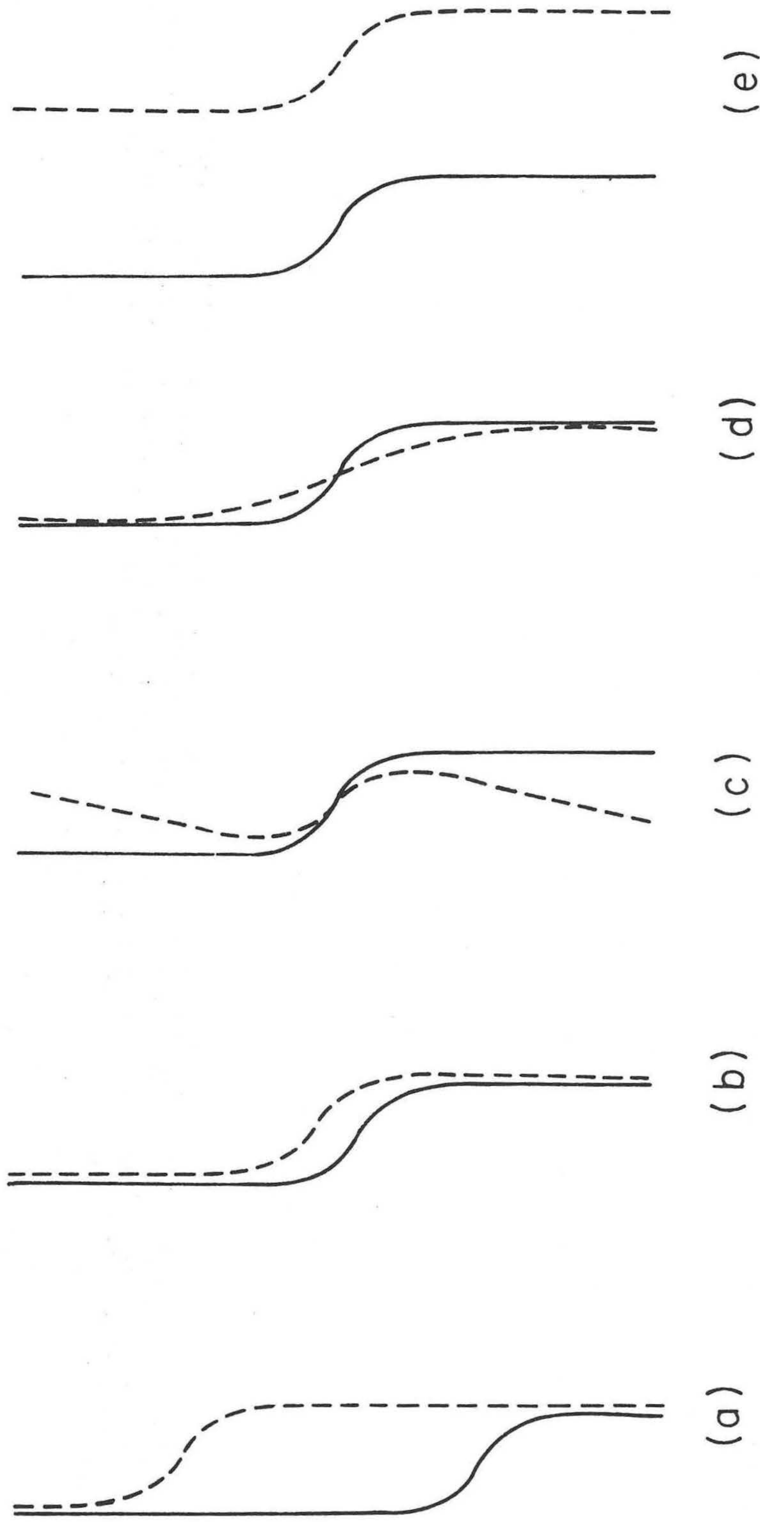


Fig. 30

0 0 0 0 3 6 0 0 0 4 1



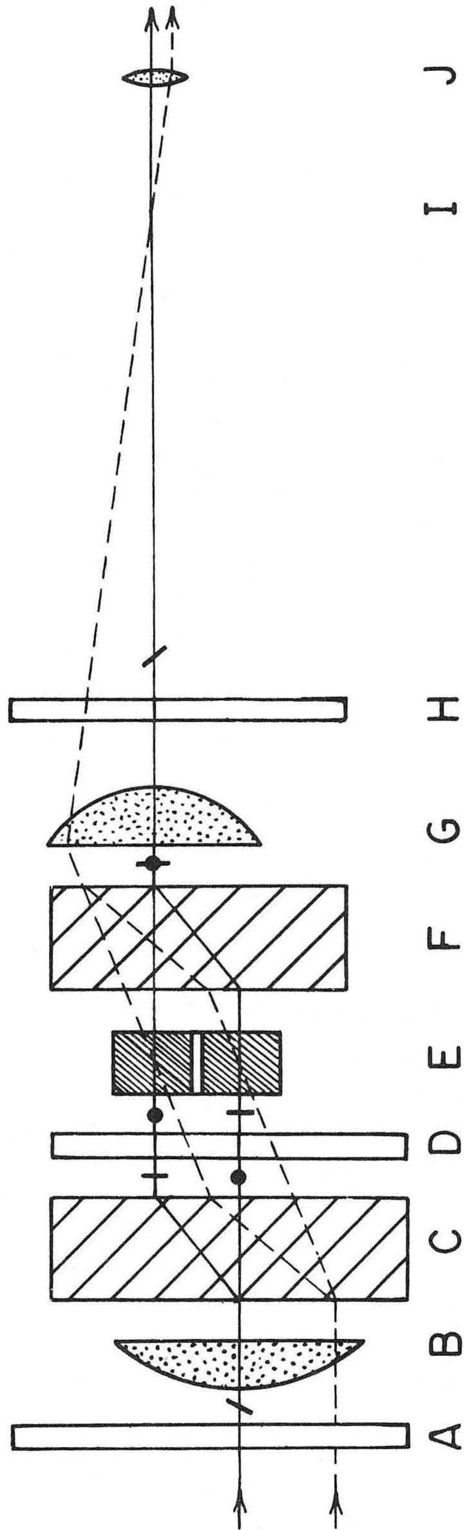


Fig. 31

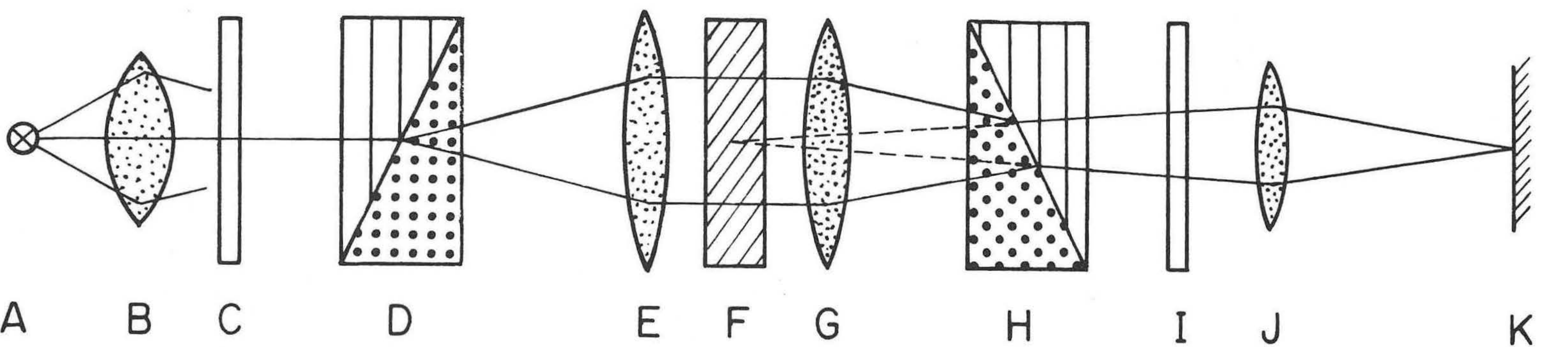


Fig. 32

0 0 0 0 3 6 0 0 0 4 2



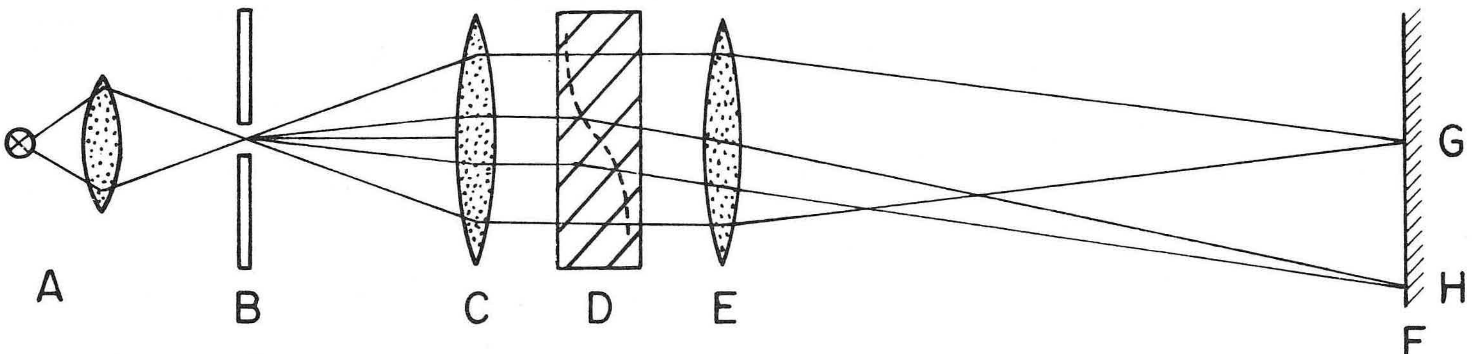


Fig. 33

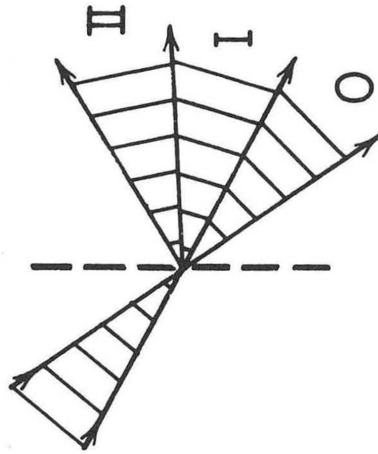


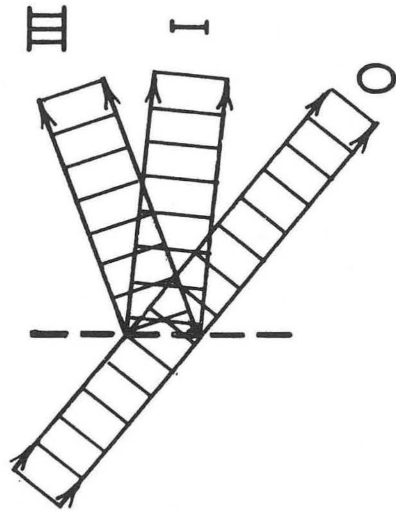


XBL716-3794

Fig. 34

0 0 0 0 3 6 0 0 0 4 3



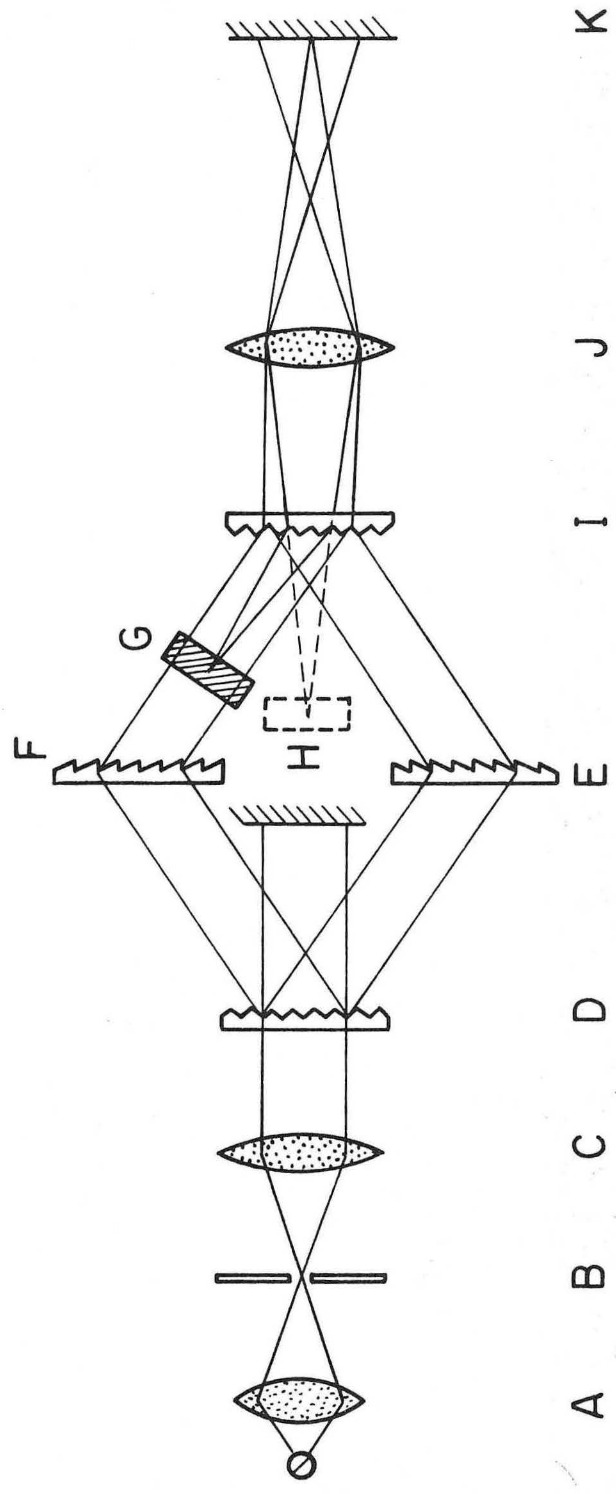


Fig. 35

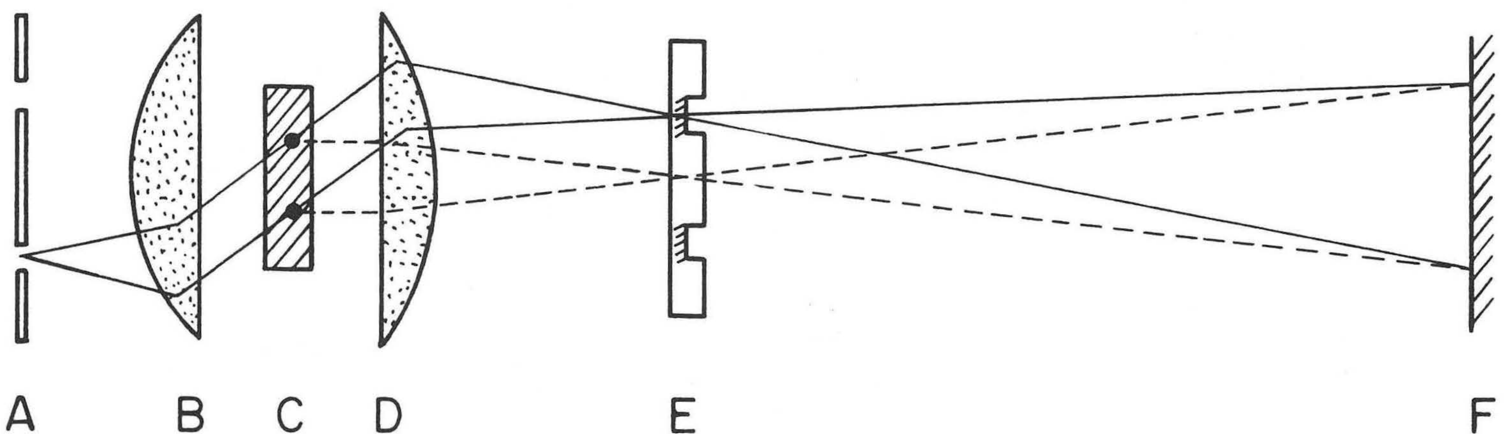


Fig. 36

0 0 0 0 3 6 0 0 0 4 4



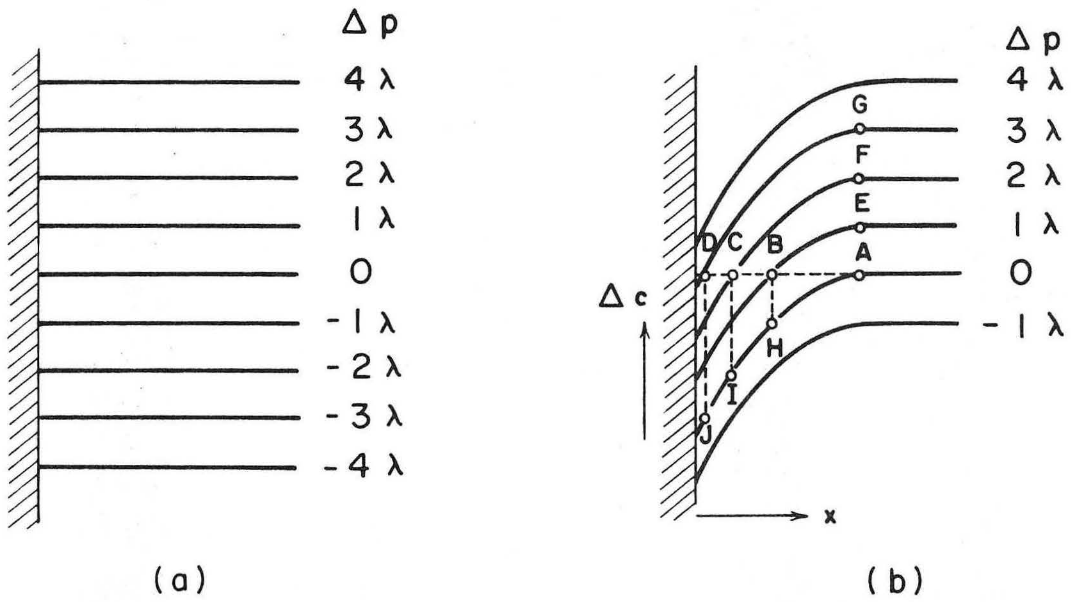


XBL717-3871

Fig. 37

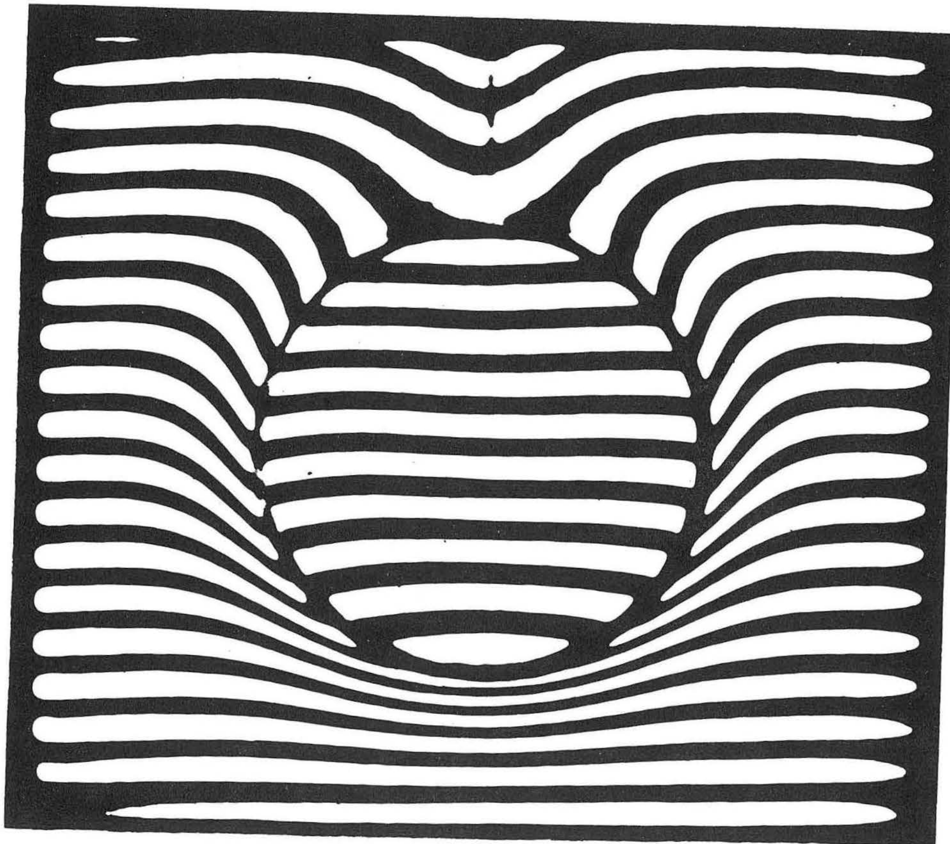

MU-35624

Fig. 38

0 0 0 0 3 6 0 0 0 4 5



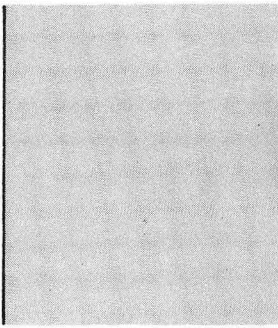

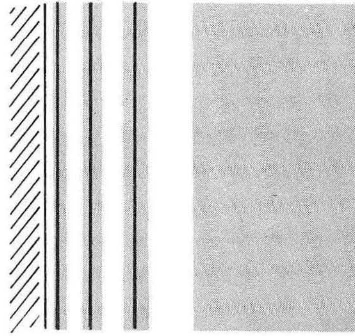

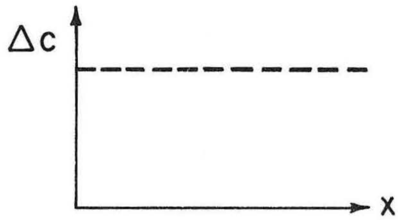


(a)

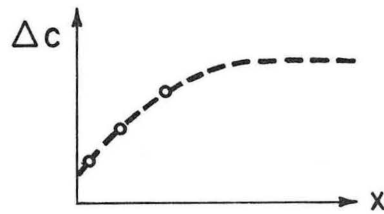


(b)

XBL717-3870

Fig. 39

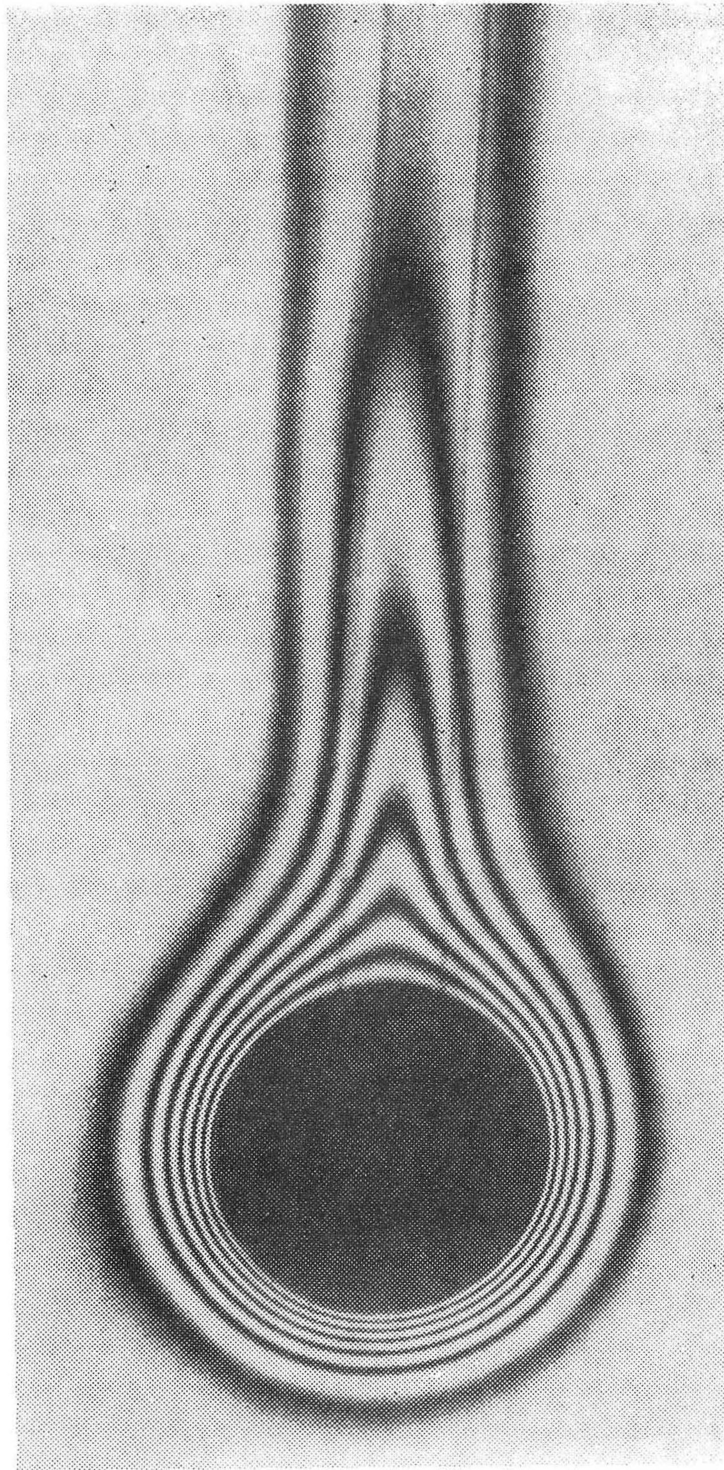

XBB 718-3559

Fig. 40

0 0 0 0 3 6 0 0 0 4 6



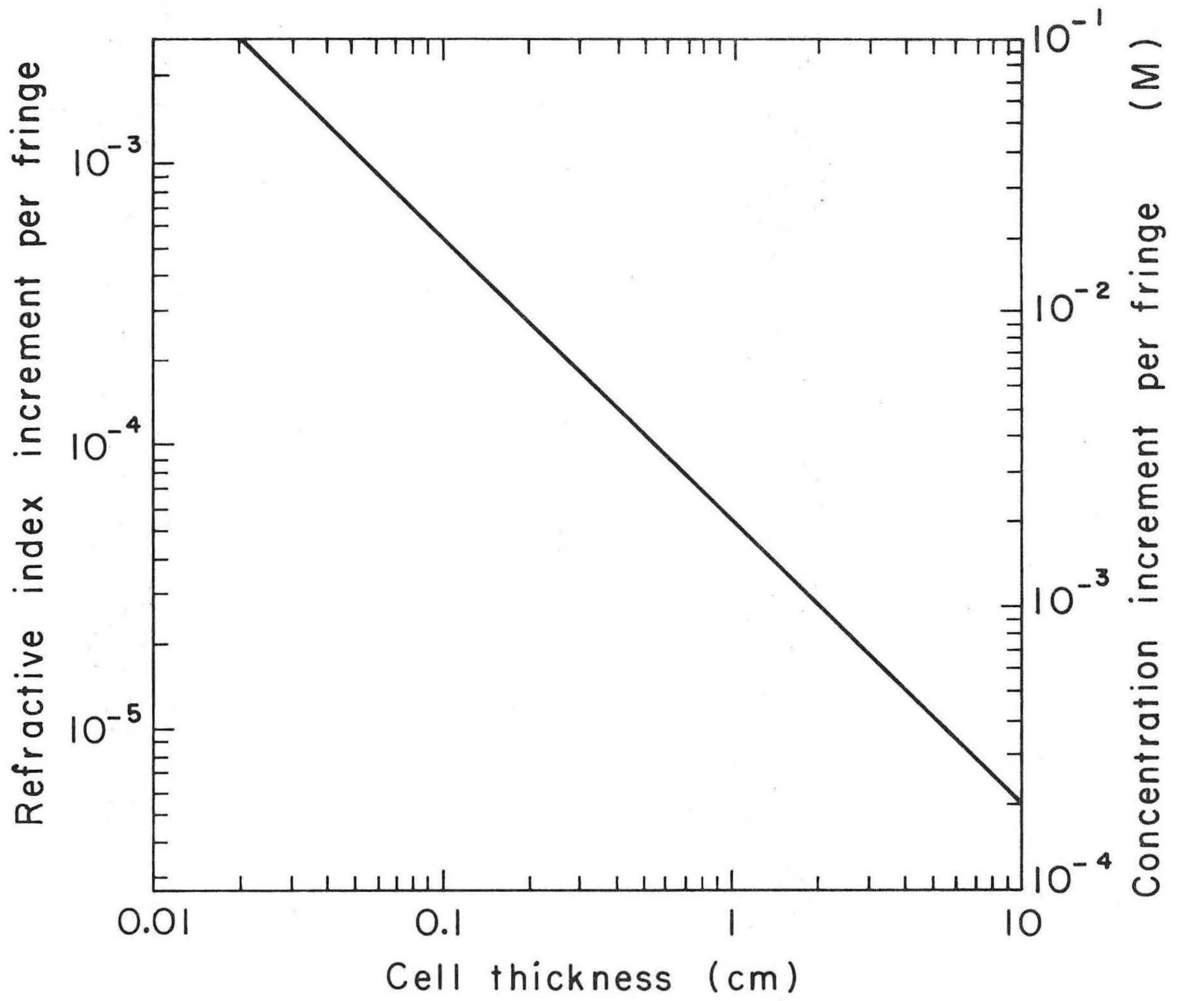


XBL717-3875

Fig. 41

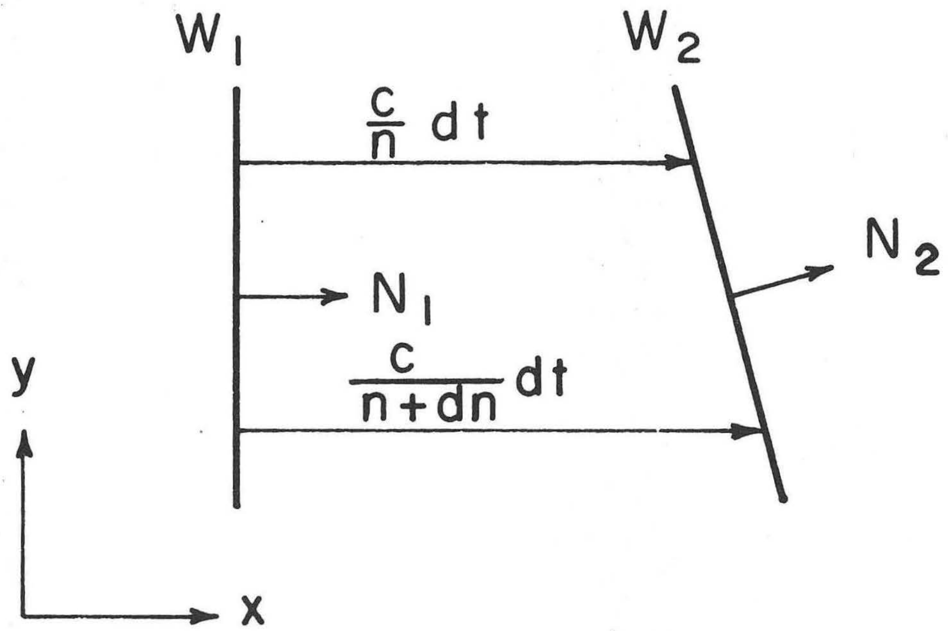


Fig. 42

0 0 0 0 3 6 0 0 0 4 7



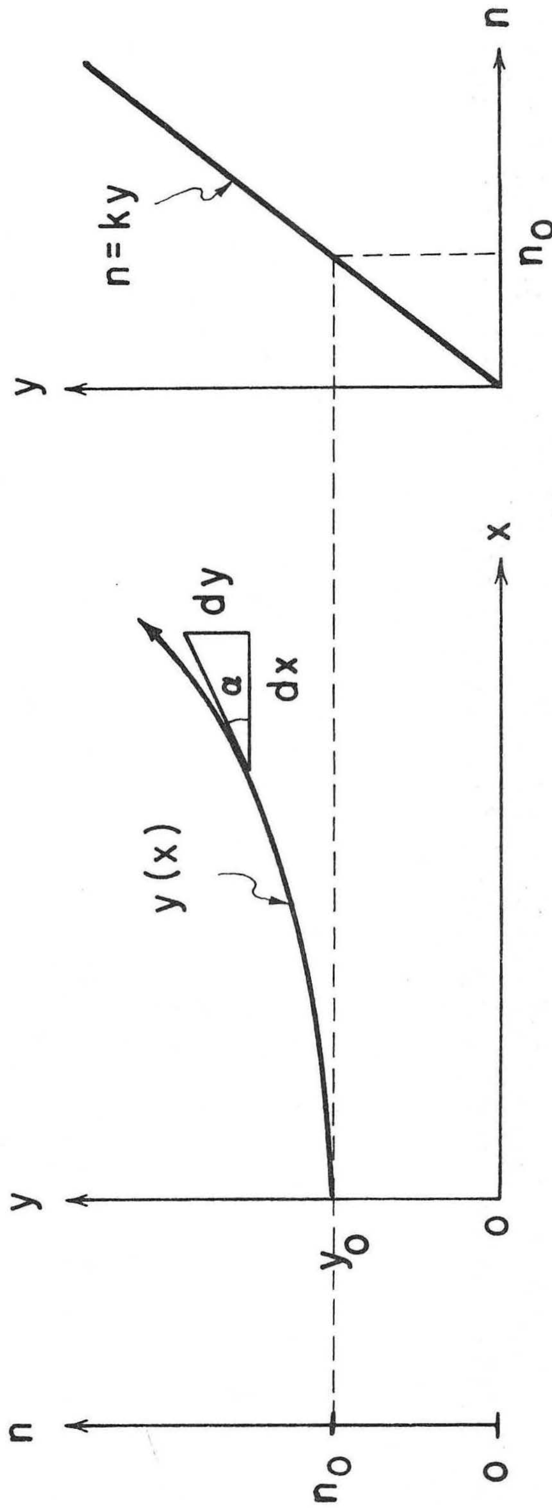


XBL717-3873

Fig. 43

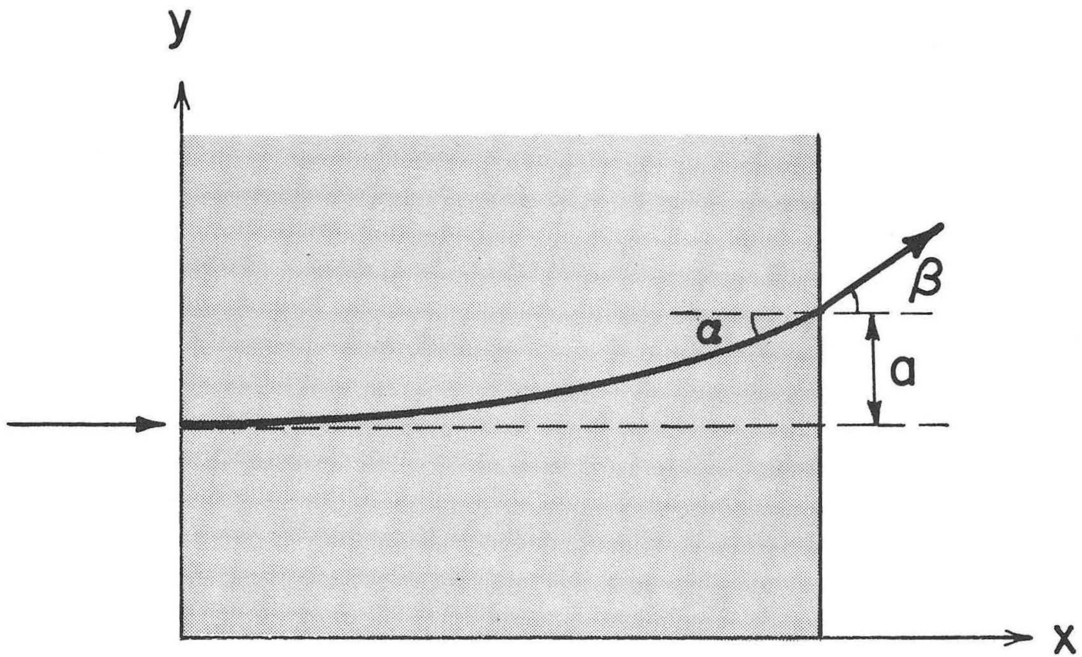


XBL717-3874

Fig. 44

0 0 0 0 3 6 0 0 0 4 8



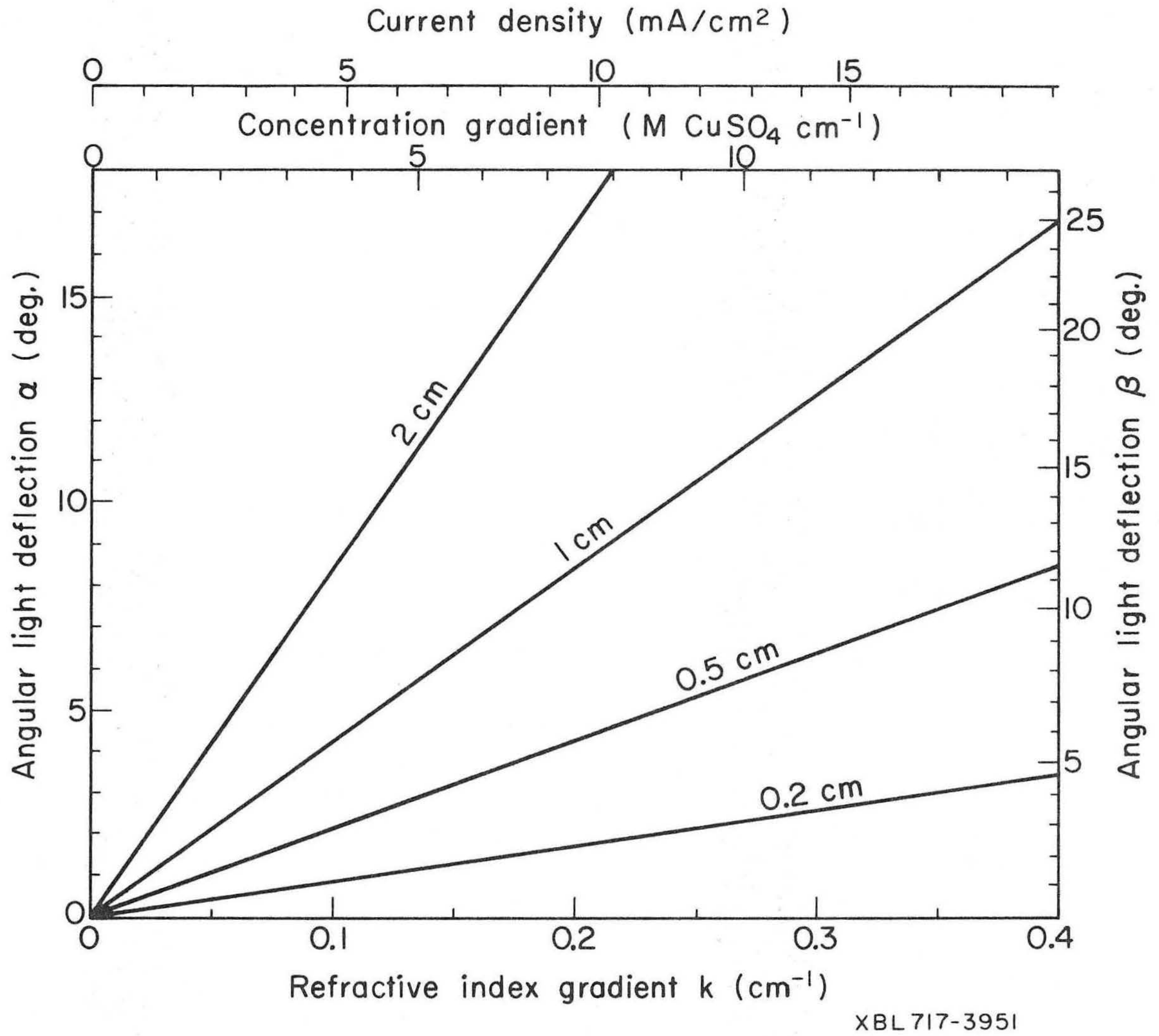


Fig. 45

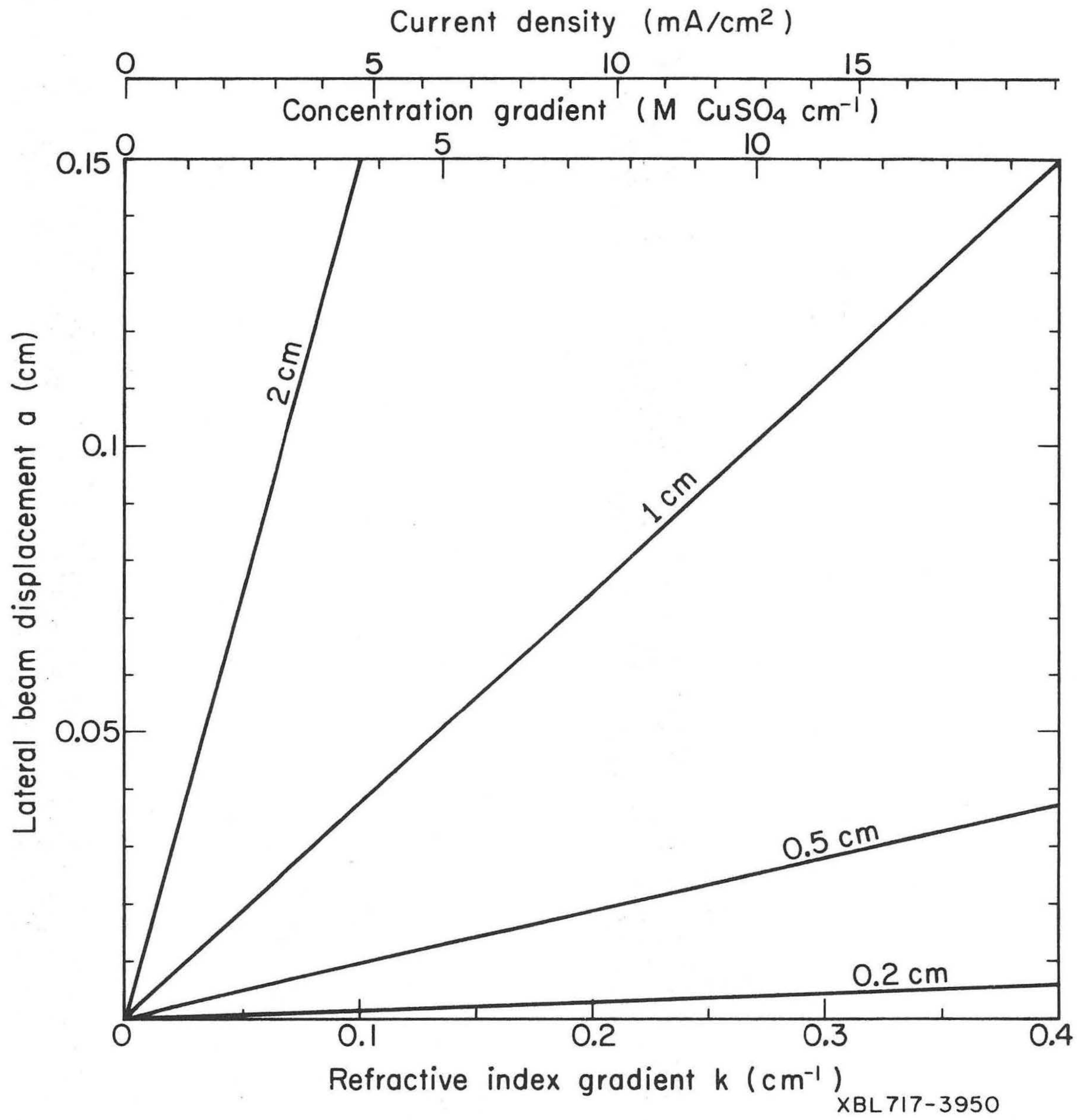


Fig. 46

0 0 0 0 3 6 0 0 0 4 9



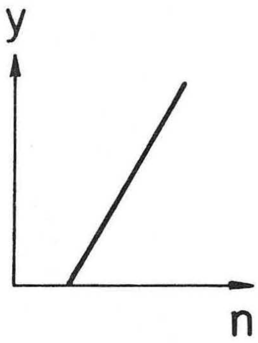


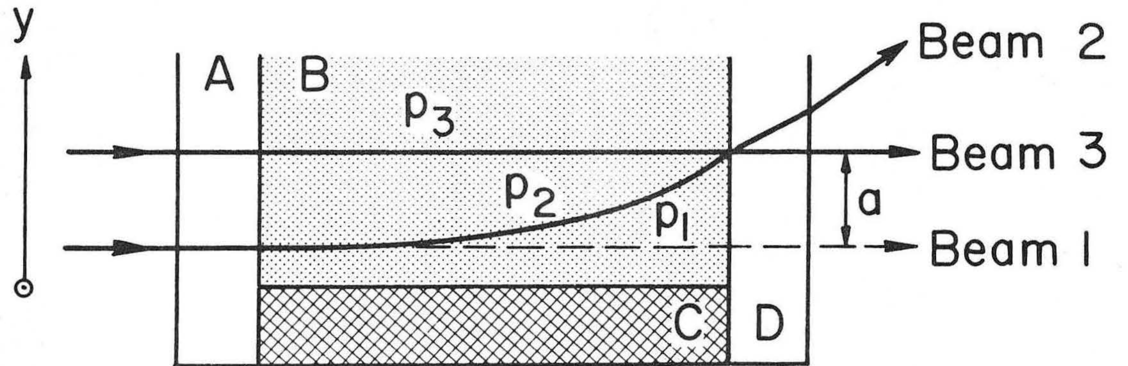


(a) (b)

XBL697-3199

Fig. 47

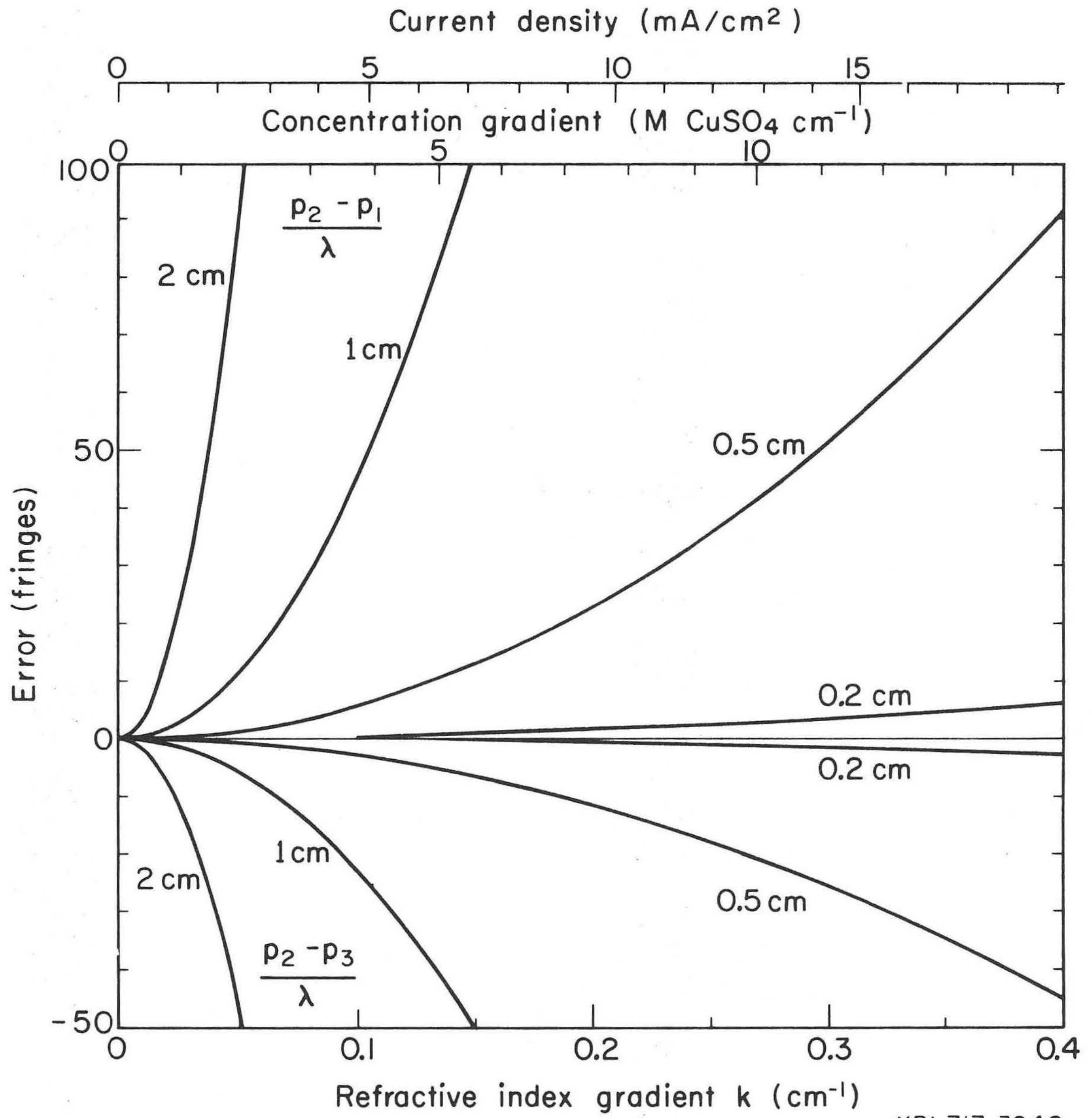


Fig. 48

0 0 0 0 3 6 0 0 0 5 0



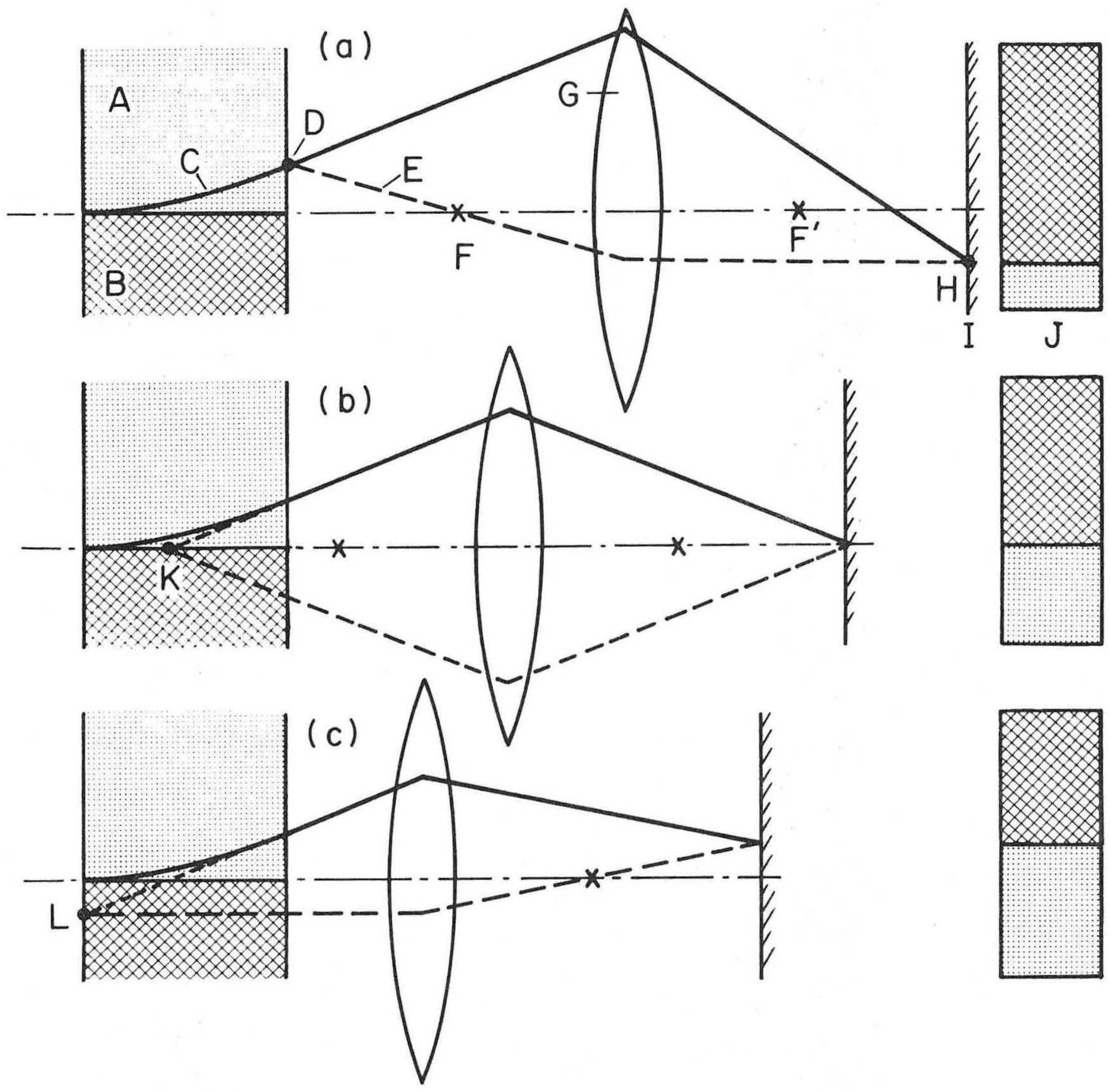


Fig. 49

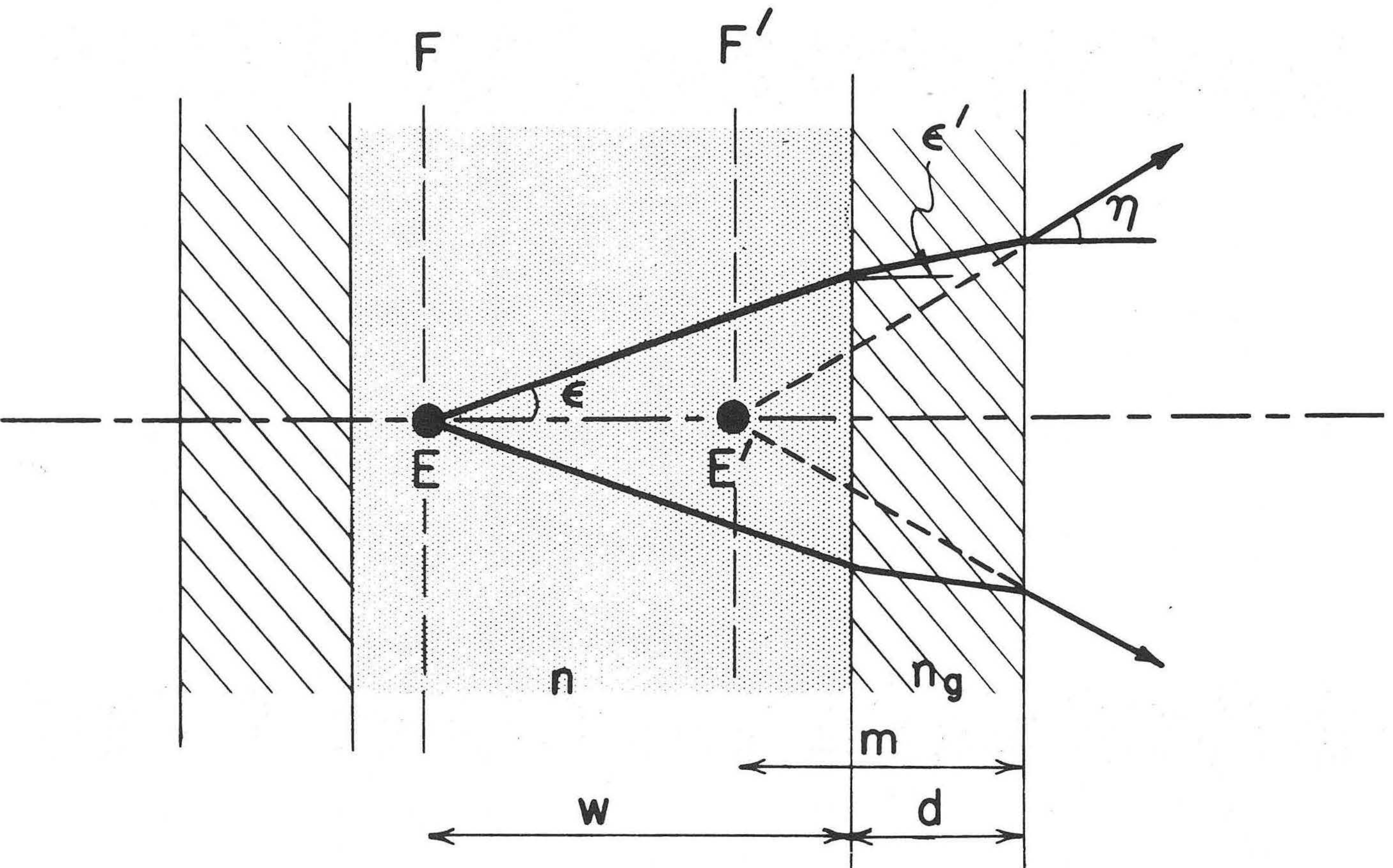


Fig. 50

0 0 0 0 3 6 0 0 0 5 1



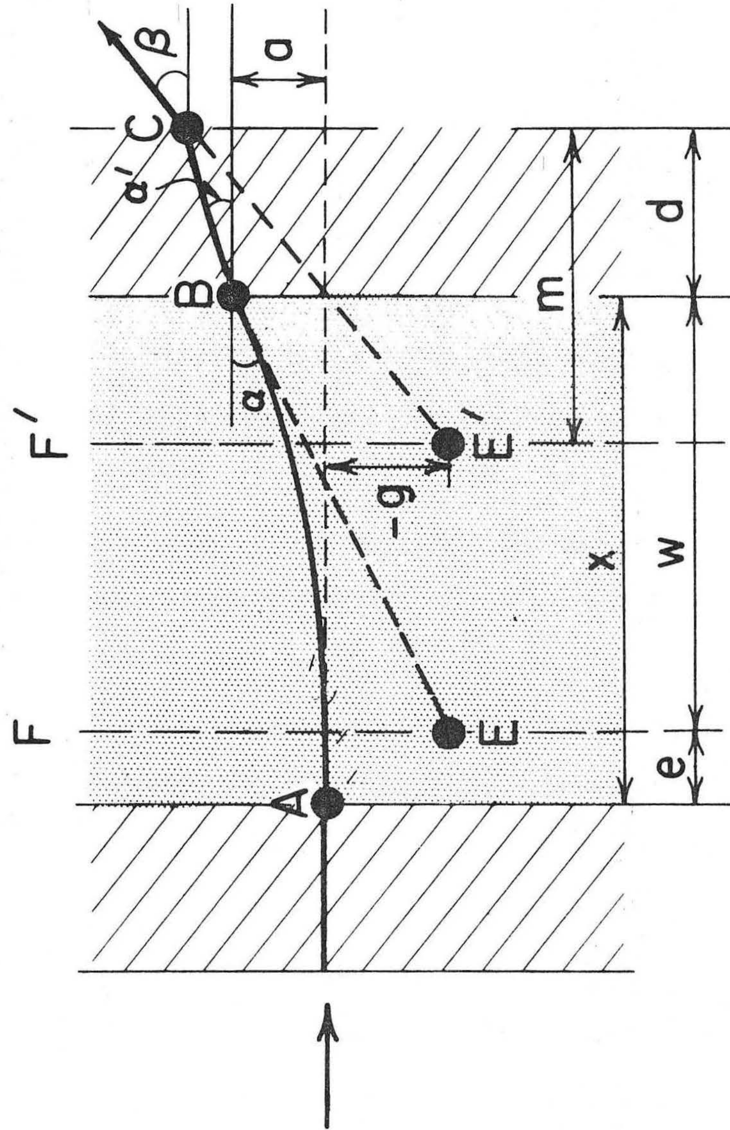


Fig. 51

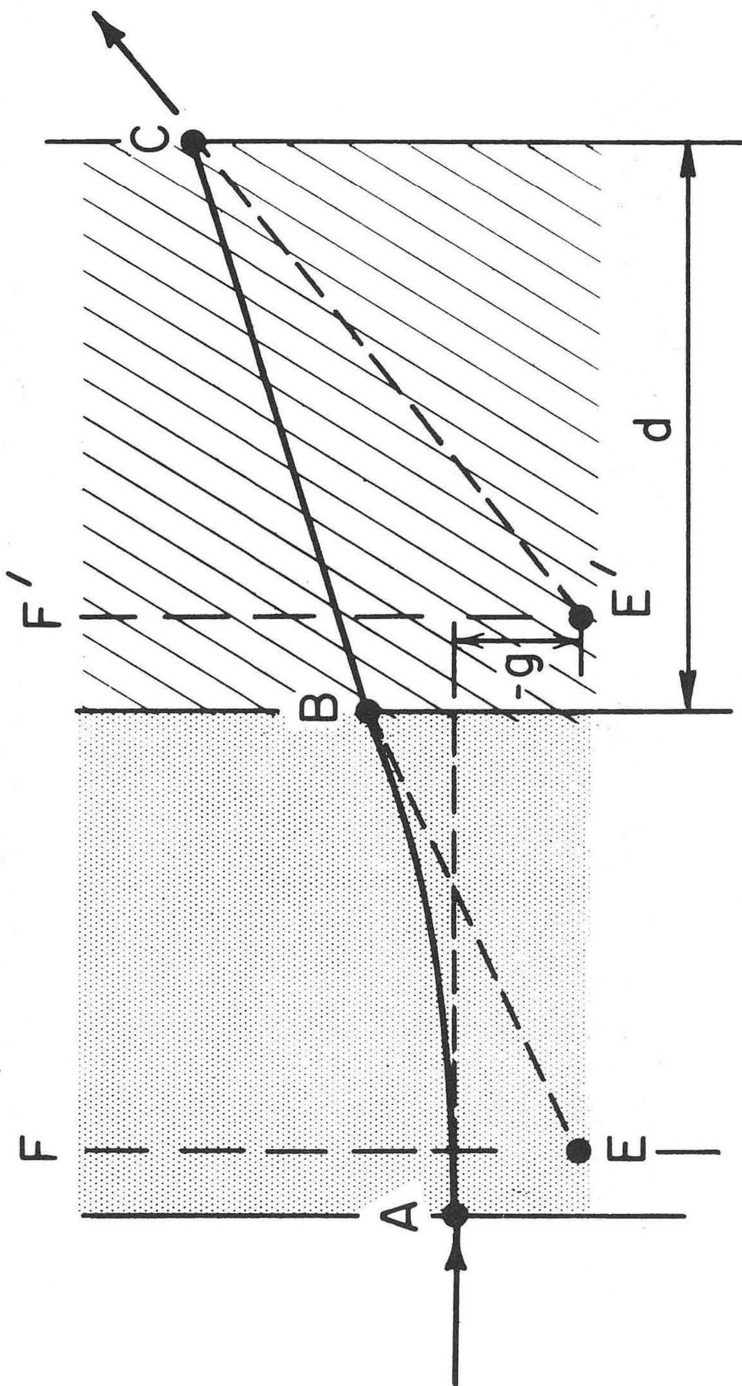


Fig. 52

0 0 0 0 3 6 0 0 0 3 2



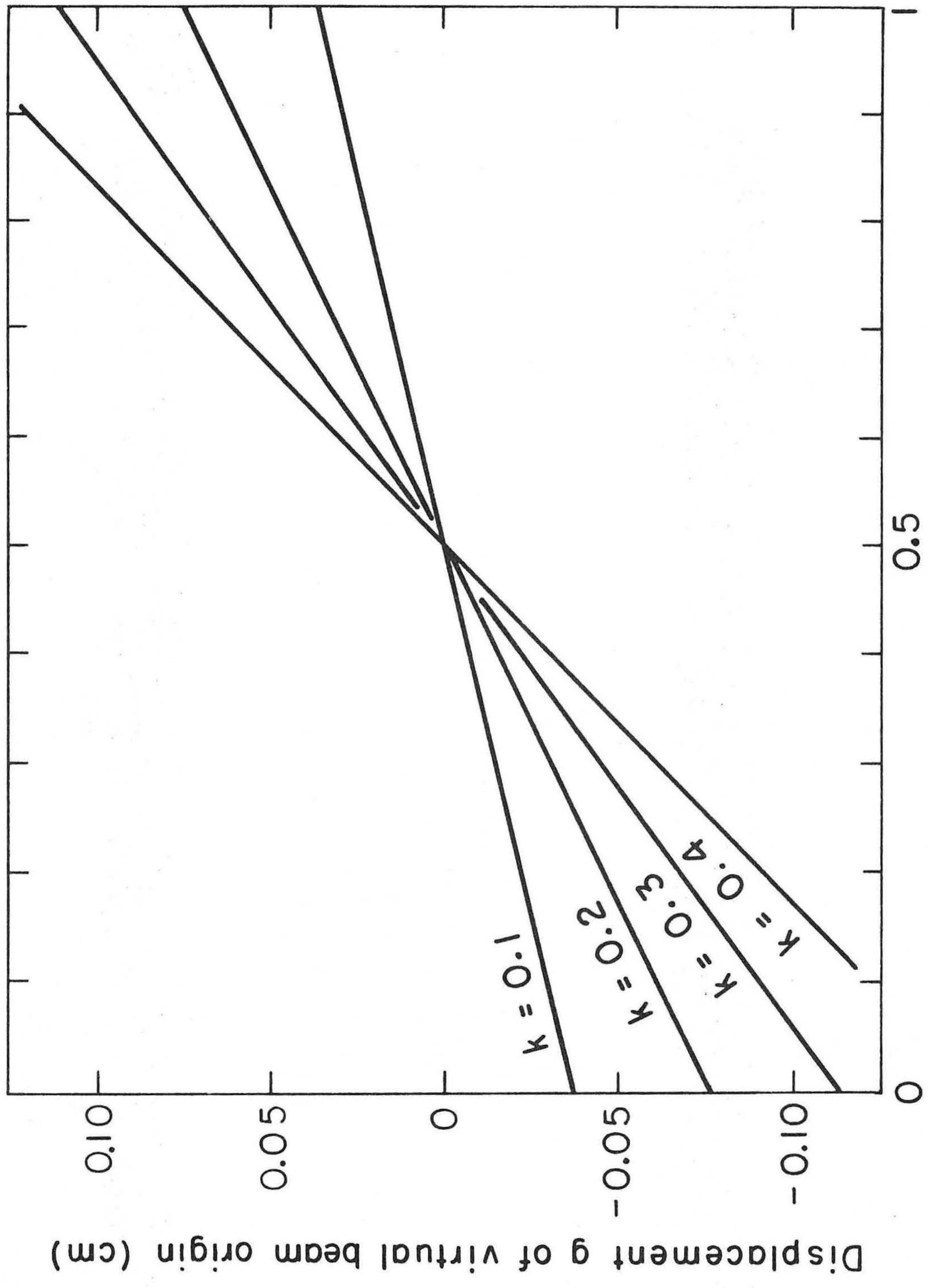


Fig. 53

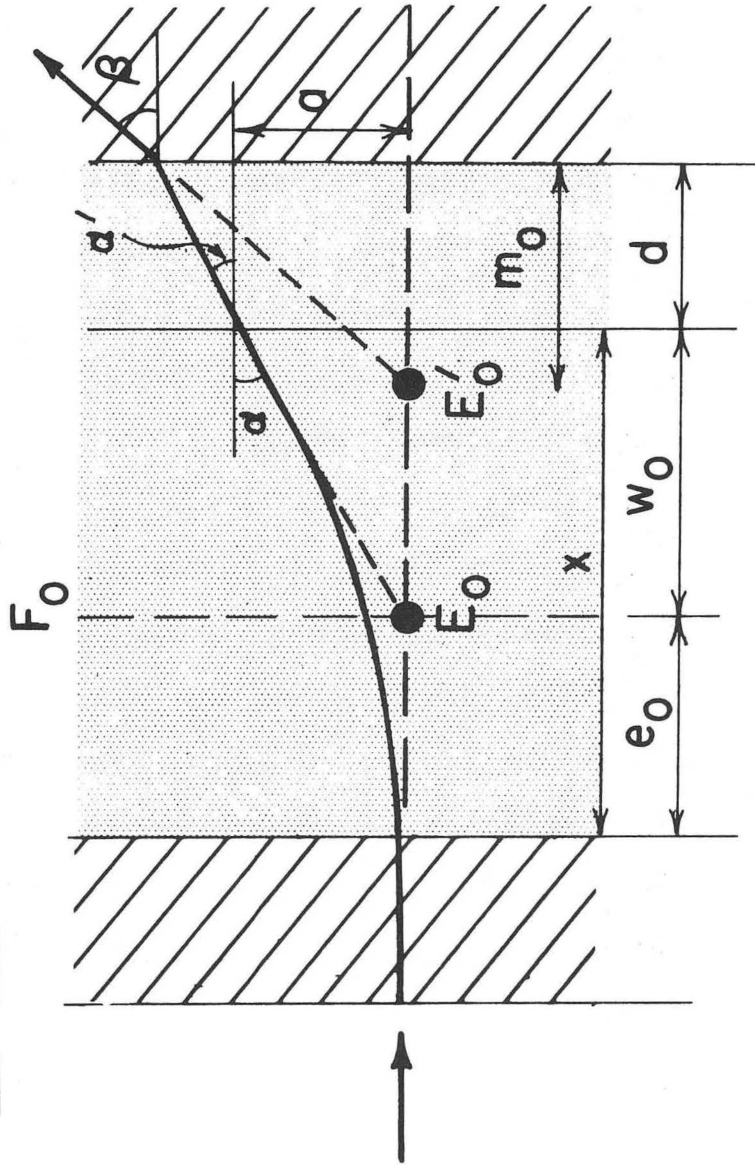


XBL723-2549

Fig. 54

0 0 0 0 3 6 0 3 0 5 3



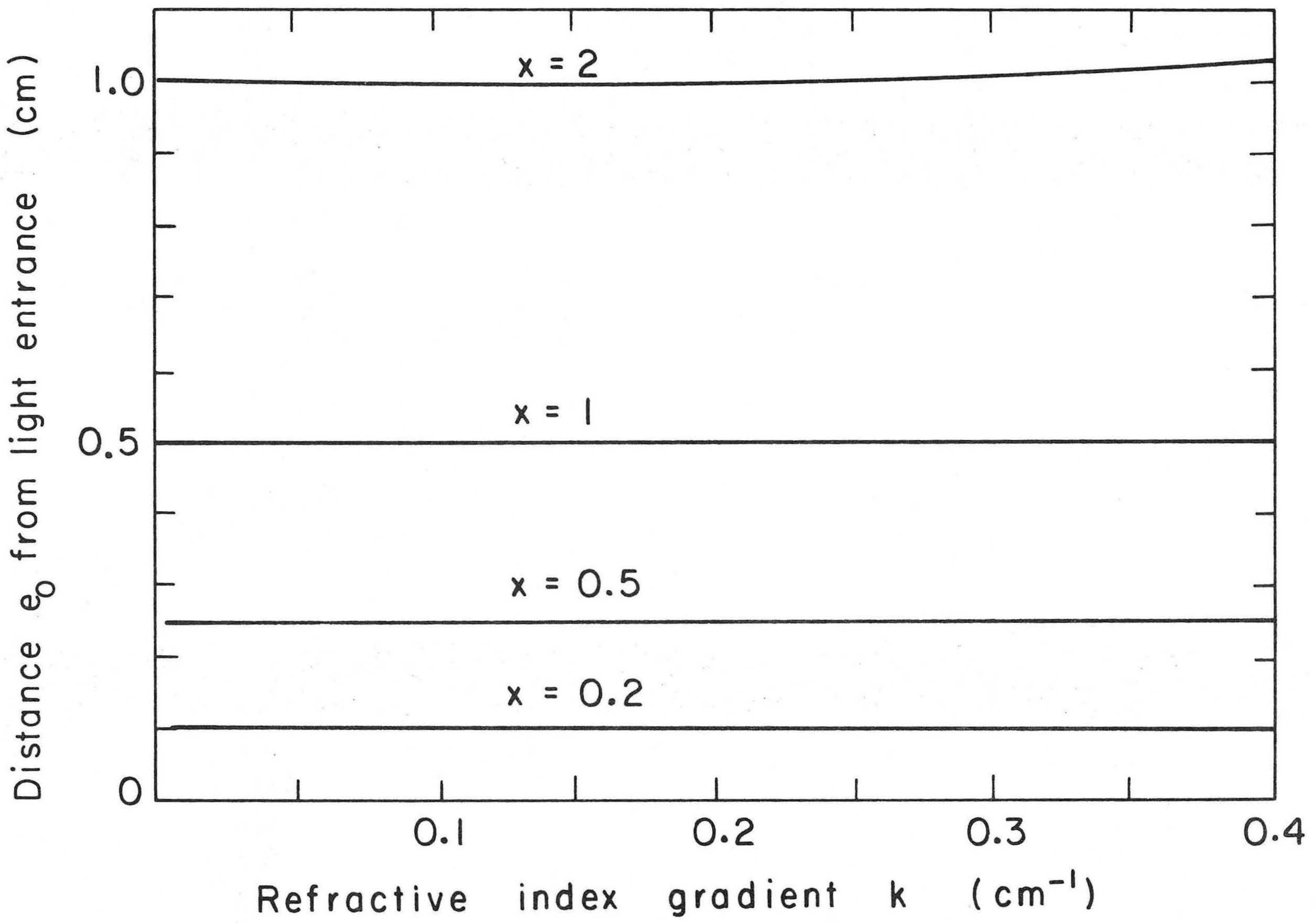


Fig. 55

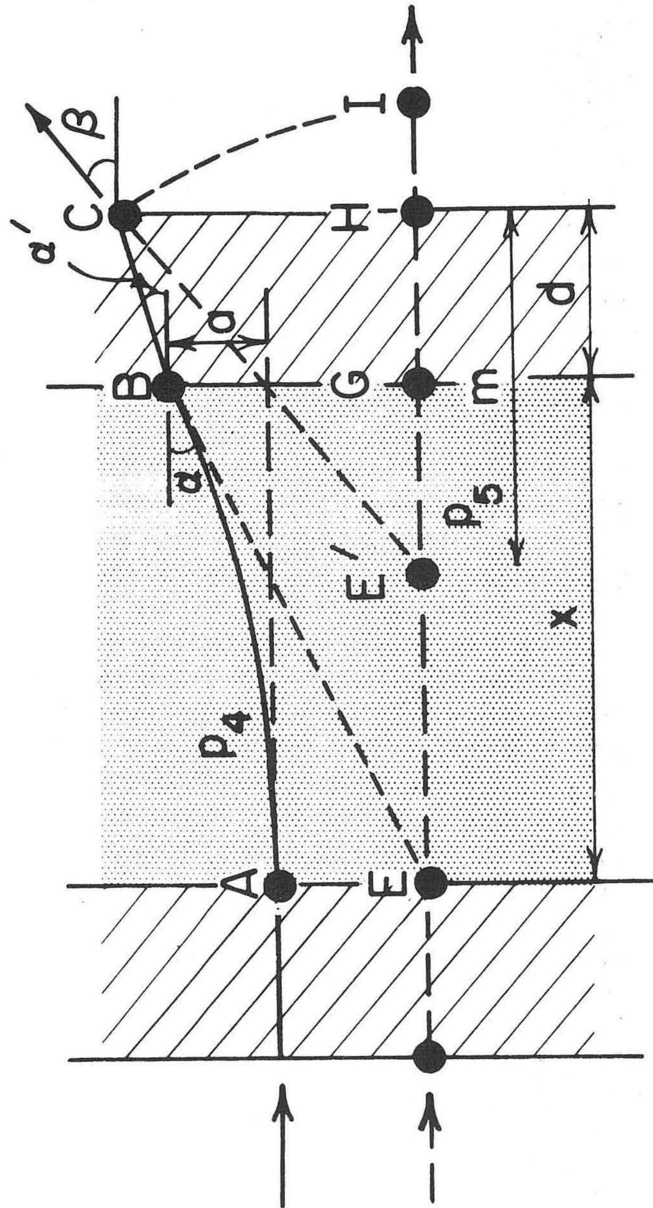


Fig. 56

0 0 0 0 3 6 0 0 0 3 4



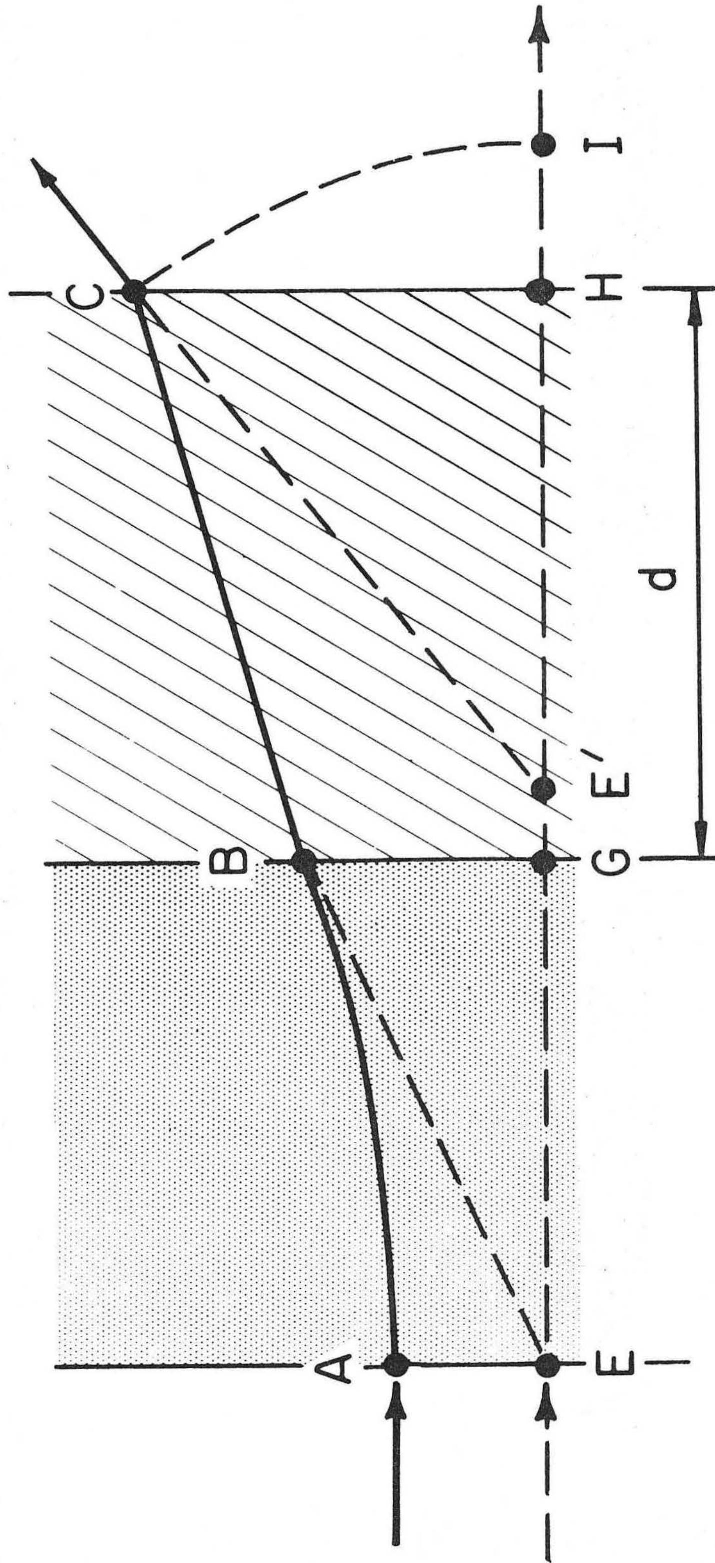


Fig. 57

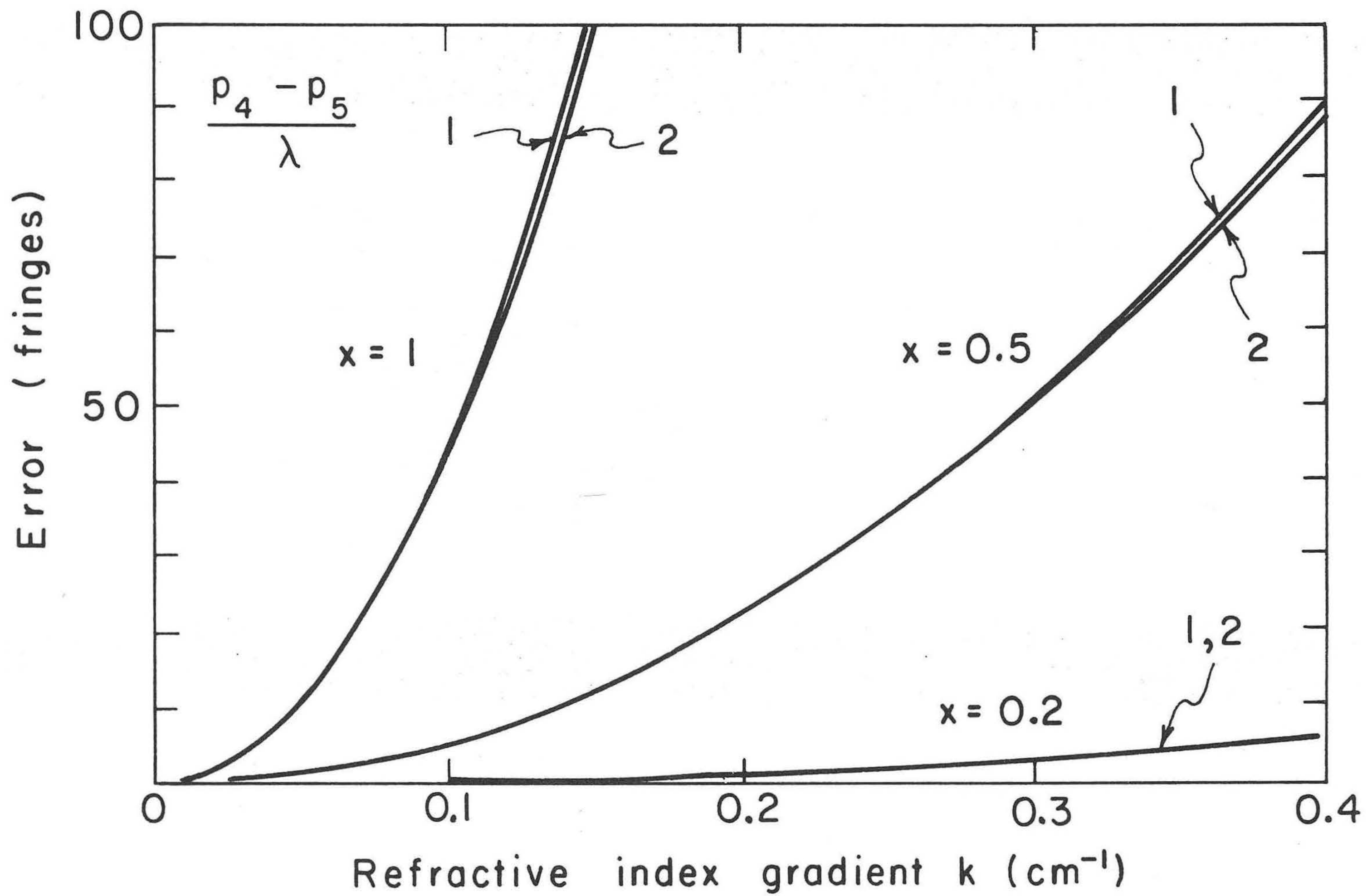


Fig. 58

0 0 0 0 3 6 0 6 0 5 5



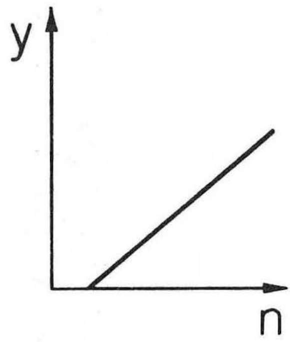


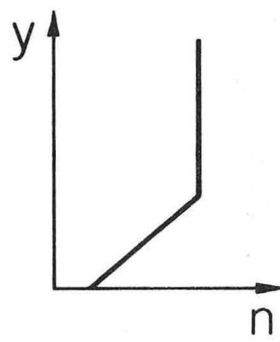


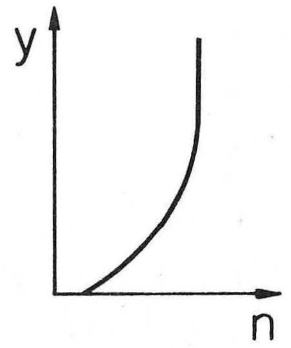


XBL717-3961

Fig. 59

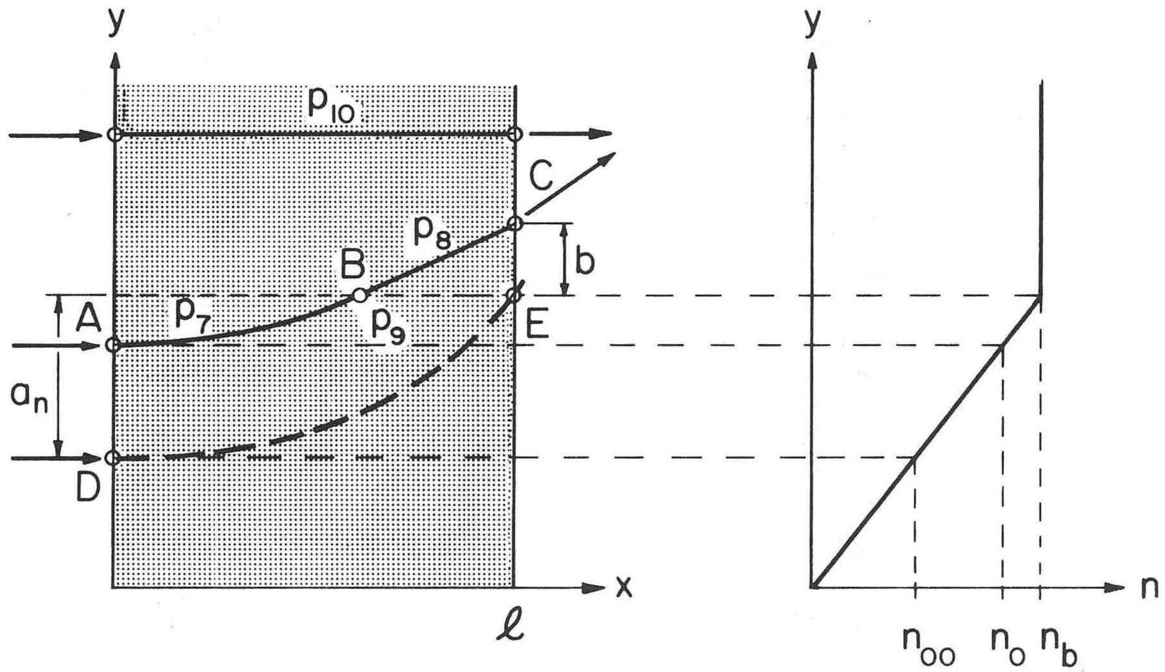


Fig. 60

0 0 0 0 3 6 0 0 0 5 6



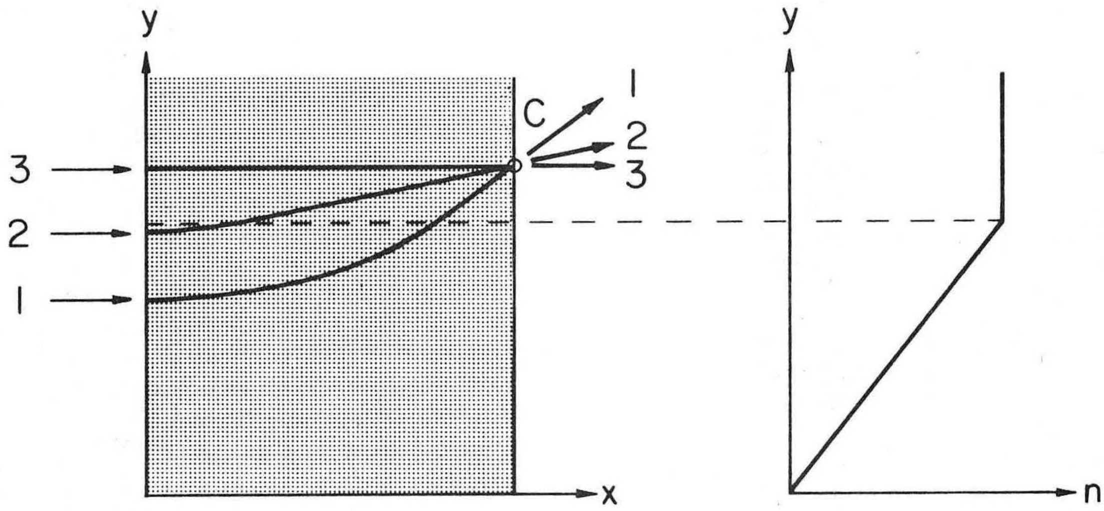


Fig. 61

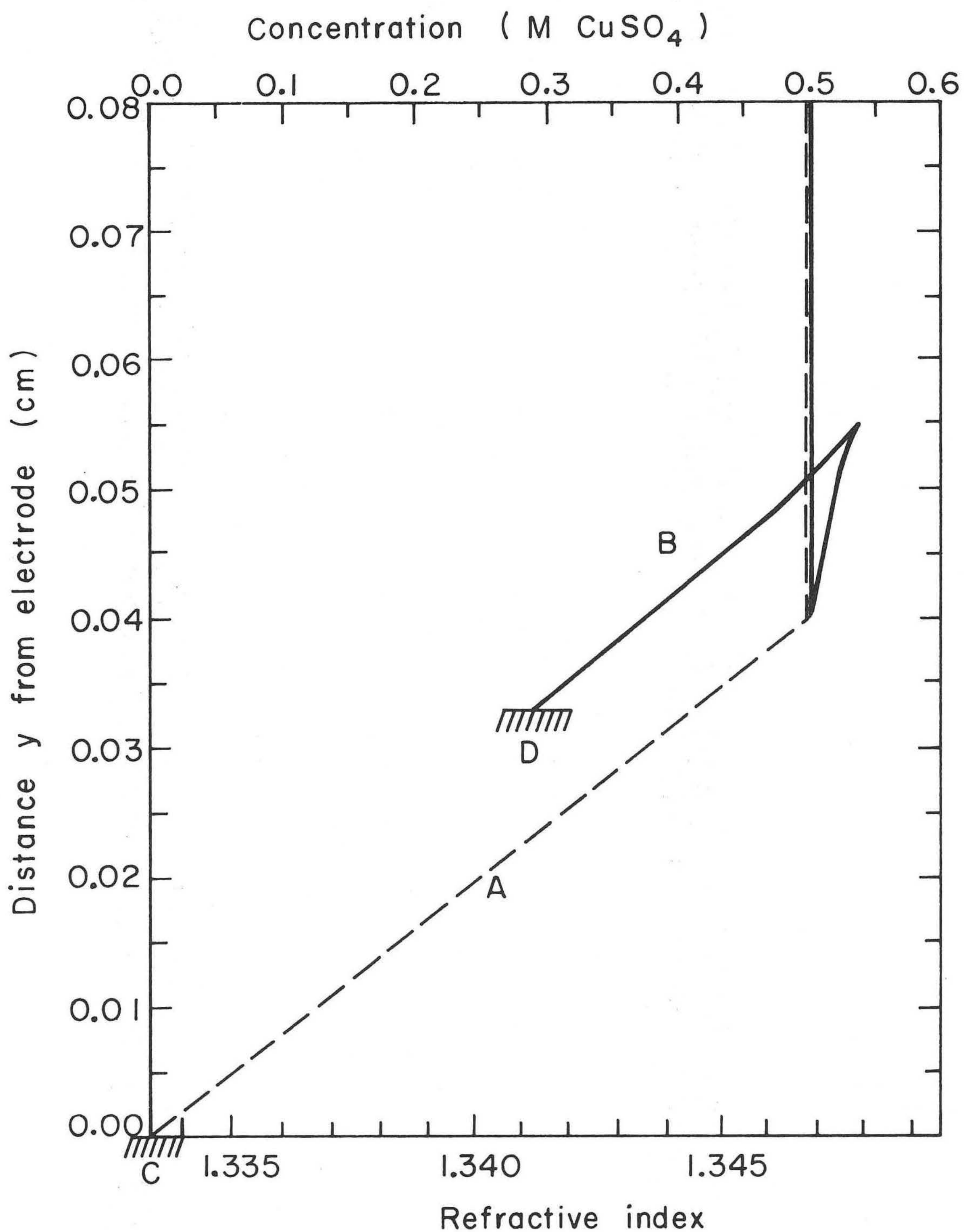


Fig. 62

0 0 0 0 3 6 0 0 0 5 7



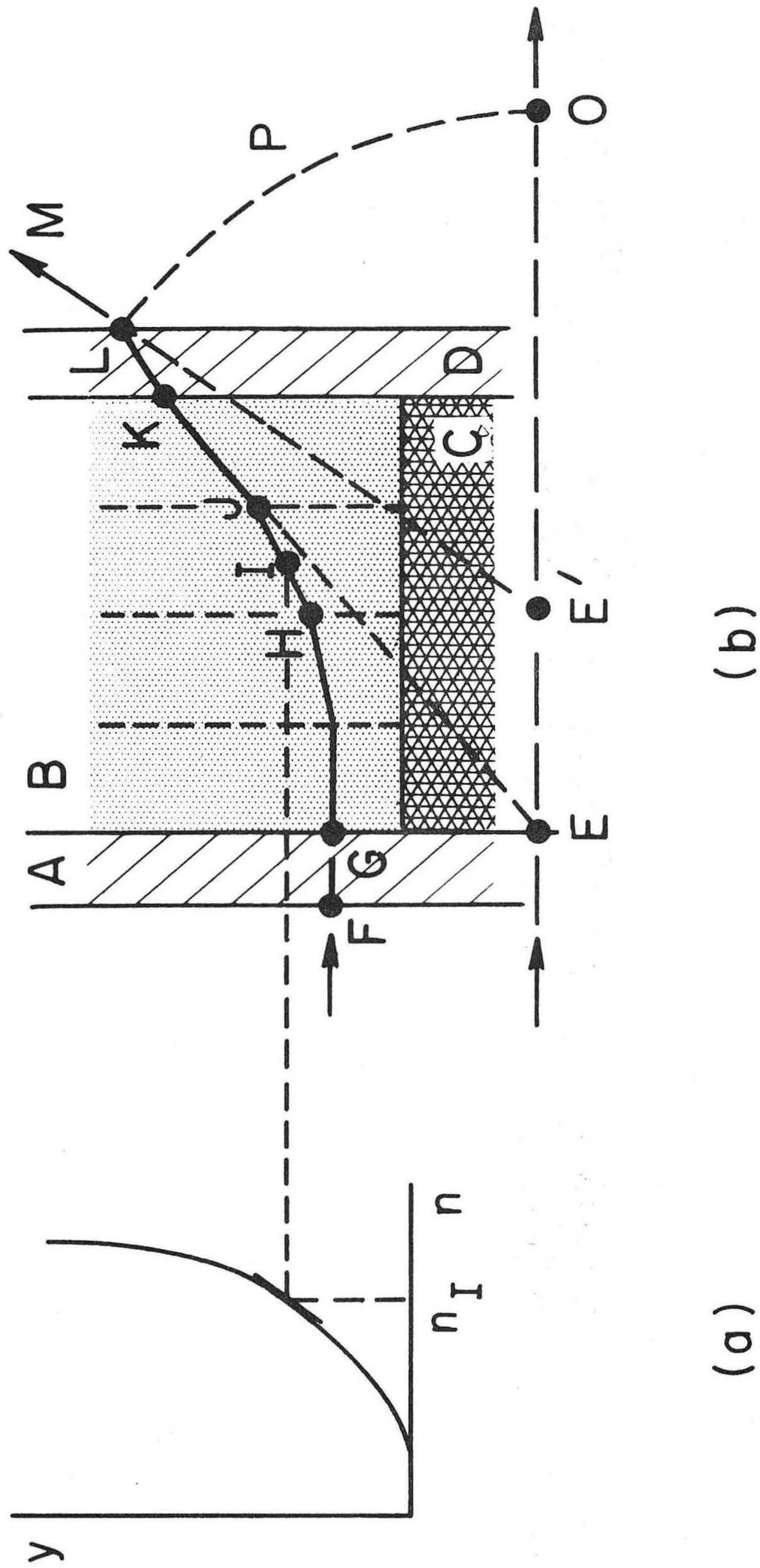


Fig. 63

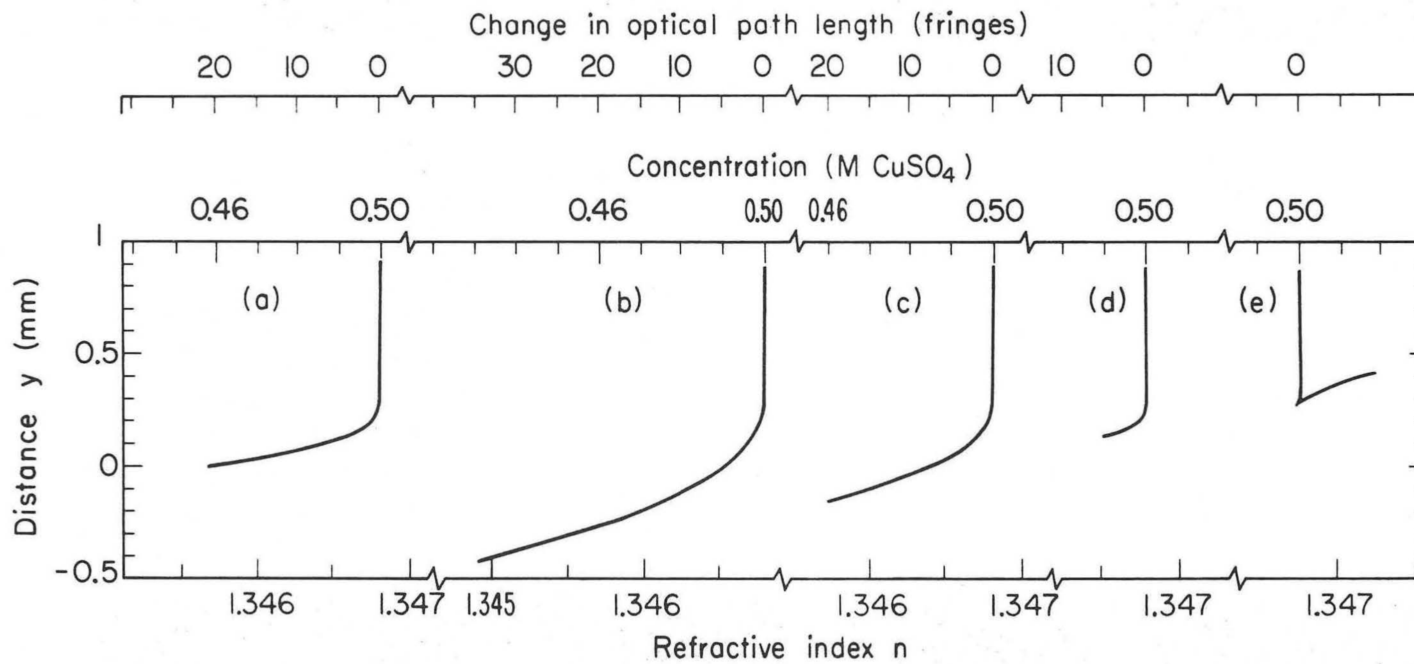


Fig. 64

0 0 0 0 3 6 0 0 0 5 8



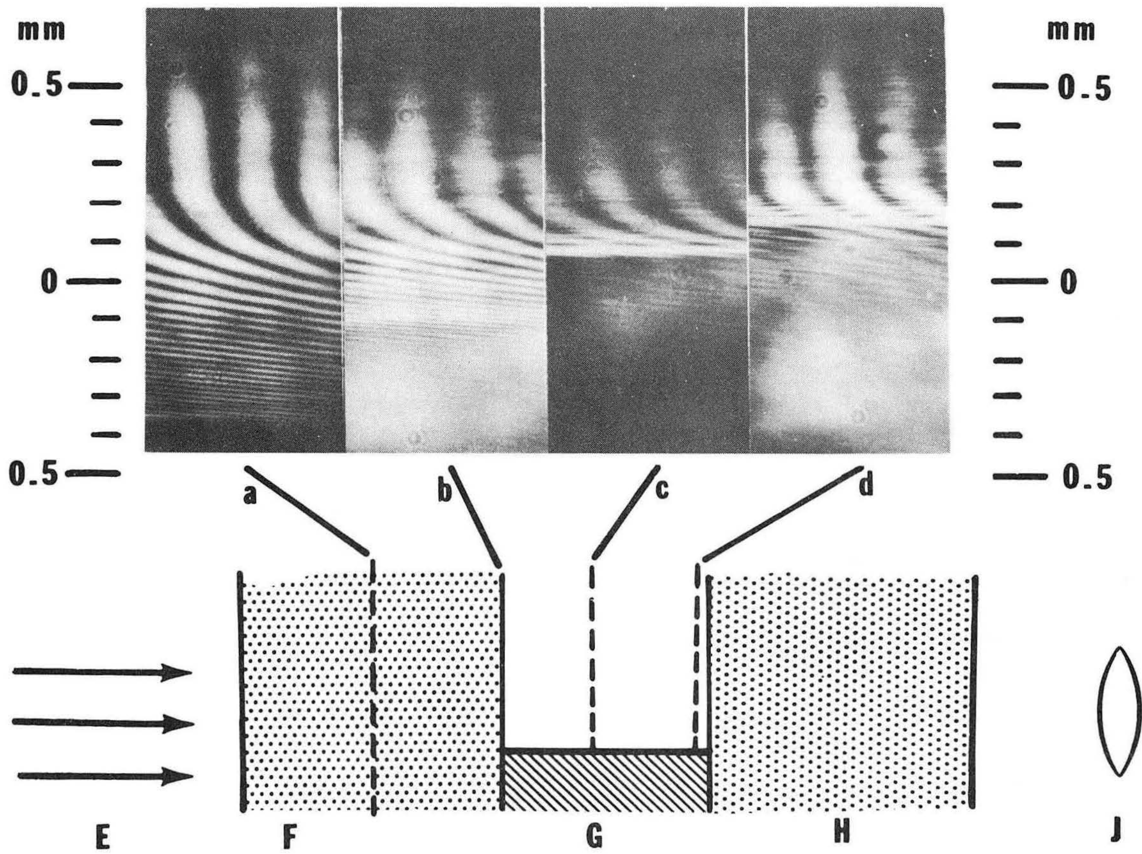


Fig. 65

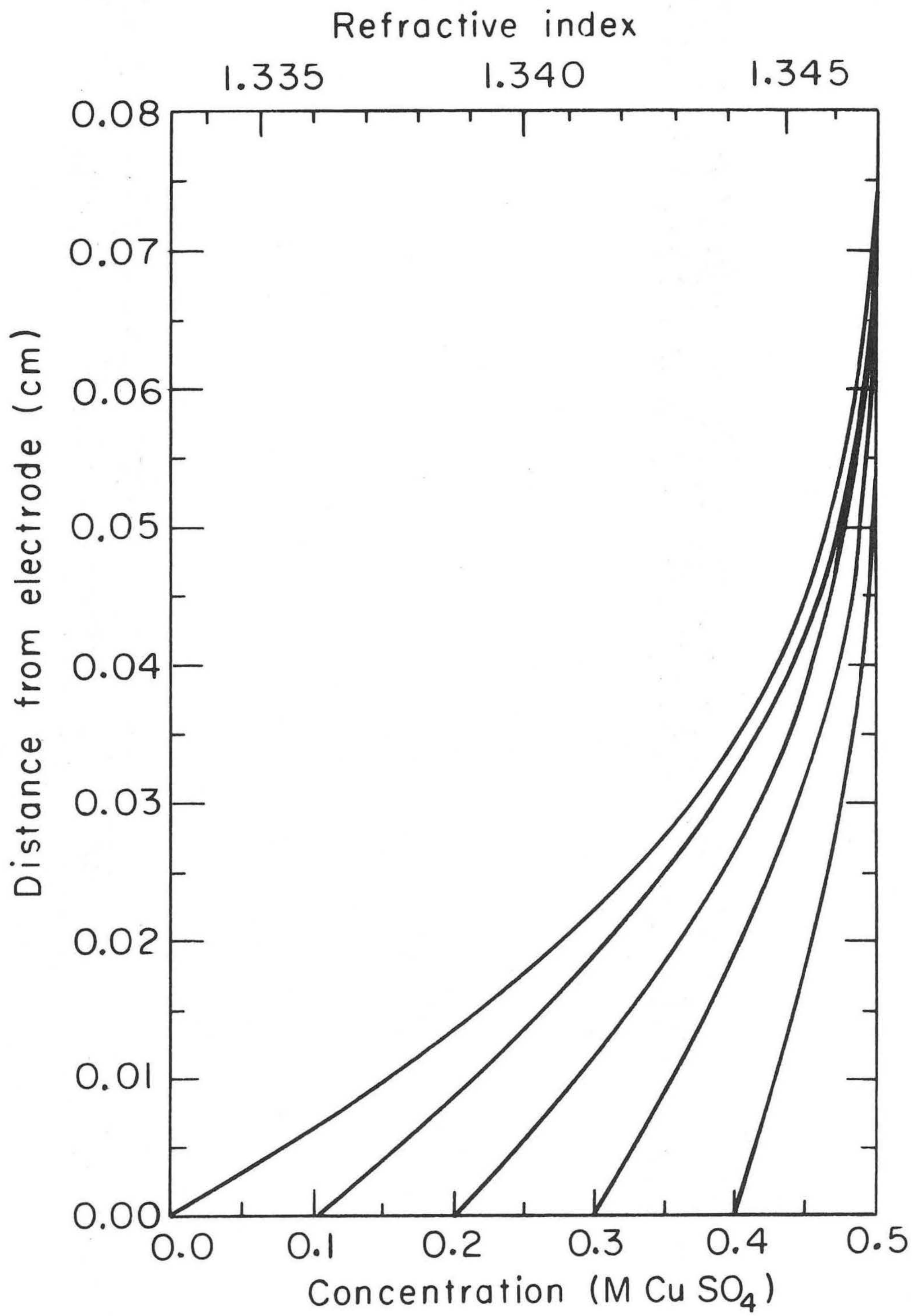


XBL 719-4293

Fig. 66

0 0 0 0 3 6 0 6 0 5 9



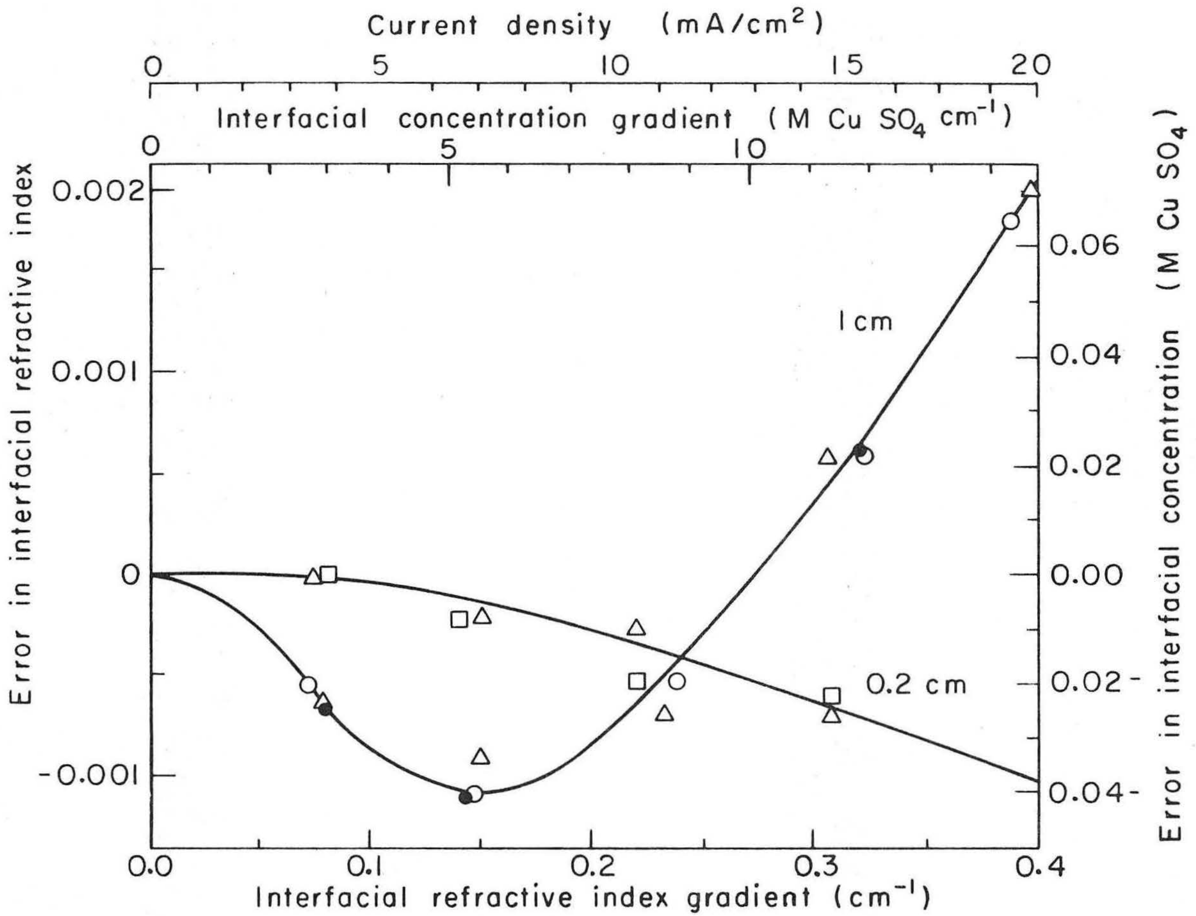


Fig. 67

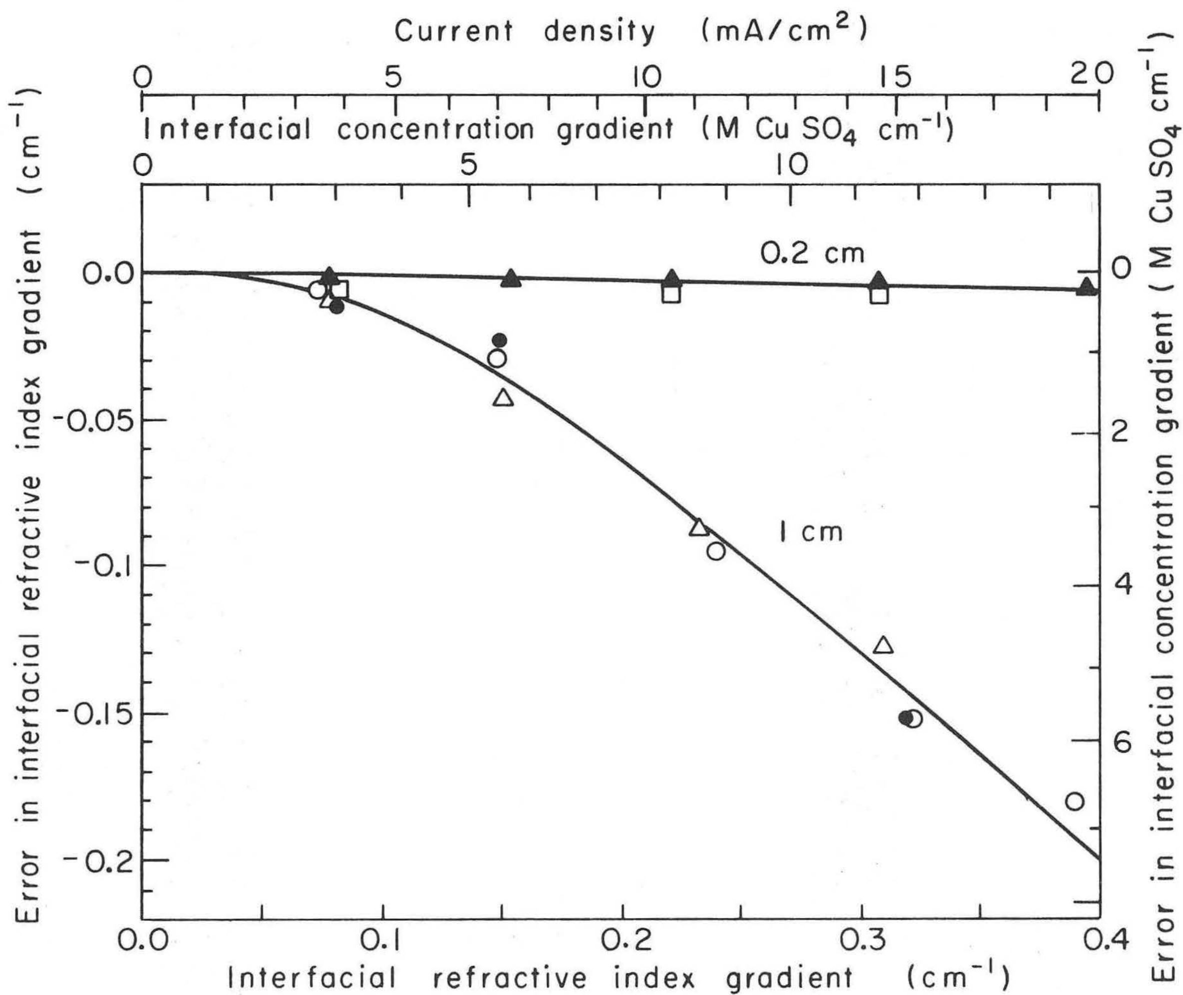


Fig. 68

0 0 0 0 3 6 0 0 0 6 0



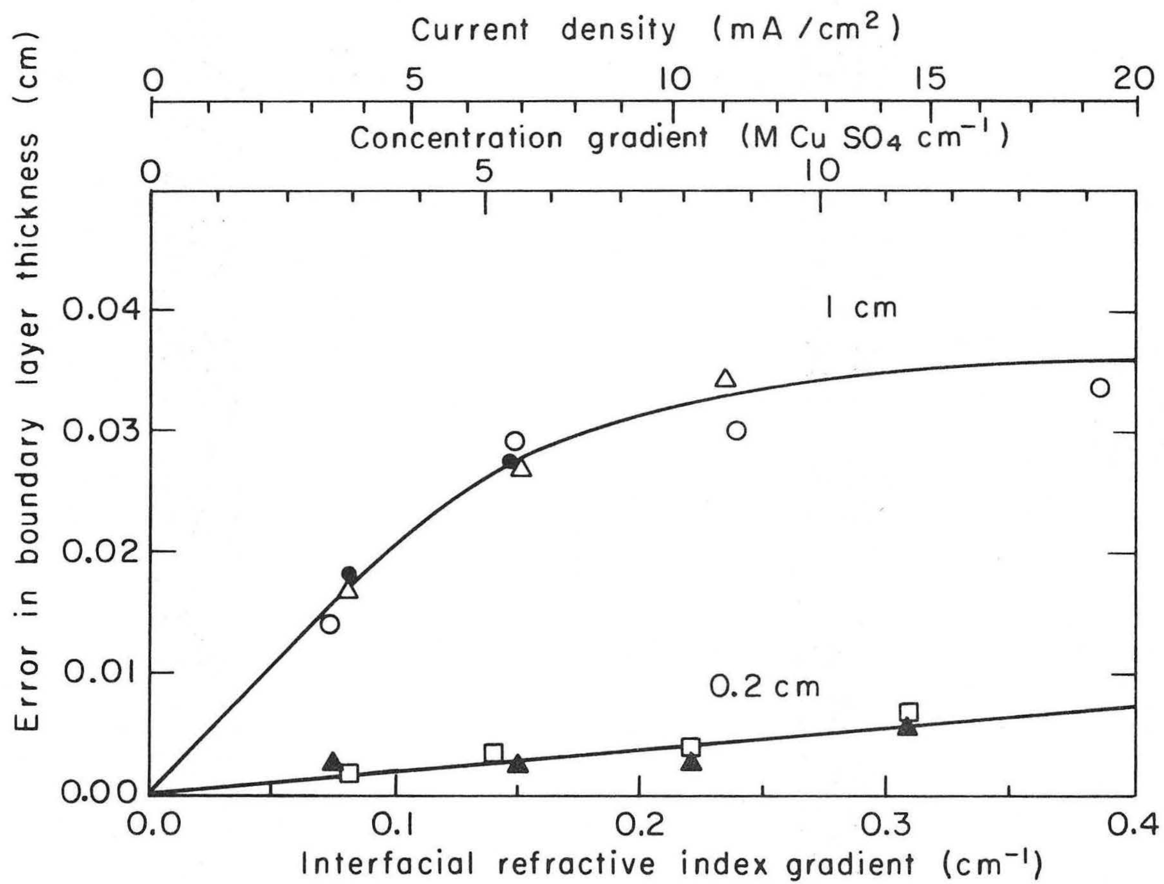


Fig. 69

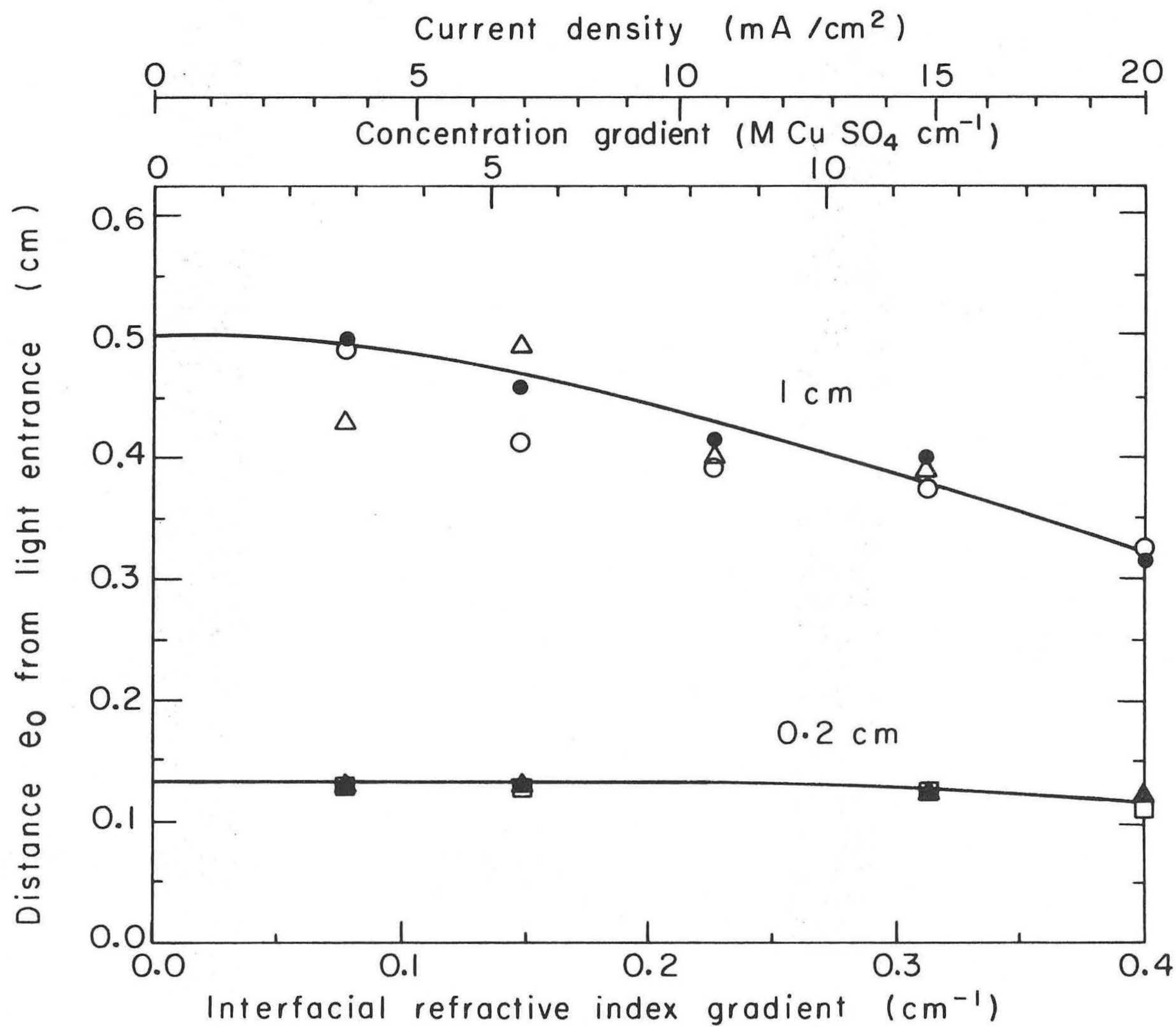


Fig. 70

0 0 0 0 3 6 0 5 0 6 1



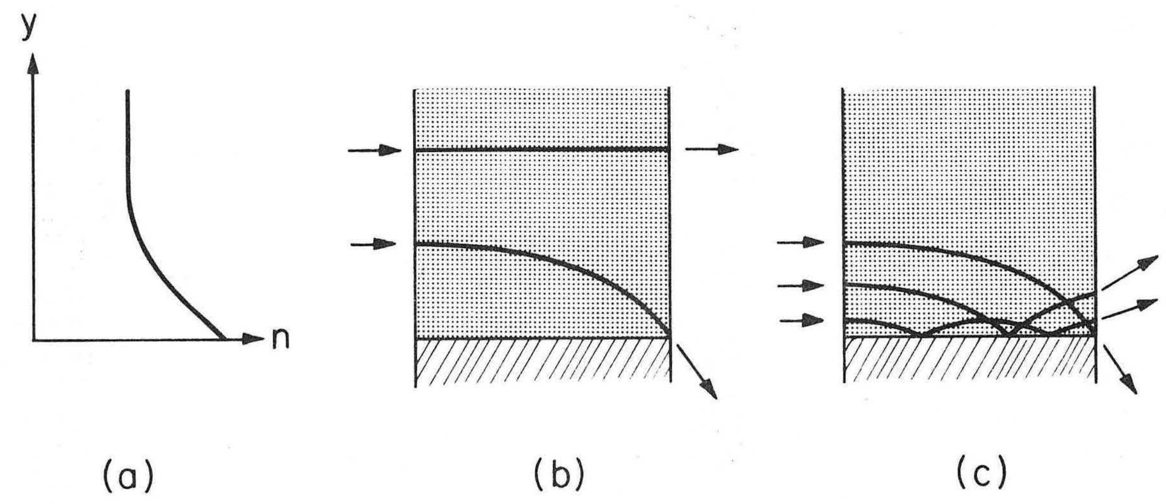


Fig. 71

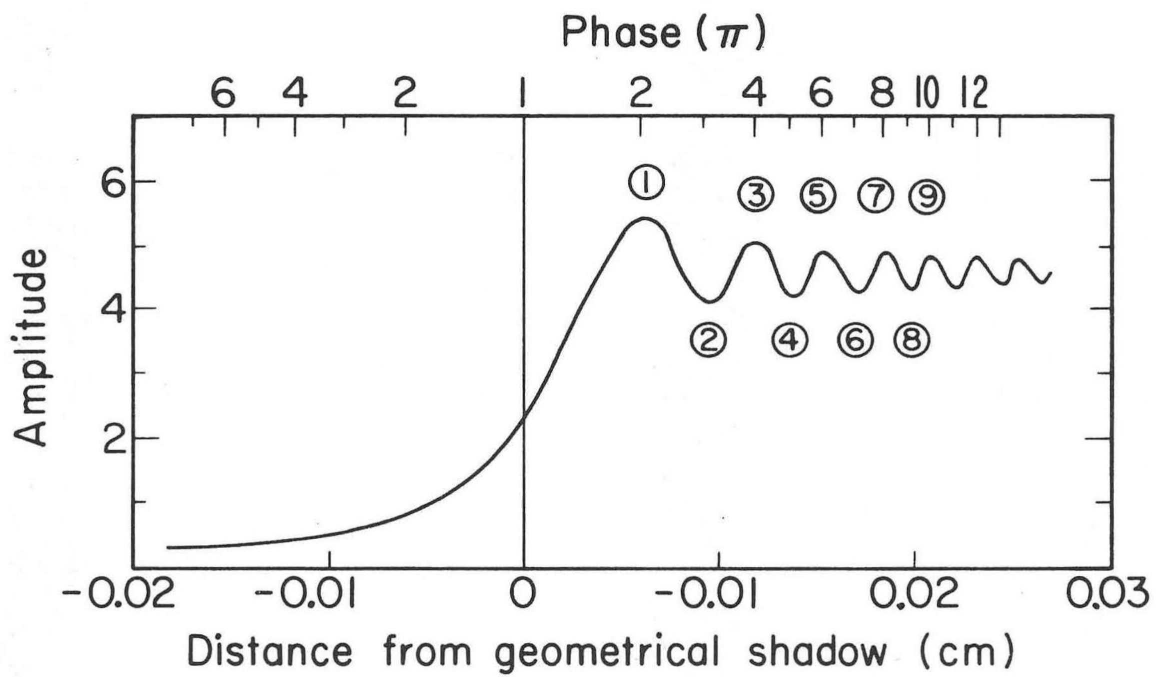


Fig. 72

0 0 0 0 3 6 0 0 0 6 2



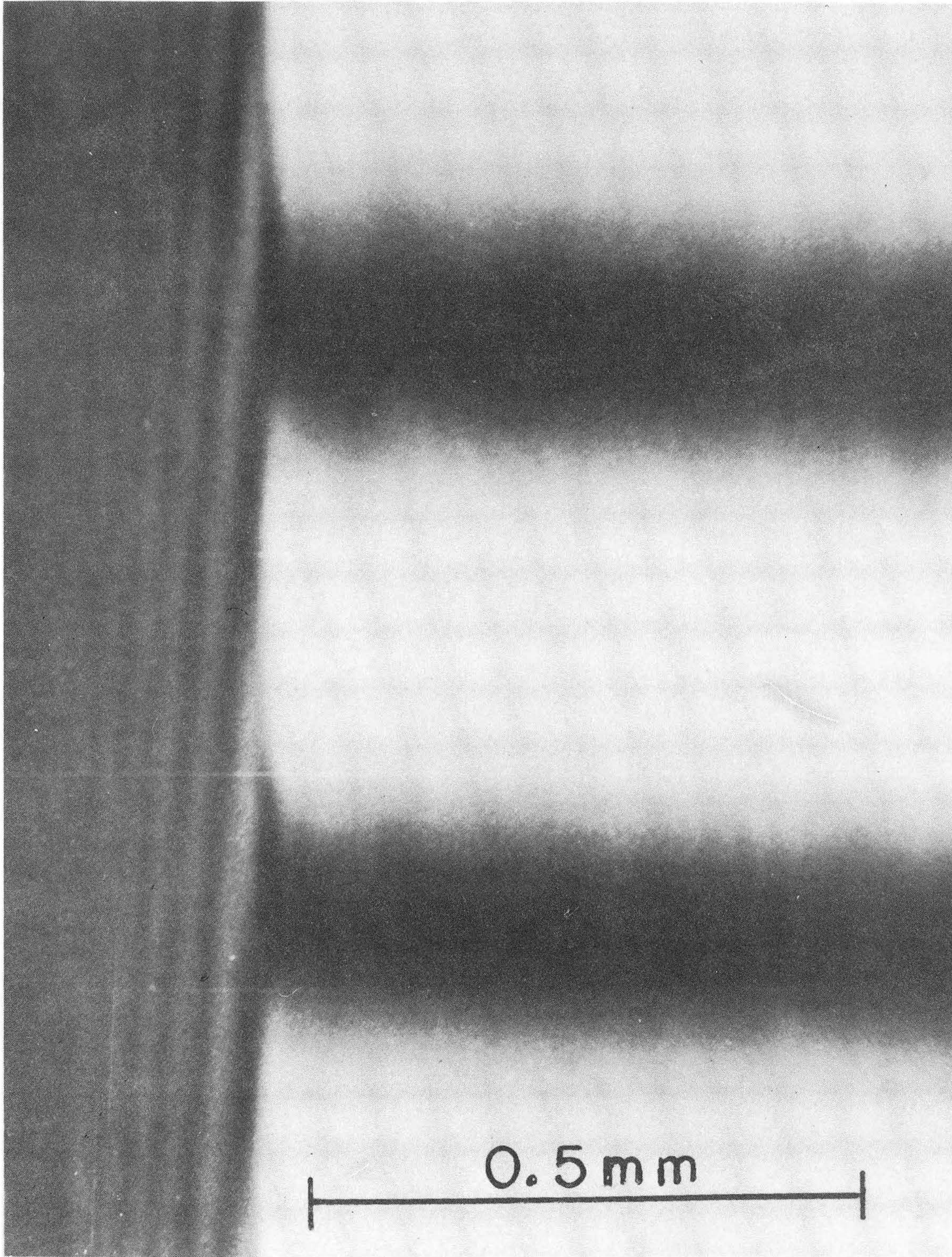


XBB 718-3569

Fig. 73

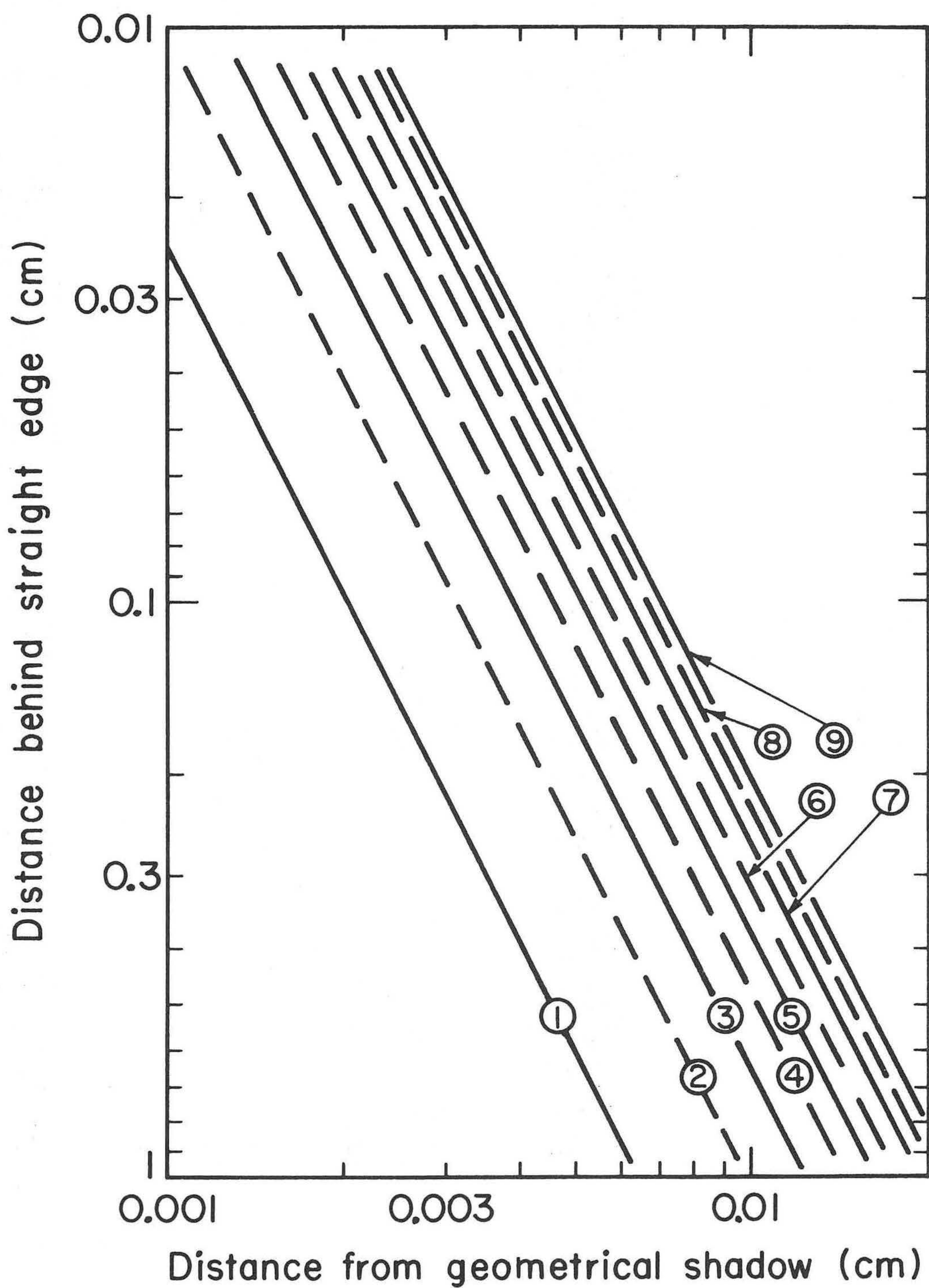


Fig. 74

0 0 0 0 3 6 0 0 0 6 3



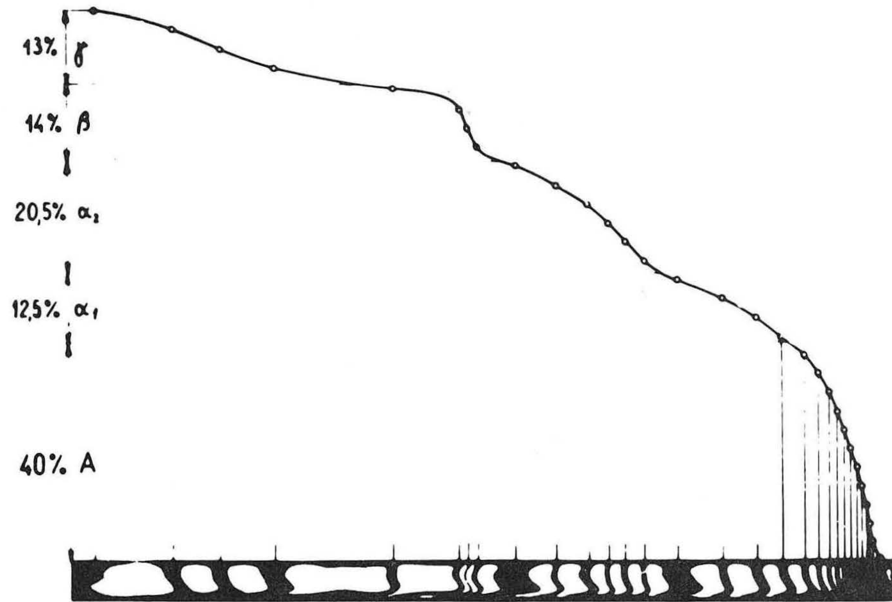


Auswertung einer Aufnahme von normalem menschlichem Serum.
Absteigender Ast, Laufzeit 37 ' bei 8,3 V cm. Michaelispuffer.

MU-35623

Fig. 75

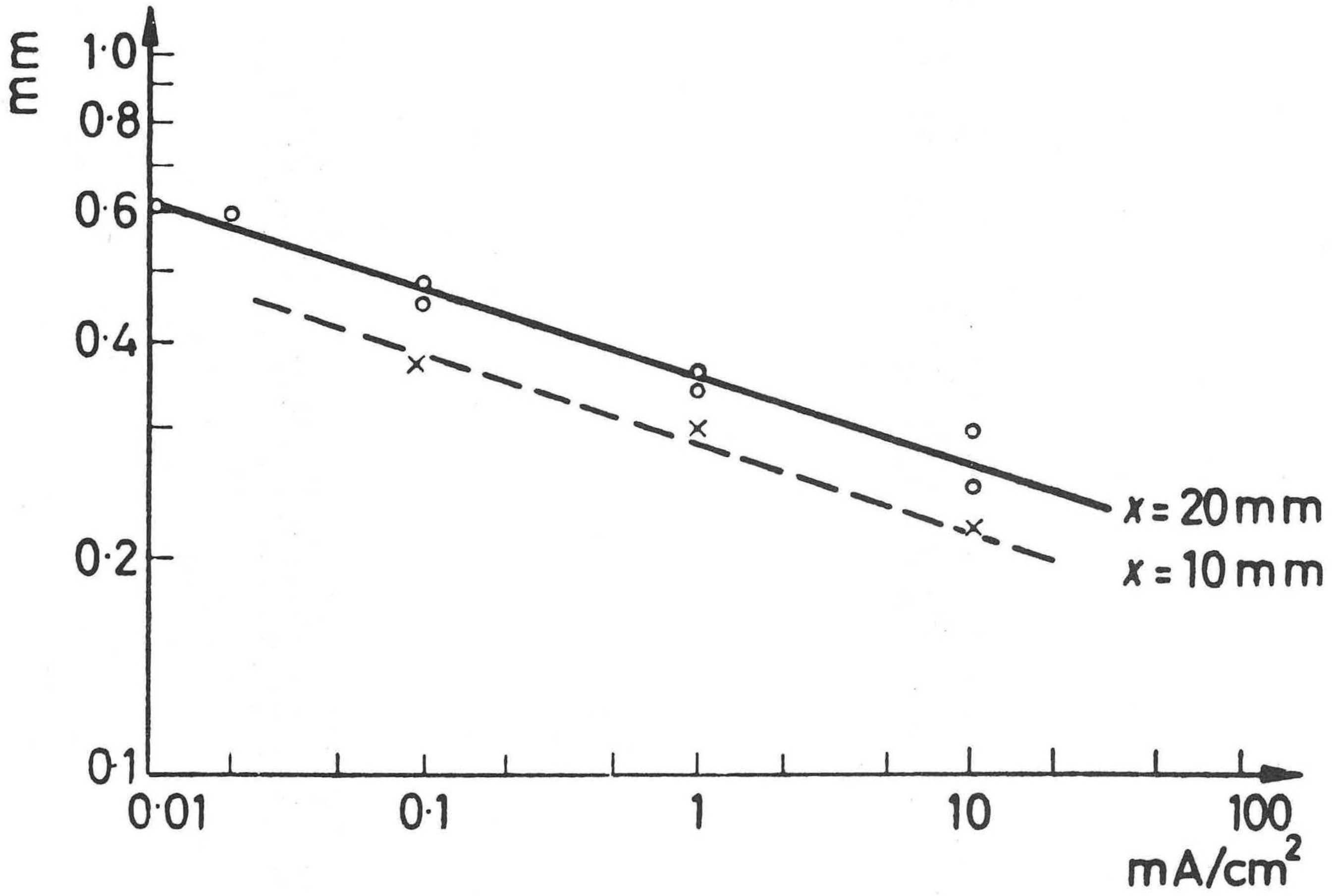


MU-35602

Fig. 76

0 0 0 0 3 6 0 5 0 6 4



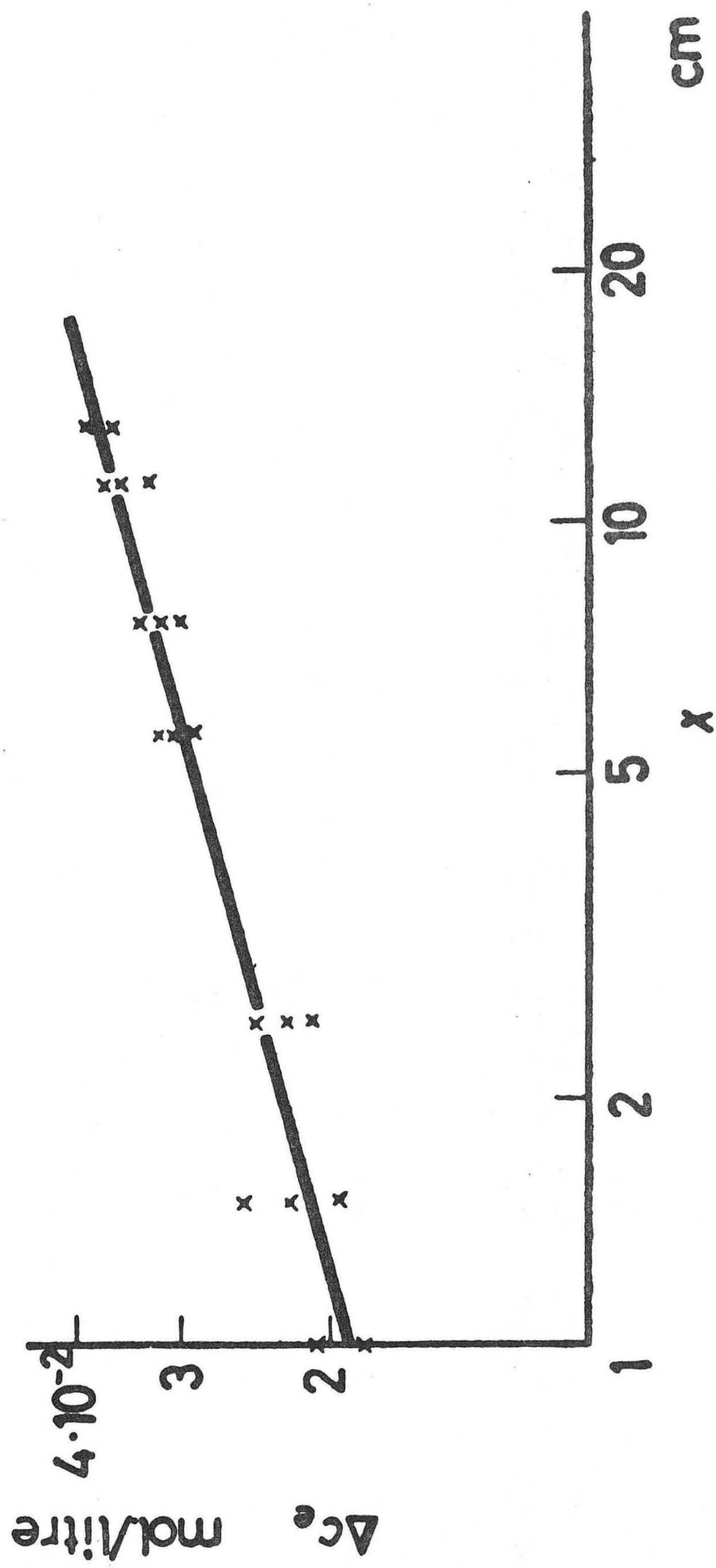


XBL 718-1271

Fig. 77

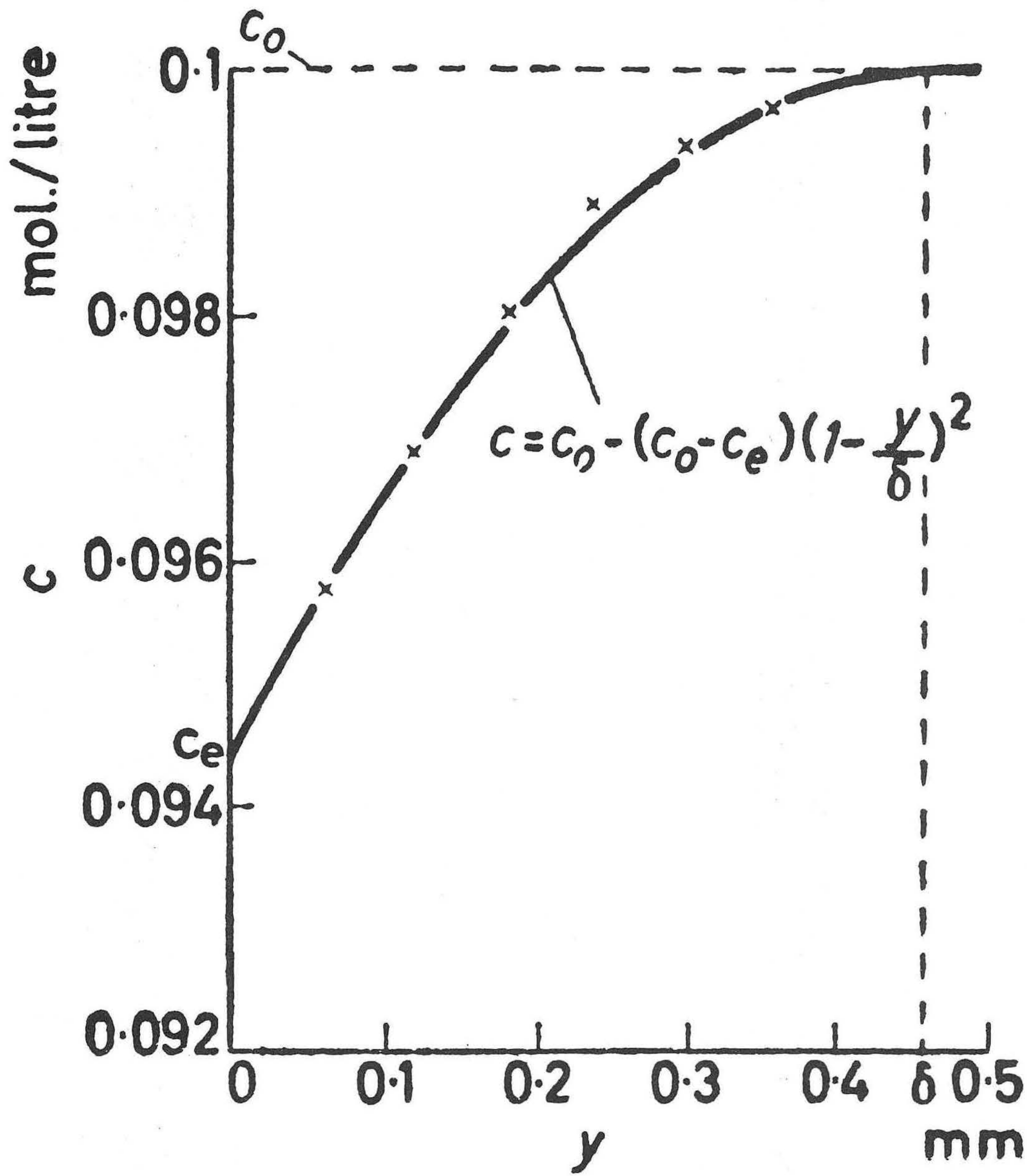


MU-35601

Fig. 78

0 0 0 0 3 6 0 0 0 6 5



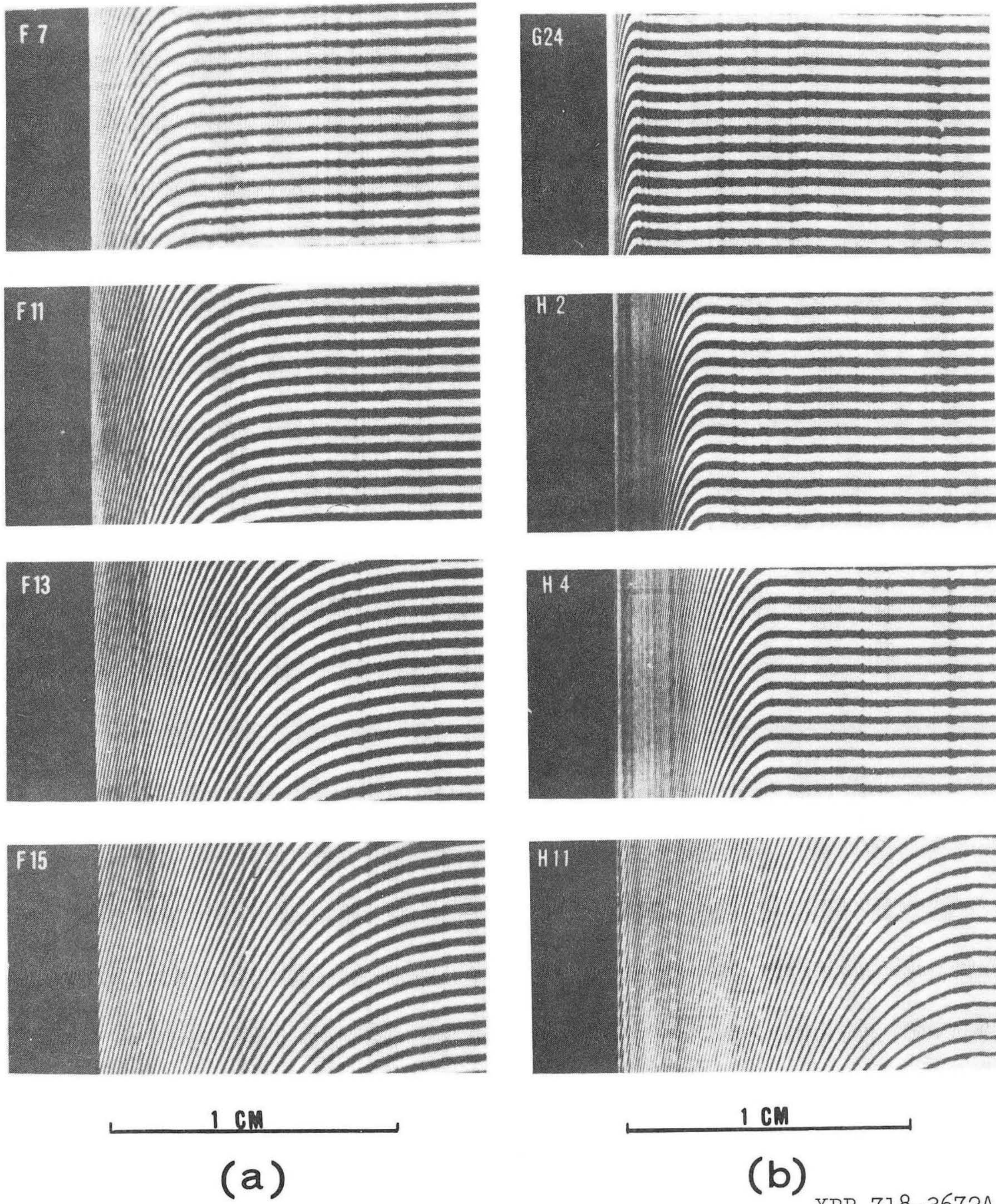


Fig. 79

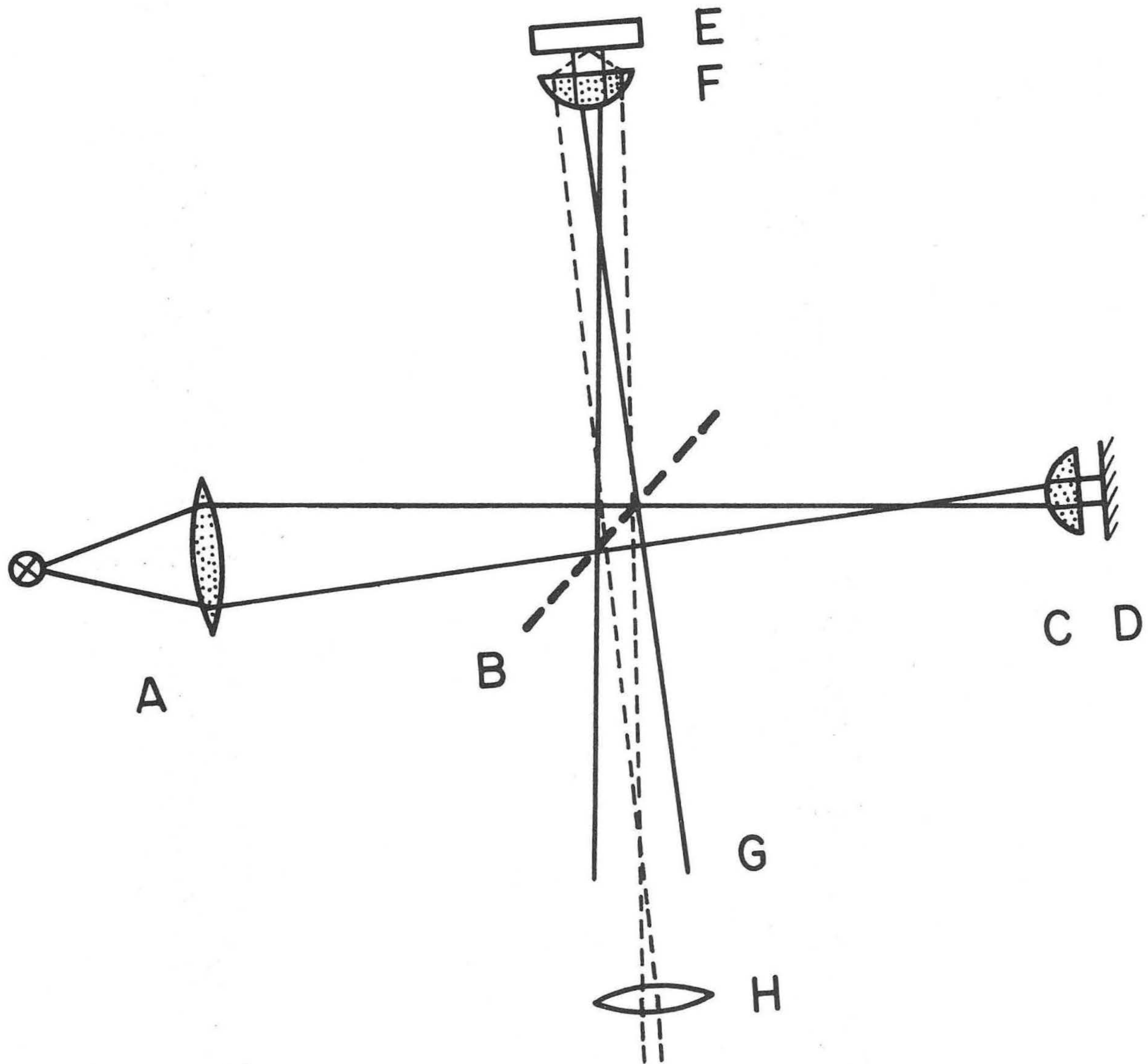


Fig. 80

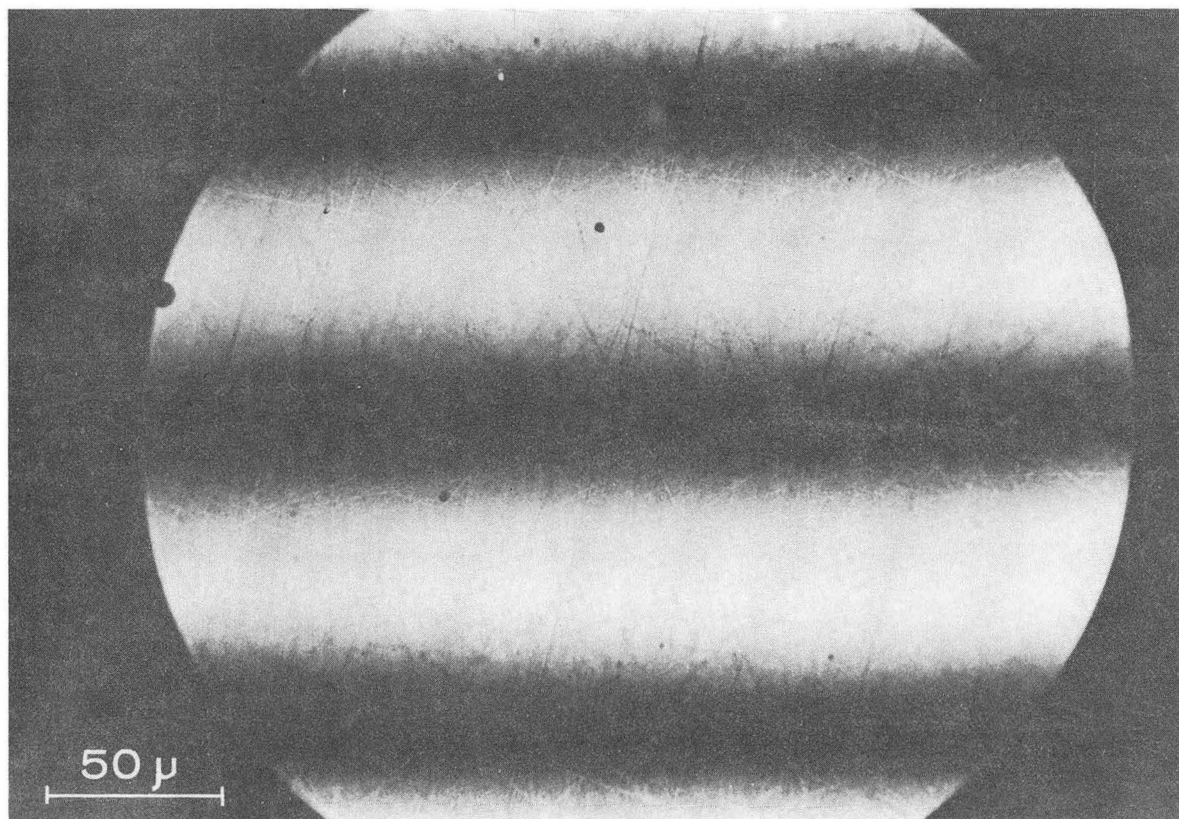


XBB 718-3848

Fig. 81

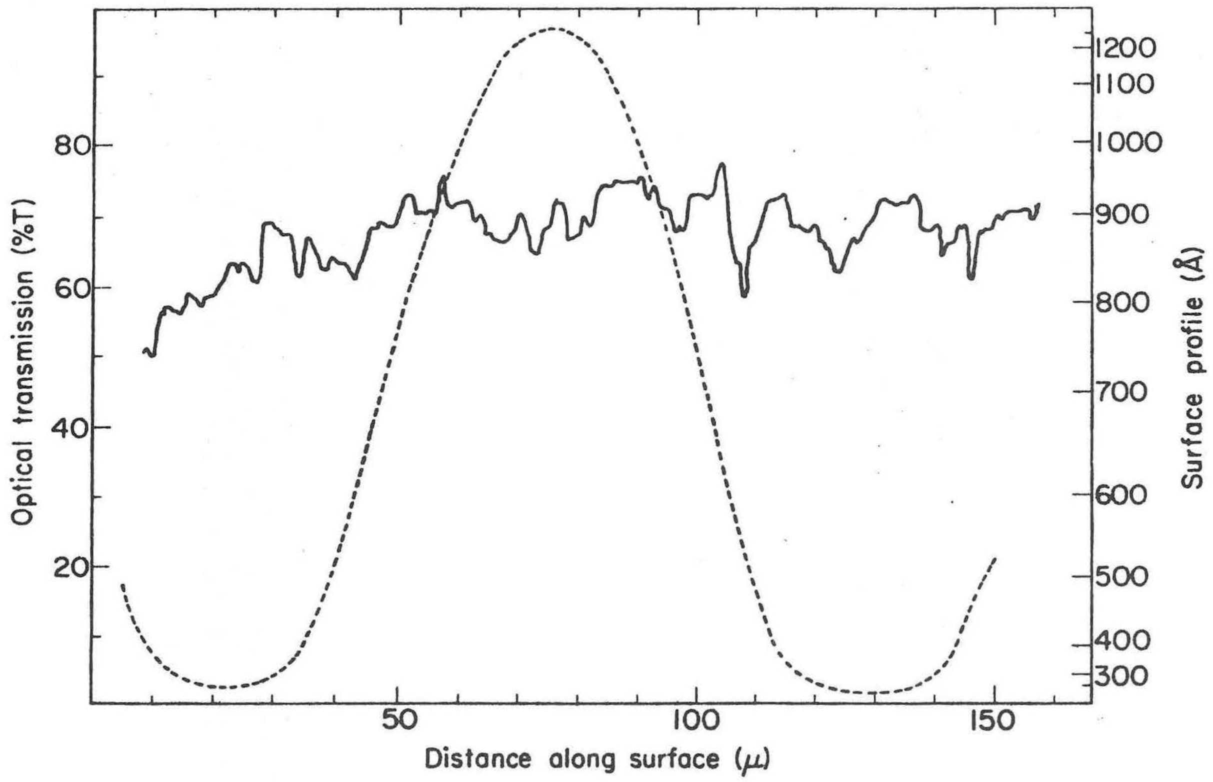


Fig. 82

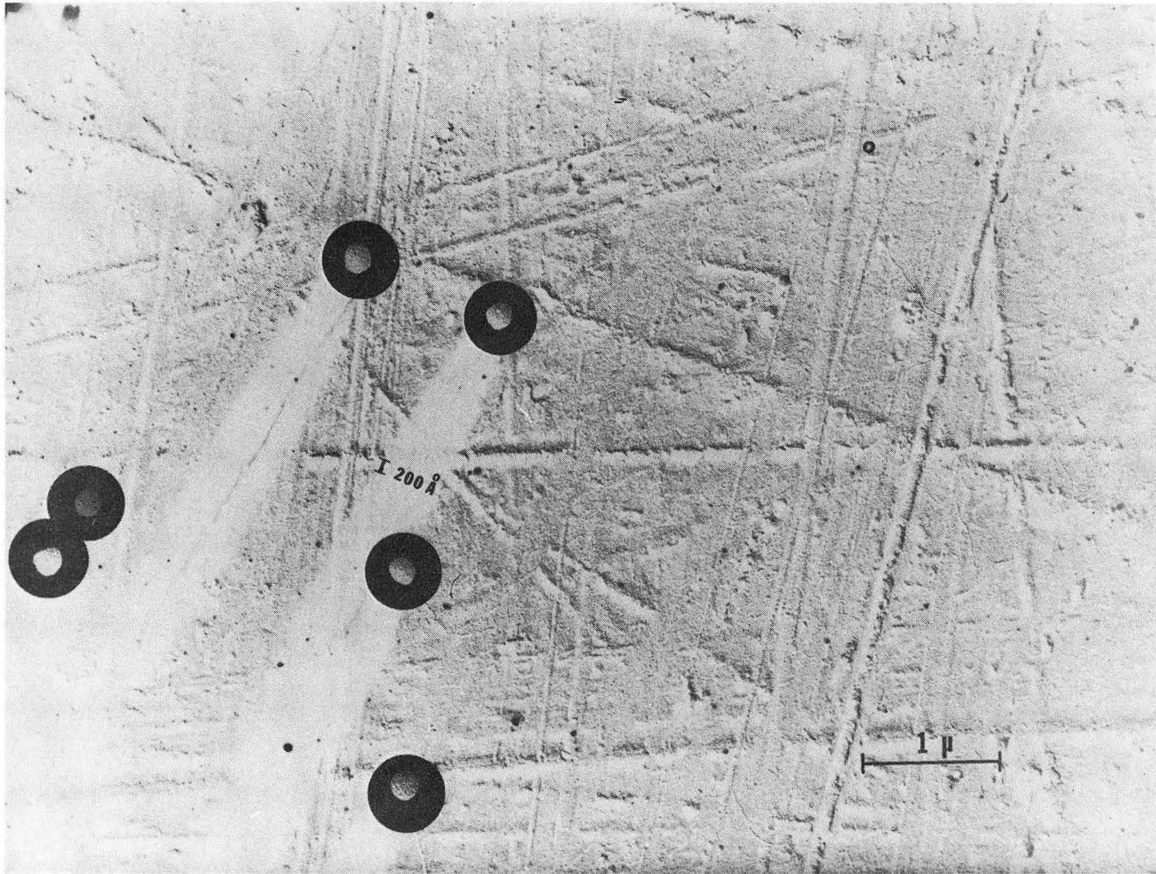


XBB 718-3673

Fig. 83

LEGAL NOTICE

*This report was prepared as an account of work sponsored by the United States Government. Neither the United States nor the United States Atomic Energy Commission, nor any of their employees, nor any of their contractors, subcontractors, or their employees, makes any warranty, express or implied, or assumes any legal liability or responsibility for the accuracy, completeness or usefulness of any information, apparatus, product or process disclosed, or represents that its use would not infringe privately owned rights.*

*TECHNICAL INFORMATION DIVISION*
*LAWRENCE BERKELEY LABORATORY*
*UNIVERSITY OF CALIFORNIA*
*BERKELEY, CALIFORNIA 94720*